University of Groningen
*Faculty of Mathematics and Natural Sciences*

Master Thesis in Applied Mathematics

# A Family of Orthogonalised Nonlinear LES Models Based on the Velocity Gradient: Discretisation and Analysis

*Author:*
R.A. Remmerswaal

*Supervisors:*
prof. dr. ir. R.W.C.P. Verstappen
M.H. Silvis, Msc.
*Second assessor:*
prof. dr. M.K. Camlibel

**Abstract**

Large Eddy Simulation (LES) aims at computing local spatial averages of solutions to the Navier-Stokes equations. The nonlinearity of the Navier-Stokes equations results in the the need for a LES model to obtain a closed set of equations for the spatially averaged velocity field. Existing LES models, e.g., the Smagorinsky and Gradient model, are often derived from the velocity gradient. In this report we generalise this by considering a general form of a nonlinear LES model which is derived from the velocity gradient. This general form of a LES model encompasses dissipative as well as transport terms. We are interested in the former as well as the latter, and therefore propose the explicit separation of dissipative and transport terms by means of orthogonalisation.

Provided with this framework of LES models we develop a Finite Volume discretisation in which we preserve the favorable properties of the analytical equations, like the vanishing sub-grid dissipation due to the LES model in case of a non-dissipative model. Since we base our discretisation on a symmetry preserving discretisation, this results in preserving the energy equality at the discrete level.

The a posteriori analysis of this general framework is done by considering one non-dissipative term in particular. Using the simulation of decaying Homogeneous and Isotropic Turbulence (HIT) as a test case, we perform numerous simulations to characterise this term in terms of both its energy transport, as well as several statistical correlation and structure functions. Our simulations show that using this non-dissipative term in combination with an eddy viscosity model allows for less eddy viscosity being used while obtaining a similar decay of kinetic energy. The correlation functions also show good agreement with experimental data. The proposed general framework of LES models therefore yields promising results, showing that we can indeed model non-dissipative effects in a LES while maintaining good agreement to experimental data. The obtained results provide opportunities for future research.

# Contents

# Acronyms

**CBC** Comte-Bellot and Corrsin. 72

**DNS** Direct Numerical Simulation. 11

**FV** Finite Volume. 35

**HIT** Homogeneous Isotropic Turbulence. 12

**LES** Large Eddy Simulation. 10

**MNSE** Model Navier-Stokes Equations. 11

**NSE** Navier-Stokes Equations. 9

**RANS** Reynolds-Averaged Navier-Stokes. 11

# Chapter 1

# Introduction

In this report we study several different aspects of the simulation of turbulent flow. The first section of this chapter therefore gives an introduction to turbulence in general. The next section covers a brief discussion on the numerical simulation techniques involved. Section three gives an outline of the contents of this report.

## 1.1 Turbulence

Turbulence is a ubiquitous physical phenomenon occurring in fluid flows. The term "turbolenza"' was first mentioned in notes by Leonardo da Vinci. He described turbulence in terms of the interaction between small- and large-scale eddies. Like turbulence, eddies elude precise (mathematical) definition. They are often characterised as distinct vortices which may or may not move along with the flow.

It is universally "agreed upon" that the Navier-Stokes Equations (NSE) describe the flow of any type of fluid, e.g. liquids or gases. Therefore the NSE are also a model for turbulent flow. The NSE were first derived by Navier (1823) but more rigorously understood by Stokes (1845). The equations follow from the conservation of mass and momentum, together with Newton's law of viscosity. Details about the derivation can be found in many books about the subject, see for instance Berselli et al. (2005). The NSE for incompressible fluids are given by

$$\begin{aligned} \nabla \cdot \mathbf{u} &= 0 \quad \text{in } \Omega \times (0,T), \\ \partial_t \mathbf{u} + \nabla \cdot (\mathbf{u} \otimes \mathbf{u}) + \frac{1}{\rho} \nabla p - \nu \Delta \mathbf{u} &= \mathbf{f} \quad \text{in } \Omega \times (0,T). \end{aligned} \tag{1.1}$$

The velocity field is given by $\mathbf{u} = (u_1, \ldots, u_d)^T \in \mathbb{R}^d$, $p$ denotes the pressure and the kinematic viscosity is given by $\nu$. The external forcing is given by $\mathbf{f}$. The flow domain $\Omega \subset \mathbb{R}^d$ is assumed to have a sufficiently smooth boundary $\partial\Omega$, the dimension $d$ is either two or three. We generally impose periodic boundary conditions on the velocity field, as well as on the pressure. This simplifies the discussion, but it is not necessarily an oversimplification since the simulations we consider in this report satisfy this type of boundary condition as well.

In dimensionless form the NSE are given by

$$\begin{aligned} \nabla \cdot \mathbf{u} &= 0 \quad \text{in } \Omega \times (0,T), \\ \partial_t \mathbf{u} + \nabla \cdot (\mathbf{u} \otimes \mathbf{u}) + \nabla p - \frac{1}{\mathrm{Re}} \Delta \mathbf{u} &= \mathbf{f} \quad \text{in } \Omega \times (0,T). \end{aligned} \tag{1.2}$$

The parameter Re is the Reynolds number, it is the ratio of convective over diffusive forces, and is defined

by

$$\mathrm{Re} := \frac{\mathcal{U}\mathcal{L}}{\nu},$$

where $\mathcal{U}$ and $\mathcal{L}$ are characteristic velocity and length scales respectively.

The nonlinear term of the NS equation is the convection term, it describes the transport of momentum by the velocity field. The term involving the Reynolds number represents the diffusion of momentum. When the Reynolds number is small ($\mathrm{Re} < 2000$) experiments show that fluid flow is laminar, i.e. the streamlines are parallel. This corresponds to diffusion dominating over convection. For larger values of the Reynolds number the flow transitions into becoming turbulent, here the nonlinearity of the NSE becomes dominant.

There is no universally agreed upon definition of turbulence, however there are some characteristic properties (McDonough, 2004):

- *Seemingly* random behaviour which could be described as chaotic.
- Sensitivity to initial conditions, as is typical for a chaotic dynamical system.
- Consists of a large range of (relevant) length and time scales (and hence also velocity scales).
- Enhanced diffusion and dissipation, mixing due to turbulence.
- Three dimensionality, time dependence and rotationality. Some mathematicians hypothesise relationships between turbulence and vorticity.
- Intermittency in space and time. (Intermittency is the percentage of time for which a certain position in the domain contains turbulent flow as opposed to laminar flow.)

Many of these characteristic properties are summarized in the following deterministic definition of turbulence (McDonough, 2004)

> *" Turbulence is any chaotic solution to the 3D NS equations that is sensitive to initial data and which occurs as a result of successive instabilities of laminar flows as a bifurcation parameter is increased through a succession of values. "*

This definition emphasises chaotic behavior instead of random behavior as was used before to describe turbulence using a statistical approach.

## 1.2 Numerical simulation

There are many numerical techniques that can be employed to solve the NSE. For example: Finite Volume, Finite Difference, Finite Element, Spectral or Spectral Element methods. But also particle methods.

Besides the choice of numerical technique, there is also the consideration of which equations are to be solved. Of course the goal will always be finding approximate solutions to the NSE. However if the resolution is limited, additional terms may have to be added to the NSE. Like in Large Eddy Simulation (LES) where a local spatial average of the solution is computed.

*DNS*

Direct Numerical Simulation (DNS) means numerically approximating the solution to the NSE (1.2) where the resolution is sufficiently high (mesh width sufficiently small) for all scales of motion to be resolved. That is, even the smallest scales of motions can be represented on the mesh. When considering homogeneous isotropic turbulence, the ratio between largest and the smallest scales of motion is proportional to $\mathrm{Re}^{3/4}$, as follows from Kolmogorov's theory. Hence when considering three-dimensional flow in a modest engineering application DNS quickly becomes infeasible. DNS still serves a purpose as a method to verify alternative simulation techniques like Reynolds-Averaged Navier-Stokes (RANS) or LES.

The rate of dissipation in a simulation of the NSE is highest at the smallest scales of motion. More precisely, the rate of dissipation is proportional to the wavenumber squared. If the mesh width is too coarse for all scales of motion to be resolved, the simulation will show a pile up of energy at the smallest scales of motion. This is due to that fact that the transport of energy from the larger scales to the small scales exceeds the amount of energy the dissipative term can dissipate.

*LES*

In LES the desire is to not resolve all scales of motion, but instead the aim is to calculate local spatial averages of solutions to the NSE. This is realised by trying to find an equation for the local spatially averaged velocity field denoted by $\bar{\mathbf{u}}$. Often a spatial average is obtained by convolving the velocity field $\mathbf{u}$ by a homogeneous filter kernel $g_\delta$, that is

$$\bar{\mathbf{u}}(\mathbf{x},t) = (g_\delta * \mathbf{u}) = \int_{\mathbb{R}^d} g_\delta(\mathbf{x}-\mathbf{r})\mathbf{u}(\mathbf{r},t)\,d\mathbf{r}.$$

Simply applying this filtering (spatial averaging) operation to the Navier-Stokes equations does not yield a closed set of equations in terms of the variable $\bar{\mathbf{u}}$

$$\begin{aligned} \nabla\cdot\bar{\mathbf{u}} &= 0, \\ \partial_t\bar{\mathbf{u}} + \nabla\cdot(\bar{\mathbf{u}}\otimes\bar{\mathbf{u}}) + \nabla\bar{p} - \frac{1}{\mathrm{Re}}\Delta\bar{\mathbf{u}} + \nabla\cdot(\overline{\mathbf{u}\otimes\mathbf{u}} - \bar{\mathbf{u}}\otimes\bar{\mathbf{u}}) &= \bar{\mathbf{f}}. \end{aligned} \tag{1.3}$$

In deriving (1.3) we assume periodic boundary conditions are imposed, such that the filtering operation commutes with differentiation. It follows that, when solving these equations, we require a closure model (LES model, sub-grid scale model) to replace the exact sub-filter scale stress tensor

$$\boldsymbol{\tau}^{\mathrm{Exact}}(\mathbf{u}) := \overline{\mathbf{u}\otimes\mathbf{u}} - \bar{\mathbf{u}}\otimes\bar{\mathbf{u}},$$

with a term that depends only on $\bar{\mathbf{u}}$. We denote by

$$\mathbf{w} \approx \bar{\mathbf{u}}, \quad q \approx \bar{p},$$

the approximate solution after replacing the exact sub-filter scale stress tensor with an approximate tensor depending only on the filtered velocity field $\bar{\mathbf{u}}$. This solution then satisfies the Model Navier-Stokes Equations (MNSE) *, given by

$$\begin{aligned} \nabla\cdot\mathbf{w} &= 0, \\ \partial_t\mathbf{w} + \nabla\cdot(\mathbf{w}\otimes\mathbf{w}) + \nabla q - \frac{1}{\mathrm{Re}}\Delta\mathbf{w} + \nabla\cdot\boldsymbol{\tau} &= \bar{\mathbf{f}}. \end{aligned}$$

*We call the equations the *Model* NSE to emphasise that the equations are equipped with a LES *model*. Of course the NSE are also a model.

We emphasise that the closure model $\boldsymbol{\tau}(\bar{\mathbf{u}})$ is *not* intended to equal $\boldsymbol{\tau}^{\text{Exact}}(\mathbf{u})$ since the former depends on the filtered velocity field which is constructed *such that* it contains less information than the full velocity field $\mathbf{u}$ does. The closure model should merely model the influence of the sub-grid scales on the resolved scales and vice versa. Traditionally, this is done with an emphasis on the ability to capture a sufficient amount of dissipation.

Several closure models are introduced and discussed in Section 3.2.

## 1.3 Outline

The contents of this thesis are distributed over the five remaining chapters. Chapter 2 gives an introduction to the theory regarding turbulence; in particular we discuss the idealised case of (decaying) Homogeneous Isotropic Turbulence (HIT), as well as some theory regarding the existence and uniqueness of the NSE (additionally, Appendix A.1 gives a brief introduction to Sobolev spaces and its notation). Even though the research done in later chapters is not as involved as this formal discussion, we still include some of this theory, since it is an important aspect of the NSE in general, and should not be overlooked. The theory regarding HIT involves some statistical analysis and is strongly related to the famous work of Kolmogorov.

In Chapter 3 we describe some existing LES models which are all functions of the velocity gradient. Two of these models are eddy viscosity models, and hence only model the dissipative processes contained in the exact sub-grid scale stress tensor. We therefore propose a generalisation of such models by considering a family of tensor models where each term is derived from the velocity gradient. Moreover we orthogonalise these terms, thereby generalising the separation between dissipation and transport mechanisms.

Having such a general framework, in Chapter 4 we consider suitable discretisation methods for this family of tensor models. With an emphasis on preserving conservation laws, we derive two methods for the discretisation of the tensor model. The first is an adaptation of a discretisation method which, without orthogonalisation, would yield the smallest truncation error of the two methods. The second method is a rather straightforward method, which is computationally cheaper and moreover satisfies the previously mentioned preservation property by default. After comparing the two methods, we motivate our final choice for method two as our discretisation method.

The final part of the research, contained in Chapter 5, discusses some preliminary results in using this general framework as an LES model. Before doing so, we need to have some idea of what kind of transport mechanism each of the non-dissipative terms represents. Therefore we consider the analysis of one term in particular. We quantify the transport of energy by comparing this term to a known transport mechanism represented by the convective term. The results of this comparison yields the hypothesis that using this term may indirectly increase dissipation by transporting energy from large to small scales of motion. To test this hypothesis we consider a two-parameter model consisting of a dissipative term together with the aforementioned transport term. Using reference data from a physical experiment we are then able to assess how well the two-parameter model performs in the simulation of decaying HIT.

In Chapter 6 we summarise the contents of this report and briefly discuss possible areas of future research.

# Chapter 2

# Theory of turbulence and the Navier-Stokes equations

In this chapter we introduce some important theoretical aspects of turbulence as well as the Navier-Stokes Equations. We first introduce some notation in Section 2.1.

The results about turbulence we present here relate to statistical measures, an introduction into which is given in Section 2.3. Section 2.3 concludes with a brief discussion of the results by Kolmogorov which yield the famous $-5/3$-law. This section results in several characterisations of a velocity field resulting from decaying HIT. Such characterisations will be used in Chapter 5 as a method of comparing several LES models.

In Section 2.4 the mathematical properties, and difficulties, regarding the existence and uniqueness of weak solutions to the (M)NSE are discussed.

## 2.1 Notation

Matrices, vectors in $\mathbb{R}^N$, vector valued coordinates, vector valued functions and rank 2 tensors are denoted by boldface letters.

We denote the velocity gradient tensor by $\nabla \mathbf{u}$, whose elements are given by

$$\nabla \mathbf{u}_{mn} = \frac{\partial u_m}{\partial x_n}.$$

Often the symmetric and skew-symmetric parts of the velocity gradient tensor are explicitly denoted by $\mathbf{S}$ and $\mathbf{\Omega}$ respectively.

Unless indicated otherwise, repeated indices imply a summation only if the indices take values from 1 to $d$, where $d$ is the spatial dimension we work in.

The inner product on $\mathbb{R}^N$ is denoted by

$$(\mathbf{x}, \mathbf{y}) = \sum_{i=1}^{N} x_i y_i.$$

And correspondingly, the Euclidean 2-norm is denoted by $|\mathbf{x}|$.

The $L^2(\Omega)$ inner product is denoted by

$$\langle f, g \rangle := \langle f, g \rangle_{L^2(\Omega)} = \int_\Omega fg \, d\mathbf{x}.$$

Similarly, the $L^2(\Omega)$-norm is denoted by

$$\|f\| := \|f\|_{L^2(\Omega)} = \sqrt{\langle f, f\rangle_{L^2(\Omega)}}.$$

A brief introduction to the notation regarding Sobolev spaces is given in Appendix A.1.

In the derivation of the NSE we find that the stress acting on the interface between fluid elements is described by some stress tensor $\boldsymbol{\sigma}$. The convective term in (1.2) is denoted by $\nabla \cdot (\mathbf{u} \otimes \mathbf{u})$, where $\mathbf{u} \otimes \mathbf{u}$ is a tensor whose components are given by

$$(\mathbf{u} \otimes \mathbf{u})_{mn} = u_m u_n.$$

Without going into the details of a precise mathematical description of tensors, we simply consider a (rank two) tensor $\boldsymbol{\tau}$ as a mapping

$$\boldsymbol{\tau} : \Omega \times (0, T) \to \mathbb{R}^{d \times d}.$$

Hence locally, at a fixed point in space and time, a rank two tensor may be treated as a matrix. Hence the usual matrix product is used to construct products of tensors.

We define the *local* tensor inner product as

$$\boldsymbol{\tau} : \boldsymbol{\eta} = \sum_{m,n=1}^{d} \tau_{mn}\eta_{mn},$$

which induces the $L^2(\Omega)$ tensor inner product in the following way

$$\langle \boldsymbol{\tau}, \boldsymbol{\eta} \rangle = \int_\Omega \boldsymbol{\tau} : \boldsymbol{\eta} \, d\mathbf{x}.$$

## 2.2 Energy (in-)equalities

We will mostly consider the MNSE in the strong form given by (1.1). A more formal discussion regarding the regularity and existence of solutions is given in Section 2.4.

The NSE are derived from physical conservation laws, stating that both mass and momentum are conserved. A third and equally important quantity is the total kinetic energy, given by

$$E(t) := \frac{1}{2}\|\mathbf{u}\|.$$

In what follows we discuss the equations that govern the conservation of kinetic energy in both the spatial domain, as well as in the frequency domain where we consider the kinetic energy per wavenumber.

### 2.2.1 Spatial domain

Taking the $L^2$ inner product of the NSE with the velocity field $\mathbf{u}$ yields

$$\frac{1}{2}\frac{d}{dt}\|\mathbf{u}\|^2 + \langle \nabla \cdot (\mathbf{u} \otimes \mathbf{u}), \mathbf{u}\rangle + \langle \nabla p, \mathbf{u}\rangle - \frac{1}{\mathrm{Re}} \langle \Delta \mathbf{u}, \mathbf{u}\rangle = \langle \mathbf{f}(t), \mathbf{u}\rangle . \tag{2.1}$$

We define the convective operator $\mathcal{C}$ (on some suitable, sufficiently regular, Sobolev space) as

$$\langle \mathcal{C}\mathbf{v}, \mathbf{w}\rangle = \langle \nabla \cdot (\mathbf{u} \otimes \mathbf{v}), \mathbf{w}\rangle ,$$

for some fixed divergence-free velocity field $\mathbf{u}$. Integration by parts, together with the assumption that the resulting boundary terms vanish, then yields

$$\begin{aligned}\langle \mathcal{C}\mathbf{v}, \mathbf{w}\rangle &= \int_\Omega u_n(\partial_n v_m) w_m \, d\mathbf{x} \\ &= -\int_\Omega v_m \partial_n (u_n w_m) \, d\mathbf{x} \\ &= -\int_\Omega u_n (\partial_n w_m) v_m \, d\mathbf{x} \\ &= -\langle \mathbf{v}, \mathcal{C}\mathbf{w}\rangle .\end{aligned} \tag{2.2}$$

Which shows that the convective operator is skew-adjoint (or skew-symmetric). It follows that the convective term does not yield a contribution to (2.1).

Similarly, integration by parts results in showing that the Laplace operator is a self-adjoint (or symmetric) operator. Moreover it is negative semi-definite, since

$$\langle \Delta\mathbf{u}, \mathbf{u}\rangle = \int_\Omega (\partial_n \partial_n u_m) u_m \, d\mathbf{x} = -\int_\Omega (\partial_n u_m)(\partial_n u_m) \, d\mathbf{x} = -\|\nabla \mathbf{u}\|^2.$$

The term in (2.1) involving the pressure vanishes since the velocity field is divergence free. This yields the following energy equality

$$\frac{1}{2}\frac{d}{dt}\|\mathbf{u}\|^2 = -\frac{1}{\mathrm{Re}}\|\nabla \mathbf{u}\|^2 + \langle \mathbf{f}, \mathbf{u}\rangle . \tag{2.3}$$

This then shows that, in the absence of a forcing term, the energy decreases monotonically. The first term on the right-hand side is called the total rate of dissipation, and is denoted by

$$\epsilon(t) := \frac{1}{\mathrm{Re}}\|\nabla \mathbf{u}\|^2.$$

Moreover the power input resulting from the forcing term is denoted by

$$P(t) := \langle \mathbf{f}, \mathbf{u}\rangle .$$

Hence we can reformulate the kinetic energy balance as

$$\frac{d}{dt}E(t) = P(t) - \epsilon(t). \tag{2.4}$$

Energy (in-) equalities are often a first step for showing existence and uniqueness of solutions to the weak form of the NSE (this will be discussed briefly in Section 2.4). But they are also considered a desirable (in-)equality to be maintained in a discretisation. We will consider this in Section 4.2 where we derive an extension to a symmetry-preserving (Verstappen and Veldman, 2003) (symmetry preserving in the sense of skew- and self-adjointness of the convective and diffusive operator, respectively) discretisation of the NSE.

### 2.2.2 Frequency domain

Often the kinetic energy is considered in the frequency domain. Especially for (statistically) isotropic flow this leads to some simplifications.

We denote the Fourier transform as

$$\hat{u}(\mathbf{k},t) = \mathcal{F}u(\mathbf{k},t) := \int_{\mathbb{R}^3} u(\mathbf{x},t)e^{2\pi i\mathbf{k}\cdot\mathbf{x}}\, d\mathbf{x}.$$

Since the Fourier transform is an isometry on $L^2$ it follows that

$$E(t) = \frac{1}{2}\|\mathbf{u}\| = \frac{1}{2}\|\hat{\mathbf{u}}\|.$$

Let's consider a velocity field which is isotropic. For simplicity (without having to introduce an ensemble average of the velocity field) we consider this property to be defined as the Fourier transform of the velocity field to only depend on the magnitude $k$ of the wave vector $\mathbf{k}$. We can exploit the isotropy assumption when imposing a change of variables to spherical coordinates

$$\mathbf{k} = \mathbf{k}(k,\varphi,\vartheta).$$

This yields

$$E(t) = \int_0^\infty \pi k^2\phi(k,t)dk = \int_0^\infty E(k,t)dk,$$

where $\phi(k,t) = \frac{1}{2}|\hat{\mathbf{u}}(k,t)|^2$ is the local (in frequency space) energy corresponding to the wavenumber $k$. Moreover we defined the energy spectrum function as

$$E(k,t) := \pi k^2\phi(k,t).$$

This results in the following energy balance in the frequency domain (Pope, 2001, Section 6.6)

$$\frac{\partial}{\partial t}E(k,t) = P(k,t) - \frac{\partial}{\partial k}T(k,t) - \frac{2}{\mathrm{Re}}k^2E(k,t). \tag{2.5}$$

The term $T(k,t)$ represents the spectral transfer, interactions between wavenumbers, and results from the convective term.

In regions where the dissipation dominates, it follows that

$$\frac{\partial}{\partial t}E(k,t) = -\frac{2}{\mathrm{Re}}k^2E(k,t) \quad \Rightarrow \quad E(k,t) = e^{-\frac{2}{\mathrm{Re}}k^2(t-t_0)}E(k,t_0).$$

Hence whenever dissipation dominates the energy balance, the energy at wavenumber $k$ decays exponentially fast at a rate proportional to $k^2$.

*Relation to total kinetic energy*

Since the kinetic energy per wavenumber is a more detailed desciption of kinetic energy as compared to considering the total kinetic energy, we can derive the energy equality (2.3) from the spectral energy equality (2.5).

We let

$$P(t) = \int_0^\infty P(k,t)dk,$$

and moreover note that (Pope, 2001, Section 6.6) the convective contribution vanishes

$$\int_0^\infty \frac{\partial}{\partial k}T(k,t)dk = T(\infty,t) - T(0,t) = 0.$$

From the isotropy assumption it follows that

$$\begin{aligned}\|\nabla \mathbf{u}\|^2 &= \|\widehat{\nabla \mathbf{u}}\|^2 \\ &= -\int_{\mathbb{R}^3} \sum_{m,n=1}^{3} k_m^2 \hat{u}_n^2 d\mathbf{k} \\ &= -2\int_{\mathbb{R}^3} |\mathbf{k}|^2 \phi(|\mathbf{k}|, t) d\mathbf{k} \\ &= -2\int_0^\infty k^2 E(k,t) dk.\end{aligned}$$

Hence integration of (2.5), over $k \in [0, \infty)$, yields the previously encountered energy balance given by (2.4).

## 2.3 Theory of turbulence

### 2.3.1 Statistical analysis

Since solutions from the (M)NSE are given by time-dependent three-dimensional vector fields, it follows that resulting solutions become hard to study and or quantify. Often simplifying assumptions, such as homogeneity and isotropy of the velocity field, are made to reduce the complexity of the problem.

Homogeneity and isotropy are considered in a statistical sense (Pope, 2001, Section 3.7). A velocity field is considered statistically homogeneous if all statistics are invariant under translations. Similarly, a velocity field is said to be statistically isotropic if the statistics are invariant under rotations. Statistics are obtained by computing some mean, denoted by $\langle \cdot \rangle$. Here we initially consider the ensemble average, which is defined as

$$\langle f(\mathbf{x}, t) \rangle_N = \frac{1}{N} \sum_{r=1}^{N} f^{(r)}(\mathbf{x}, t),$$

where $f^{(r)}(\mathbf{x}, t)$ denotes the $r$-th measurement of $f$. That is, it is defined as repeating a single experiment $N$ times, and then computing the mean value.

In numerical simulations this ensemble average is replaced by a suitable spatial or temporal average. For example in fully developed turbulent channel flow, the average could be taken over time and the spanwise direction. Moreover, when considering decaying HIT, the average may be taken in all spatial directions.

We now define some useful correlation functions, assuming that we indeed have a statistically homogeneous and isotropic velocity field.

*Two-point correlation functions*

The two-point (single-time) correlation function, denoted by $R_{mn}(\mathbf{r}, t)$, is given by

$$R_{mn}(\mathbf{r}, t) := \langle u_m(\mathbf{x}, t) u_n(\mathbf{x} + \mathbf{r}, t) \rangle ,$$

where $\langle \cdot \rangle$ now denotes a spatial average in all directions. $\mathbf{r}$ is some displacement. Note that often we consider the (dimensionless) normalisation of $R_{mn}(\mathbf{r}, t)$ instead

$$\tilde{R}_{mn}(\mathbf{r}, t) := \frac{R_{mn}(\mathbf{r}, t)}{\left(R_{mm}(\mathbf{0}, t) R_{nn}(\mathbf{0}, t)\right)^{1/2}}.$$

From the definition of $R_{mn}(\mathbf{r},t)$ it follows that

$$R_{mn}(-\mathbf{r},t) = R_{nm}(\mathbf{r},t),$$

hence the diagonal entries are even functions in terms of the displacement $\mathbf{r}$. Moreover, provided the velocity field is divergence free, it follows that

$$\frac{\partial R_{mn}(\mathbf{r},t)}{\partial r_m} = 0 = \frac{\partial R_{mn}(\mathbf{r},t)}{\partial r_n}.$$

As is shown in Pope (2001, Section 6.3), due to isotropy, the normalised two-point correlation function is completely defined by two functions $f(r,t)$ and $g(r,t)$

$$\tilde{R}_{mn}(\mathbf{r},t) = g(|\mathbf{r}|,t)\delta_{mn} + (f(|\mathbf{r}|,t) - g(|\mathbf{r}|,t))\,\frac{r_m r_n}{|\mathbf{r}|^2}. \tag{2.6}$$

Considering the special case where $\mathbf{r} = r\mathbf{e}_l$, we obtain the following

$$\tilde{R}_{mn}(r\mathbf{e}_l,t) = \begin{cases} f(r,t), & \text{if} \quad m=n=l \\ g(r,t), & \text{if} \quad m=n\neq l \\ 0, & \text{if} \quad m\neq n \end{cases}.$$

Hence we call $f$ the normalised longitudinal two-point correlation function, and correspondingly $g$ is called the normalised transversal two-point correlation function. Differentiating (2.6) with respect to $r_m$, and subsequently summing over $m$ yields

$$0 = \frac{\partial \tilde{R}_{mn}(\mathbf{r},t)}{\partial r_m} = \frac{r_n}{|\mathbf{r}|^2}\left(f(|\mathbf{r}|,t) - g(|\mathbf{r}|,t) + \frac{|\mathbf{r}|}{2}\left.\frac{\partial f(r,t)}{\partial r}\right|_{r=|\mathbf{r}|}\right),$$

from which it follows that

$$g(r,t) = f(r,t) + \frac{r}{2}\frac{\partial f(r,t)}{\partial r}. \tag{2.7}$$

Hence the normalised two-point correlation tensor $\tilde{\mathbf{R}}(\mathbf{r},t)$, for homogeneous and isotropic turbulence, is entirely determined by the longitudinal two-point correlation function $f$, via (2.6) and (2.7).

We can take the simplification one step further by deriving two length scales from the correlation functions $f$ and $g$. First of all we define the integral length scale (for the longitudinal correlation function) as

$$L_f = \int_0^\infty f(r,t)dr.$$

Complementary to this integral length scale, we can also consider which "small" length scale is of importance. Hence we consider the Taylor series expansion of $f$ around $r=0$, this yields

$$f(r,t) = f(0,t) + f'(0,t)r + \frac{f''(0,t)}{2}r^2 + \mathcal{O}(r^3) = 1 + \frac{f''(0,t)}{2}r^2 + \mathcal{O}(r^3),$$

note that the first derivative vanishes since the function is even about $r=0$. For small $r$, the correlation function is thus determined by $\frac{f''(0,t)}{2}$. Since the second derivative has dimensions $m^{-2}$ ($f$ is dimensionless), it follows that we obtain the length scale

$$\lambda_f = \sqrt{\left|\frac{f''(0,t)}{2}\right|^{-1}} = \sqrt{-\frac{2}{f''(0,t)}},$$

which is called the Taylor microscale. Hence for small $r$, the Taylor microscale, still being a function of time, completely determines $\tilde{\mathbf{R}}(\mathbf{r}, t)$ in the case of decaying HIT.

The physical interpretation of such Taylor microscales is not very clear, it is often described as "an average length scale at which dissipation is relevant". However due to the previous discussion, where in the idealised case of decaying HIT we showed that for small increments the Taylor microscale determines the two-point correlation function, we consider the Taylor microscale as an important characterisation of a velocity field.

*Structure functions*

Given a multi-index $\mathbf{m} = (m_1, \ldots, m_l)$, the $l$-th order structure function is defined as (Pope, 2001, Section 6.2)

$$D_{\mathbf{m}}(\mathbf{r}, t) := \left\langle \prod_{i=1}^{|\mathbf{m}|} (u_{m_i}(\mathbf{x} + \mathbf{r}, t)) - u_{m_i}(\mathbf{x}, t)) \right\rangle.$$

For longitudinal structure functions (that is, $\mathbf{r} = r\mathbf{e}_i$ with $i = m_1 = \ldots = m_l$) we introduce the simplifying notation (letting $i = 1$)

$$D_l^L(r, t) := D_{\mathbf{1}}(r\mathbf{e}_1, t), \quad \mathbf{1} = (1, \ldots, 1)^T \in \mathbb{R}^l,$$

which can be non-dimensionalised, resulting in

$$\tilde{D}_l^L(r, t) := \frac{D_l^L(r, t)}{(D_2^L(r, t))^{l/2}}.$$

Similar to the previously discussed two-point correlation tensor $\mathbf{R}(\mathbf{r}, t)$, the second-order structure function, when considering a homogeneous and isotropic velocity field, is given by (Pope, 2001, Section 6.2)

$$D_{mn}(\mathbf{r}, t) = b(r, t)\delta_{mn} + (a(r, t) - b(r, t))\frac{r_m r_n}{|\mathbf{r}|^2},$$

where $a$ and $b$ are the longitudinal and transversal second-order structure functions respectively, related by

$$b(r, t) = a(r, t) + \frac{r}{2}\frac{\partial a(r, t)}{\partial r}.$$

In the next section we discuss how the previously introduced two-point correlation and structure functions may be used together with Kolmogorov's hypotheses.

### 2.3.2 Kolmogorov's Theory of Turbulence

Kolmogorov was a Russian mathematician who published a series of papers on turbulence in the year 1941 (Kolmogorov, 1941)(hence this theory is often called "K41 theory"). The theory is based on three hypotheses (see also McDonough (2004); Pope (2001)) which are presented here.

*Hypotheses*

The first of the hypotheses states that for a sufficiently large Reynolds number, contrary to large-scale motions (this characteristic length scale will be denoted by $\mathcal{L}$), small-scale motions are statistically isotropic.

**Hypothesis 2.1** (Local isotropy)**.** *For sufficiently high Reynolds number, small-scale turbulent motions, with length scale $l \ll \mathcal{L}$, are statistically isotropic.*

**Hypothesis 2.2** (Similarity 1)**.** *For sufficiently high Reynolds number, statistics of small-scale turbulent motions, with length scale $l \ll \mathcal{L}$, have a universal form, which is entirely determined by the viscosity $\nu$ and the energy dissipation rate $\epsilon$.*

Provided with this characterisation of small-scale turbulent motions, dimensional analysis yields length-, velocity- and timescales (called Kolmogorov scales), given by

$$\begin{aligned} \eta &:= (\nu^3/\epsilon)^{1/4}, \\ u_\eta &:= (\nu\epsilon)^{1/4}, \\ t_\eta &:= (\nu/\epsilon)^{1/2}. \end{aligned}$$

Note that the Reynolds number corresponding to these small scale motions equals one. The second similarity hypothesis supposes that turbulent motions of length scales much smaller than the characteristic length scale, but much larger than the Kolmogorov length scale, are not much affected by viscosity.

**Hypothesis 2.3** (Similarity 2)**.** *For sufficiently high Reynolds number, turbulent motions with length scale $\eta \ll l \ll \mathcal{L}$ have a universal form that is entirely determined by $\epsilon$.*

Corresponding to such length scales, we define wavenumber intervals. The wavenumber interval corresponding to $\eta \ll l \ll \mathcal{L}$ is called the inertial range, and will be denoted by $I_I = [k_{CI}, k_{ID})$. This leaves two remaining wavenumber intervals, given by the energy containing (or energy injection range) $I_C = [0, k_{CI})$ where the forcing term is relevant. And finally the dissipative range $I_D = [k_{ID}, \infty)$, where dissipation dominates the energy balance.

Integration of the energy balance (2.5) over the three different wavenumber intervals yield three balance equations under the assumptions that power input only acts on the energy containing range and dissipation is only significant in the dissipation range. These equations are shown in Figure 2.1 where we summarise the cascade of energy in HIT. Here $T_{CI}(t) = T(k_{CI}, t)$. The equations emphasise some properties mentioned before. In the energy containing range the power input is relevant, in the inertial range neither the power input nor dissipation is relevant hence yielding a wavenumber interval where transport mechanisms dominate the energy balance. The dissipation range is responsible for the dissipation of energy, hence acting as an energy drain.

*Consequences*

An important result, which follows from the Kolmogorov hypotheses, is the following. Consider a stationary turbulent flow at high Reynolds number, where the velocity field is statistically isotropic and homogeneous.

Then according to the second similarity hypothesis, the energy spectrum function $E(k)$ (no longer a function of time) is a function of $k$ and $\epsilon$, for $k \in I_I$. The dimensions of $E(k)$ are

$$[E(k)] = \frac{m^3}{s^2},$$

from which it follows that (Pope, 2001, Section 6.5)

$$E(k) \propto \epsilon^{2/3} k^{-5/3}, \quad k \in I_I. \tag{2.8}$$

The idealised case of stationary HIT in a box is hard to achieve in physical experiments. Hence instead we often consider, for the assessment of LES models, decaying HIT where there is no forcing. Hence the kinetic energy decays in time. Still (2.8) may be used as a method for verifying a numerical simulation.

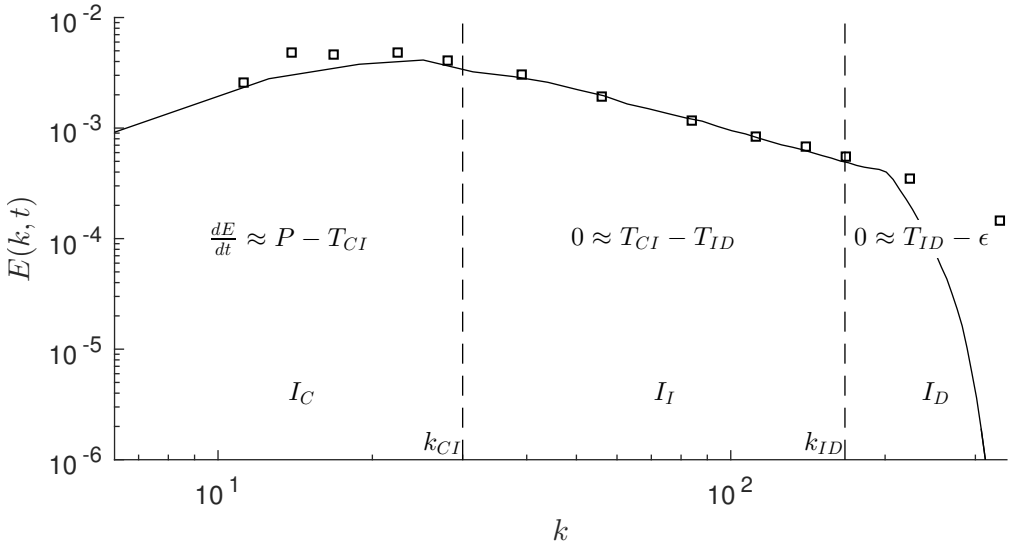


Figure 2.1: The energy spectrum function of an HIT velocity field resulting from a LES, together with data from a physical experiment. Qualitatively different wavenumber intervals $I_C$, $I_I$ and $I_D$ are shown, corresponding to the energy containing, intertial and dissipative wavenumber interval respectively. For each wavenumber interval we show, under some simplifying assumptions, the corresponding energy balance.

Better yet, in some physical experiments the kinetic energy, and even energy spectrum functions are measured and hence may be verified (Comte-Bellot and Corrsin, 1971). In Figure 2.1 we show the energy spectrum function of an HIT velocity field resulting from a LES, together with the data from the corresponding physical experiment. We will return to this experiment in Section 5.5.

A second application of Kologorov's hypotheses can be found in the structure functions. From the second similarity hypothesis, we find that the longitudinal structure functions satisfy (for $r$ in the inertial range)

$$D_l^L(r,t) = C_l(\epsilon r)^{l/3},$$

where the coefficients $C_l$ are universal constants. Hence for the non-dimensionalised $l$-th order longitudinal structure function we get

$$\tilde{D}_l^L(r,t) = \frac{C_l(\epsilon r)^{l/3}}{(C_2(\epsilon r)^{2/3})^{l/2}} = \left(\frac{C_l^{1/3}}{C_2^{1/2}}\right)^l =: \tilde{C}_l,$$

for $r$ in the inertial subrange.

## 2.4 Theory of the Navier-Stokes Equations

### 2.4.1 Weak formulation

Most solutions to the NSE are not sufficiently regular to appear in the strong form of the NSE, therefore we consider some weaker form of differentiability as we obtain by the definition of Sobolev spaces (see Appendix A.1). Obtaining a weak formulation to the NSE is done by taking the $L^2(\Omega)$ inner product of

the momentum equation with some smooth test function $\boldsymbol{\phi} \in [C^\infty_{0,\sigma}(\Omega \times [0,T))]^d$, and then integrating over the temporal domain $[0,T)$. This yields

$$\int_0^T \left\langle \partial_t \mathbf{u} + \mathbf{u} \cdot (\nabla \mathbf{u}) + \nabla p - \frac{1}{\mathrm{Re}} \Delta \mathbf{u} - \mathbf{f}, \boldsymbol{\phi} \right\rangle \, dt = 0. \tag{2.9}$$

Moreover (2.9) is made "as symmetric as possible" (w.r.t. the inner product) by using integration by parts

$$-\int_0^T \langle \mathbf{u}, \partial_t \boldsymbol{\phi} \rangle \, dt + \int_0^T \langle \mathbf{u} \cdot (\nabla \mathbf{u}), \boldsymbol{\phi} \rangle \, dt + \frac{1}{\mathrm{Re}} \int_0^T \langle \nabla \mathbf{u}, \nabla \boldsymbol{\phi} \rangle \, dt = \int_0^T \langle \mathbf{f}, \boldsymbol{\phi} \rangle \, dt + \langle \mathbf{u}_0, \boldsymbol{\phi}(0) \rangle \,. \tag{2.10}$$

Here we use either periodic or no-slip boundary conditions such that the boundary terms resulting from partial integration always vanish. The pressure term vanishes because the test function $\boldsymbol{\phi}$ is solenoidal which is exploited by partial integration.

Note that we can not (trivially) get an energy *equality* from (2.10) by substituting $\boldsymbol{\phi}$ with $\mathbf{u}$ since $\mathbf{u}$ may not be sufficiently regular for $\partial_t \mathbf{u}$ to exist in a strong sense. The following definition specifies a certain type of solution to the Navier-Stokes problem, and also provides an energy inequality which such solutions should satisfy.

**Definition 2.1** (Leray-Hopf weak solutions)**.** *A function $\mathbf{u} : \Omega \times [0,T] \to \mathbb{R}^d$ is called a weak solution to the Navier-Stokes equations* (1.2) *if*

1. $$\mathbf{u} \in L^\infty(0,T; L^2_\sigma(\Omega)) \cap L^2(0,T; H^1_{0,\sigma}(\Omega)),$$

2. $\forall \boldsymbol{\phi} \in [C^\infty_{0,\sigma}(\Omega \times [0,T))]^d$ *the function* $\mathbf{u}$ *satisfies* (2.10) *for* $T \to \infty$,

3. *the following energy inequality is satisfied for* $t \in [0,T]$

$$\frac{1}{2}\|\mathbf{u}(t)\|^2 + \frac{1}{\mathrm{Re}} \|\nabla \mathbf{u}\|^2_{L^2(0,t;L^2(\Omega))} \leq \frac{1}{2}\|\mathbf{u}_0\|^2 + \int_0^t \langle \mathbf{f}, \mathbf{u} \rangle \, dt. \tag{2.11}$$

In the next subsection we will state a theorem that claims the existence of such weak solutions. Indeed such a result can be proven. However, long-time existence *and* uniqueness of such solutions is still an open problem.

Besides playing an important role in proving existence theorems, energy inequalities of the form (2.11) also prove useful in studying the stability of certain LES models where equivalent energy inequalities (equivalent to the one mentioned above) are desired to ensure stability of a model.

### 2.4.2 Existence and uniqueness

One of the fundamental aspects of studying PDEs is the ability to prove existence and uniqueness of solutions. Actually, one of the seven Millennium Prize Problems is to prove the long time existence and uniqueness of solutions to the NSE.

An important result is the following (for a proof, see Berselli et al. (2005, pp. 47-51)).

**Theorem 2.1** (Existence of Leray-Hopf solutions)**.** *Given a smooth and bounded domain $\Omega \subset \mathbb{R}^3$, let the initial velocity field $\mathbf{u}_0$ and external forcing $\mathbf{f}$ be square integrable functions, hence*

$$\mathbf{u}_0 \in L^2_\sigma(\Omega), \quad \mathbf{f} \in L^2(0,T; L^2_\sigma(\Omega)).$$

*Then there exists a weak solution on $[0,T]$ in the sense of Leray-Hopf (see Definition 2.1) to the NSE.*

There are similar theorems proving existence *and uniqueness* of so called strong solutions, such solutions satisfy

$$\begin{cases} \mathbf{u} & \in & L^\infty(0,T;H^1_{0,\sigma}(\Omega)) \cap L^2(0,T;H^1_{0,\sigma}(\Omega) \cap [H^2(\Omega)]^d), \\ \partial_t \mathbf{u} & \in & L^2(0,T;L^2_\sigma(\Omega)). \end{cases}$$

However such solutions can only be shown to exist for "short time" (the end time $T$ is inversely proportional to the Reynolds number cubed (Berselli et al., 2005, p. 56)). The challenge is to show existence of weak solutions that are not only sufficiently regular (as in Leray-Hopf weak solutions) but also exist for long time and are unique.

Interestingly, in some cases the addition of an LES model to the NSE results in the ability to indeed prove existence as well as uniqueness of solutions. An example is given by Ladyžhenskaya's proof (Berselli et al., 2005, Theorem 3.9, 3.16) of existence and uniqueness of the NSE equipped with Smagorinsky's model.

# Chapter 3

# LES modelling

This chapter gives an introduction to LES modelling. The first section describes some desirable properties of LES models, which may be used as guiding principles in developing LES models. The second section covers some existing LES models which are interesting for our discussion. Moreover we make the connection to the first section by discussing how well these models satisfy the desirable properties. In the final section we introduce a general framework of LES models which are, like the previously mentioned existing LES models, functions of the velocity gradient. Furthermore we show how the previously discussed LES models fit in this framework, and we discuss some its favourable properties.

## 3.1 Desirable properties

We repeat the MNSE

$$\begin{aligned} \nabla \cdot \mathbf{w} &= 0, \\ \partial_t \mathbf{w} + \nabla \cdot (\mathbf{w} \otimes \mathbf{w}) + \nabla q - \frac{1}{\mathrm{Re}} \Delta \mathbf{w} + \nabla \cdot \boldsymbol{\tau} &= \bar{\mathbf{f}}, \end{aligned}$$

which is a closed set of equations if $\boldsymbol{\tau} = \mathcal{A}(\mathbf{w})$ for some operator $\mathcal{A}$. Several approaches can be taken to determine a suitable operator, some models follow from purely physical arguments (like Smagorinsky's model), whereas a more mathematical approach can be taken as well (e.g. the Gradient model).

Yet another approach is more systematical, based on imposing conditions on the operator $\mathcal{A}$. Some of these conditions are derived either from properties of the exact sub-filter scale stress tensor, or from the NSE themselves (see also Berselli et al. (2005)). Some of these properties are listed below.

*Symmetry*

Perhaps the most obvious desired property is the symmetry of the model tensor, this follows simply from the fact that the exact sub-filter scale stress tensor is itself symmetric.

*Dimensional consistency*

The LES model should leave the MNSE dimensionally consistent. Hence the dimensions of $\boldsymbol{\tau}$ should be of a velocity squared, that is

$$[\tau_{mn}] = m^2 s^{-2}.$$

*Frame invariance*

Frame invariance consists of three properties which are all satisfied by the Navier-Stokes equations. Suppose we have a solution to the NSE given by

$$\mathbf{w}(\mathbf{x},t), \quad q(\mathbf{x},t). \tag{3.1}$$

The first property we consider is *translation invariance*. Given the solution (3.1), then the following also yields a solution to the NSE

$$\mathbf{w}'(\mathbf{x},t) := \mathbf{w}(\mathbf{x}+\mathbf{L},t), \quad q'(\mathbf{x},t) := q(\mathbf{x}+\mathbf{L},t),$$

for some fixed vector $\mathbf{L}$ (see B.1).

The second property is *rotation invariance*, which is defined as the invariance of a solution under a coordinate rotation. Again, given the solution (3.1), then so is

$$\mathbf{R}\mathbf{w}(\mathbf{R}^{-1}\mathbf{x},t), q(\mathbf{R}^{-1}\mathbf{x},t),$$

where $\mathbf{R}$ is some constant rotation matrix.

Finally Galilean invariance is defined as the invariance of solutions under Galilean boosts, that is

$$\mathbf{w}'(\mathbf{x},t) := \mathbf{w}(\mathbf{x}-\mathbf{U}t,t)+\mathbf{U}, \quad q'(\mathbf{x},t) := q(\mathbf{x}-\mathbf{U}t,t),$$

is also a solution to the NSE. Proofs of these frame invariance properties can be found in Appendix B.1.

*Energy (in-)equality*

As discussed before, Leray-Hopf weak solutions of the original NSE satisfy the energy inequality given by (2.11). This inequality clearly describes how the kinetic energy evolves in time. It is hence desirable for a LES model to admit a similar (and hence easy to interpret) energy inequality.

The contribution to the kinetic energy due to the LES model is given by the $L^2$-inner product of the contribution of the LES model to the momentum equation with the velocity field $\mathbf{w}$, and is called the sub-grid dissipation. It is given by

$$\epsilon_S := \langle \nabla \cdot \boldsymbol{\tau}, \mathbf{w} \rangle .$$

Assuming symmetry of $\boldsymbol{\tau}$, and vanishing boundary terms, this yields

$$\epsilon_S = -\langle \boldsymbol{\tau}, \mathbf{S} \rangle = -\int_\Omega \epsilon_{S,\text{loc}}\, d\mathbf{x},$$

where the local subgrid dissipation is defined as

$$\epsilon_{S,\text{loc}}(\mathbf{x},t) := \boldsymbol{\tau} : \mathbf{S}.$$

It follows that the kinetic energy balance of the MNSE is given by

$$\frac{d}{dt}E(t) = P(t) - \epsilon(t) - \epsilon_S(t).$$

An example of a LES model which has a similar energy inequality as the original NSE is an eddy viscosity model like Smagorinsky's model, see for instance Section 3.2.

*Stability*

The question of stability is twofold. First of all we have analytical stability, in the sense of, for example, the existence of weak solutions for long time and depending on not necessarily small initial data. On the other hand we have numerical stability properties, which are a result of the spatial discretisation and the temporal discretisation.

Having shown existence of solutions in some weak sense still requires some care to be taken when developing a discretisation. If conversely, it can be shown that analytical solutions blow up in finite time, then no numerical method can remedy this.

Maintaining some analytical properties (like energy (in-)equalities) in the discretisation goes a long way to yielding a stable simulation. Hence this will be one of the main criteria when we develop our discretisation in Section 4.2.

*Modelling consistency (a priori)*

An a priori consistency test is one where we consider the error made in approximating the exact sub-filter scale stress tensor $\boldsymbol{\tau}^{\text{Exact}}(\mathbf{u})$ with the model term.

It is important to realise that if a model performs well in a priori tests this is in no way a guarantee that such a model is suitable to be used as an LES model in practical situations (stability is not included in an a priori test). A case in point being the Gradient model (see Section 3.2.2 and Berselli et al. (2005, Section 7.1)).

*Accuracy (a posteriori)*

Testing the accuracy of an LES model can also be done using the result of a DNS simulation. Hence we desire that

$$\|\bar{\mathbf{u}} - \mathbf{w}\|$$

is small (tends to zero as the filter length tends to zero) for some suitable norm. Note that such an a posteriori test encompasses much more than just an accuracy test for the model since it also requires a suitable spatial discretisation, and a stable time stepping procedure.

As discussed in Section 2.3, often statistical laws (like the ones that follow from Kolmogorov's theory) are used in the verification of LES models.

## 3.2 Examples of LES models

Here we present a few LES models which are either often used or interesting and relevant for our discussion. We also consider whether the LES models satisfy the previously mentioned desirable properties.

### 3.2.1 Eddy viscosity models

An important class of LES models is given by so called "eddy viscosity models" in which the kinematic viscosity $\nu$ is increased by a so called *eddy viscosity* (or *turbulent viscosity*) $\nu_T$. Eddy viscosity models are justified by the following hypothesis stated by Boussinesq in 1877

> *" Turbulent fluctuations are dissipative in the mean. "*

This yields the following LES model where only the traceless part of the exact sub-filter scale tensor is modelled

$$\boldsymbol{\tau}^{\text{EV}} = -2\nu_T^{\text{EV}}\mathbf{S},$$

where $\nu_T^{\text{EV}}$ is the eddy viscosity which is yet to be determined. It follows that the resulting local subgrid dissipation is given by

$$\epsilon_{S,\text{loc}}^{\text{EV}} = 2\nu_T^{\text{EV}}|\mathbf{S}|^2,$$

indeed yielding an increase (provided that $\nu_T^{\text{EV}}$ is positive) in the total viscosity.

*Smagorinsky's model*

Smagorinsky's model is an eddy viscosity model where $\nu_T$ is given by

$$\nu_T^{\text{Smag}} = (C_S\delta)^2\sqrt{2}|\mathbf{S}|.$$

Here $C_S$ is called Smagorinsky's constant (a constant which is hypothesised to be universal, and often taken equal to $0.17$ (Berselli et al., 2005, Section 3.2)), and $\delta$ is the filter length.

Let's consider whether this model is satisfactory in the sense of the desirable properties stated in the previous section. Symmetry and dimensional consistency are trivially satisfied. So are translational and Galilean invariance, since the model depends only on the velocity *gradient*. Rotational invariance follows from the transformation rule of the velocity gradient (B.1), which is given by

$$\nabla\mathbf{w}' = \mathbf{R}(\nabla\mathbf{w})\mathbf{R}^{-1}.$$

It follows that the same property holds for the symmetric and skew-symmetric parts of the velocity gradient. This transformation rule is identical to the one for the exact sub-filter scale stress tensor (assuming the filtering operation is rotation invariant as well), since

$$\mathbf{w}' \otimes \mathbf{w}' = \mathbf{R}(\mathbf{w} \otimes \mathbf{w})\mathbf{R}^{-1}.$$

Moreover an invariant like $|\mathbf{S}|$ is invariant under this transformation as well. Hence the Smagorinsky model satisfies the three frame invariance properties.

Regarding the existence of solutions it can be shown (Berselli et al., 2005, Theorem 3.9 & 3.16) that there exists a *unique* solution to the MNSE equipped with Smagorinsky's model (assuming sufficient regularity of the initial data and forcing, but not smallness), for which

$$\mathbf{w} \in H^1(0,T;L^2_\sigma(\Omega)) \cap L^3(0,T;W^{1,3}_{0,\sigma}(\Omega)).$$

Such solutions satisfy the following energy *equality*

$$\frac{1}{2}\frac{d}{dt}\|\mathbf{w}\|^2 + \frac{2}{\text{Re}}\|\mathbf{S}\|^2 + (C_S\delta)^2\|\mathbf{S}\|^3_{L^3(\Omega)} = \left\langle \bar{\mathbf{f}}, \mathbf{w} \right\rangle.$$

Hence the introduction of Smagorinsky's model gives desirable properties like the existence of unique solutions (which exist for long time) which moreover satisfy an energy equality, as opposed to an energy inequality. This also leads to the question of the stability of the model. The above results (unique solutions satisfying an energy equality for "large" initial data) analytically guarantee stability since the solution does not blow up in finite time.

The Smagorinsky model is accurate in the sense that $\mathbf{w} \to \mathbf{u}$ as $\delta \to 0$ (in some weak sense) provided that the energy dissipation rate is sufficiently regular (Berselli et al., 2005, Theorem 3.25)

$$\epsilon(t) \in L^2(0,T).$$

Since the eddy viscosity $\nu_T$ in Smagorinsky's model is non-negative, it follows that only the forward transfer (from the resolved to the unresolved scales of motion) of energy is modelled. This might not be sufficient since we know that there is also energy transfer from sub-filter scales to the resolved scales, backward transfer (also called backscatter). However in terms of numerical stability this is a favourable property.

*QR model*

The aforementioned Smagorinsky model is a commonly used LES model due to its simplicity but also because it yields stable simulations. However, it is also often noted that Smagorinsky's model is *too* dissipative. This raises the following question (Verstappen, 2011)

> *"How much eddy viscosity is sufficient for the dissipation of sub-grid scale energy? "*

Successfully answering this question yields an LES model which is sufficiently dissipative to ensure that any sub-grid scales produced by the convective term are dissipated sufficiently fast.

The aforementioned question is answered by the following eddy viscosity model

$$\boldsymbol{\tau}^{\mathrm{QR}} = -2\nu_T^{\mathrm{QR}}\mathbf{S}, \quad \nu_T^{\mathrm{QR}} = C_\delta \frac{\max(r,0)}{q},$$

where

$$r = -\frac{1}{3}\mathrm{tr}(\mathbf{S}^3), \quad q = \frac{1}{2}\mathrm{tr}(\mathbf{S}^2),$$

are two invariants of the symmetric part of the velocity gradient. The constant $C_\delta$ is the Poincaré constant of the corresponding control volume (and hence really a constant for uniform meshes) and is equal to the inverse of the smallest eigenvalue of the Laplace operator on such a control volume. It is given by

$$C_\delta = \delta^2/\pi^2,$$

if we take the filter width equal to the mesh size. For a derivation, see Verstappen (2011).

### 3.2.2 Nonlinear LES models

*Gradient model*

The Gradient LES model, also known as the Clark model, is a LES model which follows from the mathematical approach called "closure based on wavenumber asymptotics" or "approximate deconvolution" (Berselli et al., 2005, Section 7.1). The model follows from approximating the Fourier transform of $\boldsymbol{\tau}^{\mathrm{Exact}}(\mathbf{u})$ with the first term of its Taylor series expansion. A derivation can be found in Berselli et al. (2005, Section 7.1), the resulting approximation is then given by

$$\boldsymbol{\tau}^{\mathrm{Exact}}(\mathbf{u}) = \frac{\delta^2}{2\gamma}\nabla\mathbf{u}(\nabla\mathbf{u})^T + \mathcal{O}(\delta^4),$$

hence giving an $\mathcal{O}(\delta^4)$ approximation to the exact sub-filter scale stress tensor. The Gradient model is then given by

$$\boldsymbol{\tau}^{\mathrm{Grad}} = \frac{\delta^2}{2\gamma}\nabla\mathbf{w}(\nabla\mathbf{w})^T.$$

And the MNSE with the Gradient LES model are then given by

$$\begin{aligned} \nabla\cdot\mathbf{w} &= 0, \\ \partial_t\mathbf{w} + \nabla\cdot(\mathbf{w}\otimes\mathbf{w}) + \nabla q - \frac{1}{\mathrm{Re}}\Delta\mathbf{w} + \nabla\cdot\left[\frac{\delta^2}{12}\nabla\mathbf{w}(\nabla\mathbf{w})^T\right] &= \bar{\mathbf{f}}, \end{aligned} \tag{3.2}$$

for the common choice of $\gamma = 6$. Moreover, the local sub-grid dissipation is given by

$$\epsilon_{S,\mathrm{loc}}^{\mathrm{Grad}} = \frac{\delta^2}{12}(\nabla\mathbf{w}(\nabla\mathbf{w})^T) : \mathbf{S},$$

which is not necessarily positive. Hence we find that the Gradient LES model is not purely dissipative and hence also backward transfer of energy is modeled.

It is well known that the Gradient LES model leads to finite time blow up of the solution to the MNSE when it is used in the absence of an additional eddy viscosity model* (Berselli et al., 2005; Vreman et al., 1996). In Vreman et al. (1996) the one-dimensional analogue of the MNSE was considered. This yields the Burgers Equation supplemented with the term $\partial_x(\partial_x w)^2$, given by

$$\partial_t w + \frac{1}{2}\partial_x(w^2) = \nu\partial_x^2 w - \frac{1}{2}\eta\partial_x(\partial_x w)^2 + f(x).$$

There it is shown that this equation is linearly unstable around the steady-state solution $w = \sin(x)$ in the absence of viscosity ($\nu = 0$). Moreover it can be shown that whenever $\nu > \eta + 1$, the equation becomes linearly stable around this same steady state solution.

Similar to the aforementioned one-dimensional Burgers Equation, the Gradient LES model can be stabilised by supplementing it with an additional dissipative term. This yields the following MNSE

$$\begin{aligned} \nabla \cdot \mathbf{w} &= 0, \\ \partial_t \mathbf{w} + \nabla \cdot (\mathbf{w} \otimes \mathbf{w}) + \nabla q - \frac{1}{\mathrm{Re}}\Delta \mathbf{w} + \nabla \cdot \left[\frac{\delta^2}{12}\nabla \mathbf{w}(\nabla \mathbf{w})^T - C_G|\nabla \mathbf{w}|\nabla \mathbf{w}\right] &= \bar{\mathbf{f}}, \end{aligned} \tag{3.3}$$

for some constant $C_G$. In Berselli et al. (2005, Section 7.1) it is shown that whenever $C_G > \delta^2/6$ there exists a weak solution to (3.3) which satisfies

$$\mathbf{w} \in H^1(0,T;L^2_\sigma(\Omega)) \cap L^3(0,T;W^{1,3}_{0,\sigma}(\Omega)).$$

Note that this extended LES model (3.3) does not satisfy one of the basic properties an LES model ought to have: it is not symmetric. It is still an open question whether it is possible to replace $\nabla \mathbf{w}$ with $\mathbf{S}(\mathbf{w})$, while maintaining such an existence result (and hence the same stabilising property) as we obtain when using the original term $\nabla \mathbf{w}$.

The Gradient model is a good example of a LES model which seems very promising in terms of modeling consistency but turns out to be unstable unless a sufficient amount of dissipation is added.

*Gradient model - projection*

Instead of adding a sufficient amount of eddy viscosity to obtain a stable simulation one could also desire to have an LES model which has both (an approximation to) the modeling consistency of the Gradient model in combination with the dissipative (and hence stabilising) property of Smagorinsky's model. Hence, the projection of the Gradient model onto the symmetric part of the velocity gradient is computed. This model is then given by (Verstappen, 2011)

$$\boldsymbol{\tau}^{\text{Proj}} = -2\nu_T^{\text{Proj}}\mathbf{S}, \quad \nu_T^{\text{Proj}} = \frac{\delta^2}{2\gamma}\frac{\max(r,0)}{q},$$

where again $r$ is "clipped" such that the eddy viscosity is non-negative. For the common choice of $\gamma = 6$ this yields a slightly smaller eddy viscosity than $\boldsymbol{\tau}^{\text{QR}}$ does.

Note that such a projection implicitly defines the following decomposition of the Gradient model (without clipping)

$$\boldsymbol{\tau}^{\text{Grad}} = \boldsymbol{\tau}^{\text{Proj}} + \boldsymbol{\tau}^{\perp},$$

where $\boldsymbol{\tau}^{\perp}$ is the non-dissipative (orthogonal to $\tilde{\boldsymbol{\tau}}_1$) part of the Gradient model, representing some transport mechanism.

*Existence (and uniqueness) of solutions to (3.2) can be shown, however they are very restrictive in the sense that the norms of the forcing $\bar{\mathbf{f}}$ and initial data $\mathbf{w}_0$ should be bounded by $\delta^2$ (Berselli et al., 2005, Theorem 7.3).

*Rational LES model*

The derivation of the Gradient LES model is based upon approximation of the Fourier transform of the Gaussian filter kernel $\widehat{g_\delta}(\mathbf{k}, t)$ (and its reciprocal) with their corresponding Taylor series expansion (up to and including the $\delta^2$ terms). That is (for $\gamma = 6$)

$$e^{-\delta^2 k^2/24} = 1 - \frac{\delta^2 k^2}{24} + \mathcal{O}((\delta k)^4).$$

This approximation is rather poor as $\delta k \to \infty$.

Alternatively, one could also approximate $\widehat{g_\delta}(\mathbf{k}, t)$ with its $(0, 1)$-Padé approximant (hence *rational* LES model). This yields

$$e^{-\delta^2 k^2/24} = \frac{1}{1 + \delta^2 k^2/24} + \mathcal{O}((\delta k)^4).$$

This approximation results in the Rational LES model (Berselli et al., 2005, Section 7.2). In Figure 3.1 we compare the two approximations to the Gaussian filter kernel. Note that asymptotically, as $\delta k \to \infty$, the Rational LES model yields better results as compared to the Gradient model.

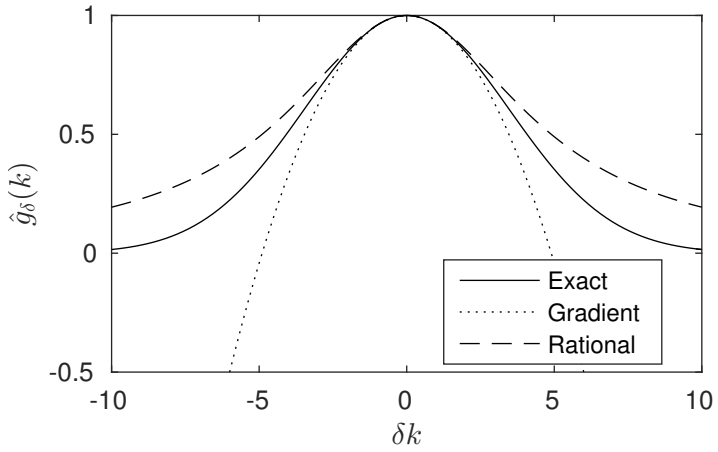


Figure 3.1: Two different approximations of the Fourier transform of the Gaussian filter kernel.

We do not consider the Rational LES model in what follows, however it's worth mentioning that the Gradient LES model is merely one example of general class of LES models which are all based on making approximations of the filter kernel in Fourier space.

## 3.3 A general framework of LES models

In this section we introduce a family of LES models based on the velocity gradient, which encompasses the previously discussed Smagorinsky, Gradient and QR model.

Earlier work by e.g. Lund and Novikov (1993) (introduced the symmetrisation of the nonlinear terms), Speziale (1991) (statistical approach, included nonlinear closure models), and Kosovic (1997) also considered nonlinear LES modeling with a similar approach as is presented here, but without orthogonalisation of the resulting symmetrised terms.

### 3.3.1 LES models based on the velocity gradient

Motivated by the success of the aforementioned LES models we consider a sub-grid scale model which is simply a function of the velocity gradient tensor $\nabla \mathbf{w}$ (the previously mentiond Smagorinsky, Gradient and QR model are all of this form). Equivalently, we assume our tensor model $\boldsymbol{\tau}$ to be of the form

$$\boldsymbol{\tau} = \mathcal{T}(\mathbf{S}, \boldsymbol{\Omega}),$$

for some function $\mathcal{T}$. Recall that $\mathbf{S}$ and $\boldsymbol{\Omega}$ are given by the symmetric and skew-symmetric part of the velocity gradient respectively. The most general expression which follows from this assumption is given by a polynomial expansion where each term is given by some product of powers of $\mathbf{S}$ and $\boldsymbol{\Omega}$. However, from the desired symmetry of the sub-grid scale model and from the Cayley-Hamilton theorem it follows that there are only eleven symmetrised terms left (Lund and Novikov, 1993). These terms are then given by

$$\begin{array}{lcllcl}
\boldsymbol{\tau}_1 &=& \mathbf{S}, & \boldsymbol{\tau}_2 &=& \mathbf{S}^2, \\
\boldsymbol{\tau}_3 &=& \boldsymbol{\Omega}^2, & \boldsymbol{\tau}_4 &=& \mathbf{S}\boldsymbol{\Omega} - \boldsymbol{\Omega}\mathbf{S}, \\
\boldsymbol{\tau}_5 &=& \mathbf{S}^2\boldsymbol{\Omega} - \boldsymbol{\Omega}\mathbf{S}^2, & \boldsymbol{\tau}_6 &=& \mathbf{S}\boldsymbol{\Omega}^2 + \boldsymbol{\Omega}^2\mathbf{S}, \\
\boldsymbol{\tau}_7 &=& \boldsymbol{\Omega}\mathbf{S}\boldsymbol{\Omega}^2 - \boldsymbol{\Omega}^2\mathbf{S}\boldsymbol{\Omega}, & \boldsymbol{\tau}_8 &=& \mathbf{S}\boldsymbol{\Omega}\mathbf{S}^2 - \mathbf{S}^2\boldsymbol{\Omega}\mathbf{S}, \\
\boldsymbol{\tau}_9 &=& \mathbf{S}^2\boldsymbol{\Omega}^2 + \boldsymbol{\Omega}^2\mathbf{S}^2, & \boldsymbol{\tau}_{10} &=& \boldsymbol{\Omega}\mathbf{S}^2\boldsymbol{\Omega}^2 - \boldsymbol{\Omega}^2\mathbf{S}^2\boldsymbol{\Omega},
\end{array} \tag{3.4}$$

together with the identity tensor $\boldsymbol{\tau}_0 = \mathbf{I}$. Moreover the associated invariants are given by

$$\begin{array}{lcllcl}
\beta_1 &=& \mathrm{tr}(\mathbf{S}^2), & \beta_2 &=& \mathrm{tr}(\boldsymbol{\Omega}^2), \\
\beta_3 &=& \mathrm{tr}(\mathbf{S}^3), & \beta_4 &=& \mathrm{tr}(\mathbf{S}\boldsymbol{\Omega}^2), \\
\beta_5 &=& \mathrm{tr}(\mathbf{S}^2\boldsymbol{\Omega}^2), & \beta_6 &=& \mathrm{tr}(\mathbf{S}^2\boldsymbol{\Omega}^2\mathbf{S}\boldsymbol{\Omega}),
\end{array} \tag{3.5}$$

where $\mathrm{tr}(\boldsymbol{\tau})$ denotes the trace of $\boldsymbol{\tau}$, that is, the sum of the diagonal elements. A family of tensor models is then given by

$$\boldsymbol{\tau} = \sum_{l=0}^{10} \alpha_l(\mathbf{x}, t)\boldsymbol{\tau}_l,$$

for coefficients $\alpha_l(\mathbf{x}, t)$, which depend on only the six invariants in order to satisfy rotational invariance of the model. The previously mentioned LES models can now be reformulated as

$$\begin{aligned}
\boldsymbol{\tau}^{\mathrm{Smag}} &= -2(C_S\delta)^2\sqrt{2\beta_1}\boldsymbol{\tau}_1, \\
\boldsymbol{\tau}^{\mathrm{Grad}} &= \frac{\delta^2}{12}(\boldsymbol{\tau}_2 - \boldsymbol{\tau}_3 - \boldsymbol{\tau}_4), \\
\boldsymbol{\tau}^{\mathrm{QR}} &= -\frac{4\delta^2 \max(-\beta_3, 0)}{3\pi^2\beta_1}.
\end{aligned}$$

For the original 11 tensors some terms are already orthogonal w.r.t. the local tensor inner product. Direct computation shows that the Gram matrix, defined by

$$G_{kl} := \tilde{\boldsymbol{\tau}}_k : \tilde{\boldsymbol{\tau}}_l,$$

has the following sparsity pattern (assuming a divergence-free velocity field)

$$\mathbf{G} = \begin{bmatrix}
\bullet & & \bullet & \bullet & & & \bullet & & & \bullet & \\
 & \bullet & \bullet & \bullet & & & \bullet & & & \bullet & \bullet \\
\bullet & \bullet & \bullet & \bullet & & & \bullet & \bullet & & \bullet & \\
\bullet & \bullet & \bullet & \bullet & & & \bullet & & \bullet & \bullet & \\
 & & & & \bullet & \bullet & & \bullet & \bullet & \bullet & \bullet \\
 & & & & \bullet & \bullet & \bullet & \bullet & \bullet & & \bullet \\
\bullet & \bullet & \bullet & \bullet & & \bullet & \bullet & & & \bullet & \bullet \\
 & & \bullet & & \bullet & \bullet & & \bullet & \bullet & \bullet & \bullet \\
 & & & \bullet & \bullet & \bullet & & \bullet & \bullet & \bullet & \bullet \\
\bullet & \bullet & \bullet & \bullet & \bullet & & \bullet & \bullet & \bullet & \bullet & \\
 & \bullet & & & \bullet & \bullet & \bullet & \bullet & \bullet & & \bullet
\end{bmatrix}.$$

Note that, for example, $\boldsymbol{\tau}_4$ (fifth column) is already orthogonal to the first four tensors, hence due to it's orthogonality w.r.t. $\boldsymbol{\tau}_1$ yielding no direct contribution to the kinetic energy.

### 3.3.2 Orthogonalisation

Suppose we orthogonalise the model terms $\boldsymbol{\tau}_l$, giving the orthogonalised terms $\tilde{\boldsymbol{\tau}}_l$ which satisfy

$$\tilde{G}_{kl} = \tilde{\boldsymbol{\tau}}_k : \tilde{\boldsymbol{\tau}}_l = |\tilde{\boldsymbol{\tau}}_k|^2 \delta_{kl}.$$

We now redefine the family of tensor models as

$$\boldsymbol{\tau} = \sum_{l=0}^{10} \alpha_l(\mathbf{x}, t) \tilde{\boldsymbol{\tau}}_l. \tag{3.6}$$

This family of model tensors is equivalent to the previous one since the proposed orthogonalisation is merely a change of basis. Considering the model in this form yields some favourable properties, one of which follows from considering the contribution to the kinetic energy by the tensor model, which is now given by

$$\epsilon_{S,\text{loc}} = -\boldsymbol{\tau} : \mathbf{S} = -\alpha_1(\mathbf{x}, t)\beta_1, \tag{3.7}$$

due to the orthogonality of the model terms. Hence orthogonalisation of the terms yields a family of models for which the sub-grid dissipation is easy to understand (equivalent to that of an eddy viscosity model), and is entirely determined by only the coefficient $\alpha_1(\mathbf{x}, t)$.

Assuming a model of the form (3.6), we obtain the following energy equality

$$\frac{1}{2}\frac{d}{dt}\|\mathbf{w}\|^2 + \frac{2}{\text{Re}}\|\mathbf{S}\|^2 - \int_\Omega \alpha_1(\mathbf{x}, t)\beta_1 \, d\mathbf{x} = \left\langle \bar{\mathbf{f}}, \mathbf{w} \right\rangle \tag{3.8}$$

hence if we consider for instance a Smagorinsky type model

$$\alpha_1(\mathbf{x}, t) = -C\sqrt{\beta_1}, \quad C \geq 0,$$

we get

$$\frac{1}{2}\frac{d}{dt}\|\mathbf{w}\|^2 + \frac{2}{\text{Re}}\|\mathbf{S}\|^2 + C\|\mathbf{S}\|^3_{L^3(\Omega)} = \|\bar{\mathbf{f}}\|\|\mathbf{w}\|.$$

So in the absence of power input (so $\mathbf{f} = 0$) the kinetic energy monotonically decreases *independent* of the coefficients $\alpha_l$, $l > 1$. Even though these calculations are not formal, in the sense that we have not shown existence of solutions of sufficient regularity, it does show some favourable properties of using the orthogonalised model terms (in particular the orthogonalisation w.r.t. $\mathbf{S}$).

By construction the tensor model is symmetric. Moreover, the model is dimensionally consistent if

$$\begin{array}{lllllll} [\alpha_1] & = & m^2 s^{-1}, & [\alpha_2] & = & m^2, \\ [\alpha_3] & = & m^2, & [\alpha_4] & = & m^2, \\ [\alpha_5] & = & m^2 s, & [\alpha_6] & = & m^2 s, \\ [\alpha_7] & = & m^2 s^2, & [\alpha_8] & = & m^2 s^2, \\ [\alpha_9] & = & m^2 s^2, & [\alpha_{10}] & = & m^2 s^3. \end{array} \tag{3.9}$$

Frame invariance follows from (B.1) together with the assumption that the coefficients $\alpha_l(\mathbf{x}, t)$ follow from some functional dependence on the six invariants (3.5).

As mentioned before, the energy inequality is easy to understand and is entirely determined by the coefficient $\alpha_1$. If such an energy inequality is preserved in the discretisation, this will automatically give some form of numerical stability as well provided that the coefficient $\alpha_1$ is non-positive. This will be one of the requirements of the discretisation, see Section 4.2.

### 3.3.3 Employing physical consistency conditions to reduce the number of possible LES models

The desirable properties mentioned in Section 3.1 are not sufficient to reduce the number of possible LES models to perhaps a few classes of models which can subsequently be tested and compared.

Silvis and Verstappen (2015) considered a broader range of both physical and mathematical consistency conditions which can be imposed on this general framework of tensor models. Using such conditions we can make an a priori assessment of an existing LES model, or we can use it to construct a LES model by imposing these conditions and therefore reducing the number of possible LES models to, hopefully, only a few.

Without going into details, we mention a few of such conditions here. The frame invariance properties discussed before are extended by scaling invariance as well as the material frame-indifference condition (therein refered to as S5 and S6 respectively). Moreover in wall-bounded flows one can impose near-wall scaling conditions.

A more abstract approach imposes conditions on the LES model which state that the model should vanish for certain flow types if the exact sub-filter scale stress tensor also vanishes (Vreman, 2004).

Besides being able to list numerous desirable conditions, it is also important to decide which of these conditions are actually relevant and important enough to be imposed on the LES model.

# Chapter 4

# Discretisation of the general framework of LES models

We now have a general framework of LES models which we eventually, in Chapter 5, want to use in numererous numerical experiments. Therefore we need a spatial as well as a temporal discretisation method. The spatial discretisation will be focussed on the contribution to the momentum equation due to the LES model, that is, we discuss the discretisation of

$$\nabla \cdot \boldsymbol{\tau}, \tag{4.1}$$

where the LES model is then given by the general expression

$$\boldsymbol{\tau} = \sum_{l=0}^{10} \alpha_l(\mathbf{x}, t)\tilde{\boldsymbol{\tau}}_l.$$

The first section of this chapter discusses the spatial discretisation of the divergence operator, as well as the discretisation of the velocity gradient. Our discretisation method will be an extension of the symmetry-preserving Finite Volume (FV) discretisation by Verstappen and Veldman (2003).

Section 4.2 discusses several methods for the discretisation of the LES model, that is, methods for obtaining an approximation to $\boldsymbol{\tau}$ provided an approximation to the velocity gradient is given. All of the proposed methods are second-order accurate. Moreover we desire a discrete equivalent to the sub-grid dissipation expression given by (3.7). We try to obtain such properties while using a relatively small stencil.

In Section 4.3 we perform the validation of the proposed discretisation methods by verifying that they are indeed of second-order accuracy (or fourth-order after extrapolation). Based on these results, and by studying how well the numerical sub-grid dissipation mimics that of the analytical sub-grid dissipation we motivate our choice for a single method.

The temporal discretisation is discussed in Section 4.4. Here we again briefly discuss the importance of preserving conservation properties by performing simulations, which indeed show that obtaining a discrete equivalent to the expression for the sub-grid dissipation (3.7) yields stable simulations.

## 4.1 Spatial discretisation

The discretisation of the contribution due to the LES model is an extension to the fourth-order symmetry-preserving Finite Volume discretisation by Verstappen and Veldman (2003). Here the MNSE in discrete

form (discretised in space only) are given by

$$\begin{aligned} \mathbf{\Omega}\frac{d\mathbf{u}^h}{dt} + \mathbf{C}(\mathbf{u}^h)\mathbf{u}^h + \frac{1}{\mathrm{Re}}\mathbf{D}\mathbf{u}^h - \mathbf{M}^T\mathbf{p}^h + \mathbf{T}(\mathbf{u}^h) = 0, \\ \mathbf{M}\mathbf{u}^h = 0, \end{aligned}$$

where $\mathbf{u}^h$ and $\mathbf{p}^h$ are the vectors containing the discrete (in space) approximations to $u$ and $p$ respectively. The matrix $\mathbf{\Omega}$ is a diagonal matrix containing the volumes of the corresponding control volumes.

The discrete convection operator, represented in matrix form by $\mathbf{C}(\mathbf{u}^h)$, is constructed such that the skew-adjointness of the convective operator (2.2) is preserved, that is

$$\left(\mathbf{C}(\mathbf{u}^h)\mathbf{v}, \mathbf{w}\right) = -\left(\mathbf{v}, \mathbf{C}(\mathbf{u}^h)\mathbf{w}\right).$$

Similarly, the discrete diffusive operator satisfies the analogous self-adjointness property. A discretisation which preserves such symmetries in the MNSE is referred to as a "symmetry-preserving discretisation". Symmetries in this context of the MNSE should not be confused with properties like frame invariance discussed earlier, which are sometimes also called symmetries of the MNSE. For precise definitions of the discrete convective and diffusive operators we refer to Verstappen and Veldman (2003).

The new term we introduce here is $\mathbf{T}(\mathbf{u}^h)$, which represents the Finite Volume approximation of the contribution due to the LES model (4.1). The discretisation of this term will be discussed in the following sections.

### 4.1.1 Second-order Finite Volume discretisation

For simplicity we restrict ourselves to the two dimensional case, $d = 2$. The domain $\Omega$ is tessellated into a rectilinear grid, defined by the grid points $(x_i, y_j)$, where $i \in \{0, \ldots, N_x\}$ and $j \in \{0, \ldots, N_y\}$. The Finite Volume discretisation will be performed on a staggered grid, therefore the grid points naturally define the pressure control volumes

$$\Omega_{i,j} := [x_{i-1}, x_i] \times [y_{j-1}, y_j],$$

we call them pressure control volumes since they are the control volumes for the pressure/incompressibility equation. The mesh widths are denoted by

$$\Delta x_i := x_i - x_{i-1}, \quad \Delta y_j := y_j - y_{j-1}.$$

Moreover the $x$-momentum control volumes (shifted control volumes) are defined as

$$\Omega_{i+\frac{1}{2},j} := [x_{i-\frac{1}{2}}, x_{i+\frac{1}{2}}] \times [y_{j-1}, y_j],$$

where

$$x_{i+\frac{1}{2}} := x_i + \frac{1}{2}\Delta x_{i+1}.$$

See also Figure 4.1. The shifted mesh widths are defined as

$$\tilde{\Delta} x_i := x_{i+\frac{1}{2}} - x_{i-\frac{1}{2}},$$

and similarly for the $y$-momentum control volume.

*Discretisation of the divergence operator*

We consider the model problem, given by

$$\partial_t \mathbf{u} = -\nabla \cdot \boldsymbol{\tau}, \quad \mathbf{x} \in \Omega, \tag{4.2}$$

together with appropriate boundary conditions on $\Gamma = \partial\Omega$. Integration of (4.2) over the volume $\Omega_{i+\frac{1}{2},j}$ yields (for $m = 1$)

$$\frac{d}{dt}\int_{\Omega_{i+\frac{1}{2},j}} u \, d\Omega = -\int_{\Omega_{i+\frac{1}{2},j}} \partial_n \tau_{1n} \, d\Omega = -\int_{\Gamma_{i+\frac{1}{2},j}} \eta_n \tau_{1n} \, d\Gamma.$$

the second equality follows from Gauss's theorem, $\boldsymbol{\eta}$ is the outward pointing normal to the surface. Approximation of the integral on the left-hand side by the midpoint rule, gives

$$\frac{d}{dt}\int_{\Omega_{i+\frac{1}{2},j}} u \, d\Omega \approx |\Omega_{i+\frac{1}{2},j}| \frac{d(u)_{i,j}}{dt}.$$

We define the contribution of the tensor model to the $x$-momentum equation as

$$(T_1)_{i,j} := \int_{\Gamma_{i+\frac{1}{2},j}} \eta_n \tau_{1n} \, d\Gamma,$$

and similarly for the $y$-momentum equation

$$(T_2)_{i,j} := \int_{\Gamma_{i,j+\frac{1}{2}}} \eta_n \tau_{2n} \, d\Gamma.$$

Approximating $(T_1)_{i,j}$ by the midpoint rule yields a semi-discretisation of (4.2). This approximation is given by

$$(T_1)^{h'}_{i,j} = \Delta y_j[(\tau_{11})(x_{i+\frac{1}{2}}, y_{j-\frac{1}{2}}) - (\tau_{11})(x_{i-\frac{1}{2}}, y_{j-\frac{1}{2}})] + \tilde{\Delta} x_i[(\tau_{12})(x_i, y_j) - (\tau_{12})(x_i, y_{j-1})]. \tag{4.3}$$

We denote this approximation by a superscript $h'$ since it is not yet fully discretised, that is, $\boldsymbol{\tau}$ is still exact. Splitting the two contributions to $(T_1)^{h'}_{i,j}$ gives

$$(T_1)^{h'}_{i,j} = (T_{11})^{h'}_{i,j} + (T_{12})^{h'}_{i,j}.$$

We consider, for example, $(T_{11})^{h'}_{i,j}$ in more detail

$$(T_{11})^{h'}_{i,j} = (T_{11})_{i,j} + \Delta y_j^3[(\partial_{yy}\tau_{11})(x_{i+\frac{1}{2}}, y_{j-\frac{1}{2}}) - (\partial_{yy}\tau_{11})(x_{i-\frac{1}{2}}, y_{j-\frac{1}{2}})] + \mathcal{O}(\Delta y_j^5), \tag{4.4}$$

which initially seems to give a leading-order term of the discretisation error of order one (after dividing by the volume of the control volume). However, note that

$$\frac{(\partial_{yy}\tau_{11})(x_{i+\frac{1}{2}}, y_{j-\frac{1}{2}}) - (\partial_{yy}\tau_{11})(x_{i-\frac{1}{2}}, y_{j-\frac{1}{2}})}{\tilde{\Delta} x_i} = (\partial_{yyx}\tau_{11})(x_i, y_{j-\frac{1}{2}}) + \mathcal{O}(\tilde{\Delta} x_i^2). \tag{4.5}$$

Hence we actually have a fourth-order approximation to $(T_{11})_{i,j}$ (and second-order accurate after dividing by the volume of the control volume).

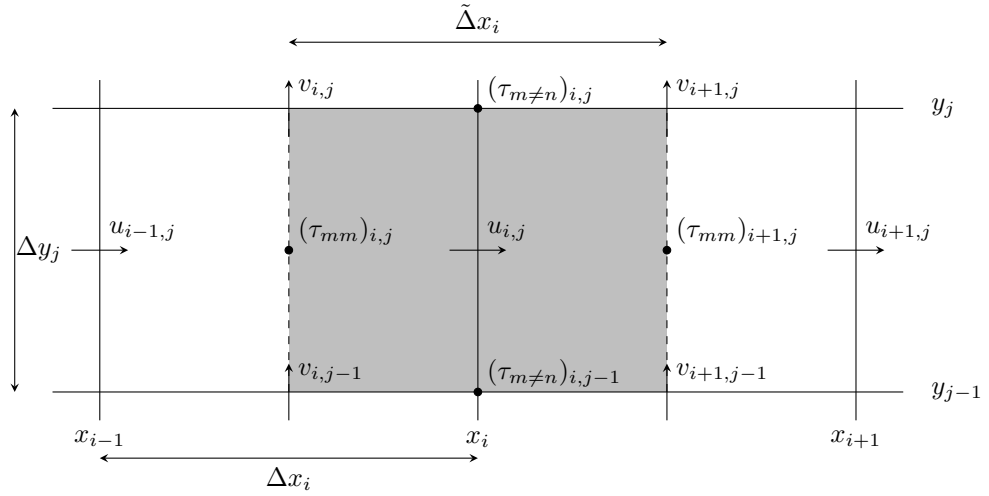


Figure 4.1: Staggered grid for the $x$-momentum equation. With $(\tau_{m\neq n})_{i,j}$ we emphasise that the off-diagonal elements are evaluated at the corners of the pressure control volumes. The shaded area equals $\Omega_{i+\frac{1}{2},j}$.

Using this second-order discretisation, we need the diagonal elements of $\boldsymbol{\tau}$ to be known at the centers of the pressure control volumes. Hence we define

$$(\tau_{mn})_{i,j} := (\tau_{mn})(x_{i-\frac{1}{2}}, y_{j-\frac{1}{2}}), \quad m = n.$$

Moreover the off-diagonal elements should be known at the "corners"* of the pressure control volumes, hence

$$(\tau_{mn})_{i,j} := (\tau_{mn})(x_i, y_j), \quad m \neq n.$$

See also Figure 4.1.

*Discretisation of the velocity gradient*

Since $\boldsymbol{\tau}$ is a function of the velocity gradient $\nabla \mathbf{u}$ we first consider the discretisation of $\nabla \mathbf{u}$, which is denoted by $(\nabla \mathbf{u})^h$. We approximate $\nabla \mathbf{u}$ by the second-order central discretisation, where we "pretend" the mesh is equidistant to preserve symmetry†. This gives for example

$$(\partial_x u)^h_{i,j} = \frac{u_{i,j} - u_{i-1,j}}{\Delta x_i} = (\partial_x u)_{i,j} + (\partial_{xxx} u)_{i-\frac{1}{2},j} \frac{\Delta x_i^2}{24} + \mathcal{O}(\Delta x_i^4).$$

Similar to (4.4) and (4.5) this actually yields a third-order leading term in the discretisation error when considering the difference between the fluxes through the opposing faces.

Hence we now have

$$(\nabla u_{mn})^h_{i,j} = (\nabla u_{mn})_{i,j} + \mathcal{O}(h^2).$$

*When generalising to $d = 3$, the off-diagonal elements are located at the midpoints of the edges. For example $(\tau_{12})_{i,j} := (\tau_{12})(x_i, y_j, z_{k-\frac{1}{2}})$.

†Such a discretisation results in conservation properties on a discrete level (Verstappen and Veldman, 2003), but the local truncation error is of first order (for non-uniform grids). It can be shown however (Manteuffel and White, 1986) that the solution is still second-order accurate.

We use $h$ to simplify the notation, one could view $h$ as the maximum over all mesh widths.

The staggered FV discretisation which was derived here satisfies the following property.

**Lemma 4.1.** *The FV discretisation of the divergence operator as given by* (4.3) *satisfies the following discrete equivalent to integration by parts, provided the boundary terms vanish*

$$\left(\mathbf{u}^h, \mathbf{T}(\mathbf{u}^h)\right) = \sum_{i,j=1}^{N} \left[(T_1)^h_{i,j} u_{i,j} + (T_2)^h_{i,j} v_{i,j}\right] = -h^2 \sum_{i,j=1}^{N} (\boldsymbol{\tau})^h_{i,j} : (\mathbf{S})^h_{i,j}, \tag{4.6}$$

*for uniform meshes with mesh width equal to $h$ and $N = N_x = N_y$ (for simplicity in notation).*

*Proof.* Let's consider the first term in the summation (for an arbitrary rectilinear mesh)

$$\begin{aligned}
\sum_{i,j=1}^{N_x,N_y} (T_1)^h_{i,j} u_{i,j} &= \sum_{i,j=1}^{N_x,N_y} \Delta y_j \left[(\tau_{11})^h_{i+1,j} - (\tau_{11})^h_{i,j}\right] u_{i,j} + \sum_{i,j=1}^{N_x,N_y} \tilde{\Delta} x_i \left[(\tau_{12})^h_{i,j} - (\tau_{12})^h_{i,j-1}\right] u_{i,j} \\
&= \sum_{i,j=1}^{N_x,N_y} (\tau_{11})^h_{i,j} \Delta y_j \left[u_{i-1,j} - u_{i,j}\right] + \sum_{i,j=1}^{N_x,N_y} (\tau_{12})^h_{i,j} \tilde{\Delta} x_i \left[u_{i,j} - u_{i,j+1}\right] \\
&\quad + \sum_{j=1}^{N_y} \Delta y_j \left[(\tau_{11})^h_{N_x+1,j} u_{N,j} - (\tau_{11})^h_{1,j} u_{0,j}\right] + \sum_{i=1}^{N_x} \tilde{\Delta} x_i \left[(\tau_{12})^h_{i,N_y} u_{i,N_y+1} - (\tau_{12})^h_{i,0} u_{i,1}\right].
\end{aligned}$$

Hence provided the velocity field is either periodic, or vanishing at the boundary, we get

$$\sum_{i,j=1}^{N_x,N_y} (T_1)^h_{i,j} u_{i,j} = - \sum_{i,j=1}^{N_x,N_y} \left[(\tau_{11})^h_{i,j} \Delta x_i \Delta y_j (\nabla u_{11})^h_{i,j} - (\tau_{12})^h_{i,j} \tilde{\Delta} x_i \tilde{\Delta} y_{j+1} (\nabla u_{12})^h_{i,j}\right].$$

Similar computations on

$$\sum_{i,j=1}^{N_x,N_y} (T_2)^h_{i,j} v_{i,j},$$

together with letting $N = N_x = N_y$ and assuming the mesh to be uniform, then yield (4.6). □

### 4.1.2 Fourth-order discretisation

To obtain a higher-order discretisation we need larger control volumes such that second-order accurate solutions on the fine and coarse grid can be combined to obtain a fourth-order accurate solution on the fine grid (as was done in Verstappen and Veldman (2003)). We define the three times larger control volumes for the $x$-momentum equation by

$$\Omega^3_{i+\frac{1}{2},j} := [x_{i-\frac{3}{2}}, x_{i+\frac{3}{2}}] \times [y_{j-2}, y_{j+1}].$$

The mesh widths are given by

$$\Delta^3 x_i := x_{i+1} - x_{i-2}, \quad \tilde{\Delta}^3 x_i := x_{i+\frac{3}{2}} - x_{i-\frac{3}{2}}.$$

Analogous definitions hold for the $y$-momentum equation. All quantities derived in Section 4.1 for the three times larger control volumes are defined analogously and are denoted by a superscript "three". For example

$$(\partial_x u)^{3h}_{i-1,j} = \frac{u_{i,j} - u_{i-3,j}}{\Delta^3 x_{i-1}} = (\partial_x u)_{i,j} + (\partial_{xxx} u)_{i-\frac{3}{2},j} \frac{\Delta^3 x^2_{i-1}}{24} + \mathcal{O}(\Delta^3 x^4_{i-1}).$$

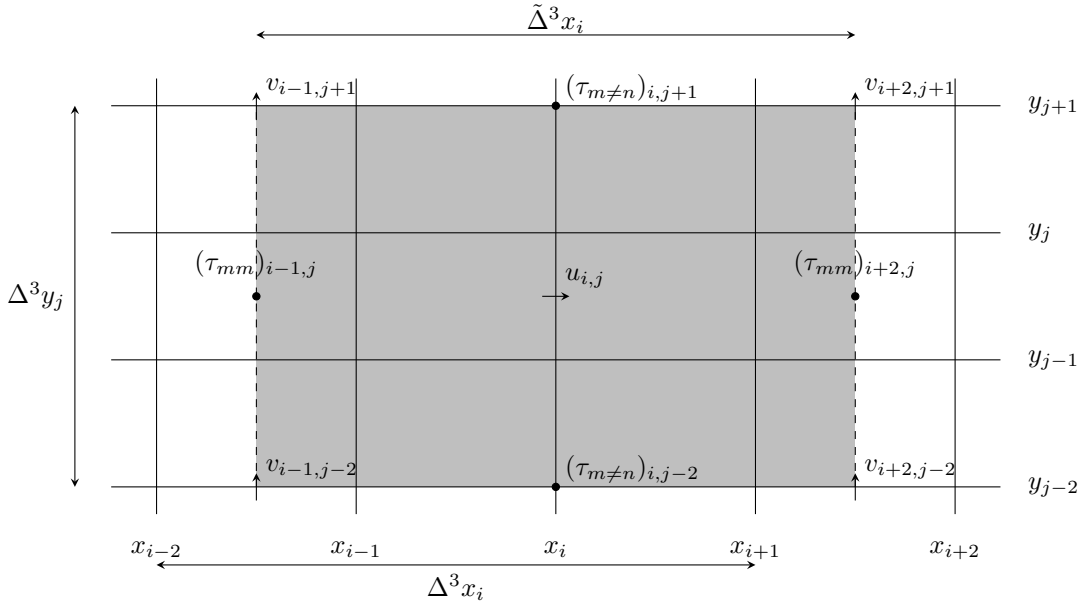


Figure 4.2: The three times larger control volume for the $x$-momentum equation. The shaded area equals $\Omega^3_{i+\frac{1}{2},j}$.

See also Figure 4.2. This yields the following discretisation error for the general $d$-dimensional case

$$(\mathbf{T})^{3h}_{i,j} = (\mathbf{T})_{i,j} + \mathbf{1}\mathcal{O}((3h)^{2+d}),$$

where $\mathbf{1}$ is the unit 3 by 1 vector. The discretisation errors can be made more precise by

$$(T_1)^h_{i,j} = (T_1)_{i,j} + (c_1)_{i,j}h^{2+d} + \mathcal{O}(h^{4+d}).$$

Similarly for the three times larger control volumes we have

$$(T_1)^{3h}_{i,j} = (T_1)_{i,j} + (c_1)_{i,j}(3h)^{2+d} + \mathcal{O}(h^{4+d}).$$

Hence we can extrapolate our approximation such that the leading-order term in the discretisation error is eliminated. We define our extrapolated approximation as

$$(\hat{T}_1)^{\text{ext}}_{i,j} := \frac{3^{2+d}(T_1)^h_{i,j} - (T_1)^{3h}_{i,j}}{3^{2+d}|\Omega_{i+\frac{1}{2},j}| - |\Omega^3_{i+\frac{1}{2},j}|} = (\hat{T}_1)_{i,j} + \mathcal{O}(h^4).$$

And similarly for the contribution to the $y$-momentum equation

$$(\hat{T}_2)^{\text{ext}}_{i,j} := \frac{3^{2+d}(T_2)^h_{i,j} - (T_2)^{3h}_{i,j}}{3^{2+d}|\Omega_{i,j+\frac{1}{2}}| - |\Omega^3_{i,j+\frac{1}{2}}|} = (\hat{T}_2)_{i,j} + \mathcal{O}(h^4).$$

The hat indicates that the contribution is divided by the volume of the control volume.

## 4.2 Discretisation of the LES model

In this section we propose several methods for discretising $\boldsymbol{\tau}^h$. Each of the methods is formally second-order accurate, however they differ in the error constant. More importantly they also differ in how a conservation law like (3.7) is preserved in the discretisation. This conservation law implies that the contribution to the kinetic energy by the tensor model should vanish whenever $\alpha_1 = 0$.

### 4.2.1 Criteria for the discretisation

*Accuracy and damping of high frequencies*

In the tensor model, terms of the form $\mathbf{S}^2$ and $\boldsymbol{\Omega}^2$ occur together with invariants which depend on for example $\mathbf{S}^3$. Such terms could be discretised by simply computing $((\mathbf{S})^h_{i,j})^2$, where

$$(\mathbf{S})^h_{i,j} := ((\nabla \mathbf{u})^h_{i,j} + (\nabla \mathbf{u}^T)^h_{i,j})/2.$$

However, since the elements of $(\mathbf{S})^h_{i,j}$ live on two different locations (similarly, four locations if $d = 3$), this would give only a first-order accurate approximation.

To obtain second-order accuracy we could compute the product by averaging wherever necessary such that only terms located at the same location are multiplied and added. We illustrate this by an example.

Consider computing $((\mathbf{S}^2)_{12})^h_{i,j}$, this yields

$$\begin{aligned}((\mathbf{S}^2)_{12})^h_{i,j} = \frac{(S_{11})^h_{i,j} + (S_{11})^h_{i+1,j} + (S_{11})^h_{i,j+1} + (S_{11})^h_{i+1,j+1}}{4}(S_{12})^h_{i,j} \\ + (S_{12})^h_{i,j}\frac{(S_{22})^h_{i,j} + (S_{22})^h_{i+1,j} + (S_{22})^h_{i,j+1} + (S_{22})^h_{i+1,j+1}}{4},\end{aligned}$$

which indeed gives a second-order accurate approximation. However when applying this approach to calculating an approximation to $\mathbf{S}^3$ by multiplying $\mathbf{S}^2$ and $\mathbf{S}$ we would have to average the elements of $\mathbf{S}^2$ again. Repeated averaging results in a larger stencil, and hence leads to damping (smoothing) of high frequencies. Therefore we would like to avoid such repeated averaging, however we must average *at least once* to be able to compute all the model terms.

To summarise: we want our discretisation to be second-order accurate and the number of interpolations should be limited (preferably only once).

*Numerical subgrid dissipation*

The second criterion we impose on our discretisation is related to the sub-grid dissipation $\epsilon_S$. Recall (3.7) where we found that (analytically) the sub-grid dissipation is entirely determined by the coefficient $\alpha_1$ and hence should vanish whenever the tensor model is orthogonal to $\mathbf{S}$. This desirable property should be preserved in our discretisation in the sense that, whenever $\alpha_1 = 0$, we should recover the symmetry-preserving property of the discretisation, which is given by Verstappen and Veldman (2003)

$$\frac{d}{dt}\frac{1}{2}\left(\mathbf{u}^h, \boldsymbol{\Omega}\mathbf{u}^h\right) = -\frac{1}{\mathrm{Re}}\left(\mathbf{u}^h, \mathbf{D}\mathbf{u}^h\right) \leq 0. \tag{4.7}$$

More generally we can use Lemma 4.1 to include the numerical sub-grid dissipation in the discrete energy equality (we will do this later for the specific methods). The numerical sub-grid dissipation is given by

$$\epsilon^h_S := \left(\mathbf{u}^h, \mathbf{T}(\mathbf{u}^h)\right) = -h^2 \sum_{i,j=1}^{N} (\boldsymbol{\tau})^h_{i,j} : (\mathbf{S})^h_{i,j}. \tag{4.8}$$

Note that recovering (4.7) whenever $\alpha_1 = 0$ is equivalent to stating that the numerical sub-grid dissipation $\epsilon_S^h$ should vanish if $\alpha_1 = 0$.

We will refer to this as "preserving the energy conservation properties of the MNSE".

### 4.2.2 Global properties of interpolation

Here we consider some properties related to linear interpolation. These properties will be used later on to show that our discretisation methods indeed preserve the energy conservation properties of the MNSE.

We start with $d = 1$ since the properties for any $d > 1$ then follow from this simple case. Consider two functions, say $f$ and $g$, defined on some closed interval $\Omega = [a, b] \subset \mathbb{R}$. Suppose we subdivide this interval into $N$ equally sized subintervals, hence yielding $N + 1$ nodes denoted by $x_i$. We also define the auxiliary centered nodes as

$$x_i^c := x_{i-\frac{1}{2}} = \frac{1}{2}(x_{i-1} + x_i),$$

and similarly we denote by a superscript at which location the function is evaluated, so

$$f_i^c = f(x_i^c).$$

Moreover we denote the original nodes by

$$x_i^o := x_i, \quad f_i^o = f(x_i^o).$$

We also introduce complementary notation for the interpolation operation. The interpolated approximation at the centered nodes, using values of $f$ at the original nodes, is given by

$$f_i^{o\to c} := \frac{1}{2}(f_{i-1}^o + f_i^o),$$

and similarly

$$f_i^{c\to o} := \frac{1}{2}(f_i^c + f_{i+1}^c).$$

Note that $f_i^{c\to o\to c} \neq f_i^c$, but rather

$$f_i^{c\to o\to c} = \frac{1}{4}f_{i-1}^c + \frac{1}{2}f_i^c + \frac{1}{4}f_{i+1}^c.$$

**Lemma 4.2.** *With the notation introduced previously, let $f$ and $g$ be any two functions defined on some interval $\Omega = [a, b]$. If $f$ and $g$ are either both periodic*

$$f(x + (b - a)) = f(x),$$

*or both vanish at the boundary*

$$f(a) = f(b) = 0$$

*then the following two properties hold*

1. $$\sum_{i=1}^{N} f_i^{o\to c} g_i^c = \sum_{i=1}^{N} f_i^o g_i^{c\to o},$$

2. $$\sum_{i=1}^{N} g_i^c = \sum_{i=1}^{N} g_i^{c\to o}.$$

*Proof.* 1.

$$\begin{aligned}\sum_{i=1}^{N} f_i^{o\to c} g_i^c &= \sum_{i=1}^{N} \frac{1}{2}\left(f_{i-1}^o + f_i^o\right) g_i^c \\ &= \frac{1}{2}\sum_{i=1}^{N} f_{i-1}^o g_i^c + f_i^o g_i^c \\ &= \frac{1}{2}\sum_{i=1}^{N} f_i^o g_{i+1}^c + f_i^o g_i^c \\ &= \sum_{i=1}^{N} f_i^o g_i^{c\to o}\end{aligned}$$

where we use

$$\begin{aligned}\sum_{i=1}^{N} f_{i-1}^o g_i^c &= \sum_{i=0}^{N-1} f_i^o g_{i+1}^c \\ &= \sum_{i=1}^{N} f_i^o g_{i+1}^c + (f_0^o g_1^c - f_N^o g_{N+1}^c).\end{aligned}$$

Note that the last term indeed vanishes if both $f$ and $g$ are either periodic or both vanish at the boundary.

2. Taking $f \equiv 1$ in the previous reasoning then shows the second property holds as well.

□

We are now ready to extend this result to higher dimensions, hence we consider the general case where

$$f, g : \Omega \in \mathbb{R}^d, \quad \Omega = [a_1, b_1] \times \ldots \times [a_d, b_d].$$

The yields the following $2^d$ interpolations for each node

$$\mathbf{x}_{i_1,\ldots,i_d}^{o\ldots o} = \mathbf{x}_{i_1,\ldots,i_d}, \quad \mathbf{x}_{i_1,\ldots,i_d}^{co\ldots o} = \mathbf{x}_{i_1-\frac{1}{2},i_2,\ldots,i_d}, \quad \ldots$$

Here $\mathbf{x}_{i_1,\ldots,i_d}$ denote the $(N_1+1)\cdot\ldots\cdot(N_d+1)$ nodes resulting from some rectilinear discretisation of $\Omega$, where we have $N_l$ intervals in the $l$-th spatial direction.

Analogously to the one-dimensional case we also introduce an averaging operation by

$$f_{\mathbf{i}}^{\mathbf{p}\to\mathbf{q}} = f_{\mathbf{i}}^{(p_1\to q_1)\ldots(p_d\to q_d)} := \left(f_{i_1,\ldots,i_{d-1}}^{(p_1\to q_1)\ldots(p_{d-1}\to q_{d-1})}\right)_{i_d}^{p_d\to q_d}, \quad \mathbf{p},\mathbf{q} \in \{o,c\}^d,$$

where no averaging is applied whenever $p_l = q_l$.

Using Lemma 4.2 we can now show the following.

**Lemma 4.3.** *Let $f$ and $g$ be any two functions defined on some $d$-dimensional domain $\Omega = [a_1, b_1] \times \ldots \times [a_d, b_d] \subset \mathbb{R}^d$. Let $f$ and $g$ be, per spatial direction $l = 1, \ldots, d$, both periodic*

$$f(\mathbf{x} + (b_l - a_l)\mathbf{e}_l) = f(\mathbf{x}), \quad l \in I_p \subset \{1, \ldots, d\}$$

*or both vanish at the boundary*

$$f(\mathbf{x}) = 0, \quad \mathbf{x} \in \left( \prod_{p \in \{1,\ldots,l-1,l+1,\ldots,d\}} [a_p, b_p] \right) \times \{a_l, b_l\}, \quad l \in I_d \subset \{1, \ldots, d\}.$$

*Here $I_p, I_d$ is some partitioning of the indices $1, \ldots, d$, and $\mathbf{e}_l$ is the $l$-th standard basis vector.*

*The following two properties then hold*

1. $$\sum_{\mathbf{i}=1}^{\mathbf{N}} f_{\mathbf{i}}^{\mathbf{p}\to\mathbf{q}} g_{\mathbf{i}}^{\mathbf{q}} = \sum_{\mathbf{i}=1}^{\mathbf{N}} f_{\mathbf{i}}^{\mathbf{p}} g_{\mathbf{i}}^{\mathbf{q}\to\mathbf{p}}, \quad \forall \mathbf{p}, \mathbf{q} \in \{o, c\}^d,$$

2. $$\sum_{\mathbf{i}=1}^{\mathbf{N}} g_{\mathbf{i}}^{\mathbf{q}} = \sum_{\mathbf{i}=1}^{\mathbf{N}} g_{\mathbf{i}}^{\mathbf{q}\to\mathbf{p}}, \quad \forall \mathbf{p}, \mathbf{q} \in \{o, c\}^d,$$

*where*

$$\sum_{\mathbf{i}=1}^{\mathbf{N}} f_{\mathbf{i}} = \sum_{i_1=1}^{N_1} \cdots \sum_{i_d=1}^{N_d} f_{i_1,\ldots,i_d}.$$

*Proof.* By construction the interpolation operation can be applied one spatial direction at a time. Hence repeated application of Lemma 4.2 gives the desired result. □

### 4.2.3 Two methods for discretising the model term

We will now consider two discretisation methods. Method 1 applies interpolation only once, however as it will turn out it does not preserve $\epsilon_S^h = 0$ if $\alpha_1 = 0$. An improvement to method 1 is considered which ensures that the sub-grid dissipation vanishes for $\alpha_1 = 0$.

A second method is considered which does preserve the energy conservation properties of the MNSE, however this method uses more than one interpolation.

We will consider (for simplicity in notation) the two-dimensional case. Before introducing the methods, we define the staggered locations in terms of the notation introduced in the previous Section.

$$\mathbf{x}_{i,j}^{(1)} := \mathbf{x}_{i,j}^{cc}, \quad \mathbf{x}_{i,j}^{(2)} := \mathbf{x}_{i,j}^{oo}.$$

Note that for $d = 3$, we would have four distinct locations, given by

$$\mathbf{x}_{i,j,k}^{(1)} := \mathbf{x}_{i,j,k}^{ccc}, \quad \mathbf{x}_{i,j,k}^{(2)} := \mathbf{x}_{i,j,k}^{ooc}, \quad \mathbf{x}_{i,j,k}^{(3)} := \mathbf{x}_{i,j,k}^{oco}, \quad \mathbf{x}_{i,j,k}^{(4)} := \mathbf{x}_{i,j,k}^{coo}.$$

When considering the velocity gradient in two dimensions (or any derived tensor) we note that from the FV discretisation each component has a location where it is defined in a natural way (that is, no interpolation is required to obtain an approximation at this location). The diagonal elements of $(\nabla \mathbf{u})_{i,j}^h$ are naturally defined at location $\mathbf{x}_{i,j}^{(1)}$, whereas the off-diagonal elements are defined at location $\mathbf{x}_{i,j}^{(2)}$. We define $(\nabla \mathbf{u}^{(p)})_{i,j}^h$ as the approximation to the velocity gradient at location $p$. When there is no superscript added, e.g. $(\nabla \mathbf{u})_{i,j}^h$, it is implied that the elements are located at their natural locations (staggered locations).

Provided with this notation, we now consider several methods for the discretisation of the LES model.

*Method 1.0*

Given the staggered velocity gradient $(\nabla \mathbf{u})^h_{i,j}$ we compute interpolated velocity gradients (interpolating whenever necessary) at locations one and two (similarly, four locations if $d = 3$). The next step is to compute the derived terms $\boldsymbol{\tau}_l$ and subsequently the orthogonalised terms $\tilde{\boldsymbol{\tau}}_l$ and their respective invariants. Then, in order to construct the staggered tensor model $\boldsymbol{\tau}$, we select the diagonal elements of $(\boldsymbol{\tau}^{(1)})^h_{i,j}$ and the off-diagonal elements of $(\boldsymbol{\tau}^{(2)})^h_{i,j}$ for the construction of $(\boldsymbol{\tau})^h_{i,j}$. The only averaging that occurs using this method is when the staggered velocity gradient is interpolated to the two locations. Hence this method is optimal with respect to the first criterion of using as little interpolation as possible. We show the construction of $(\boldsymbol{\tau})^h_{i,j}$ from $(\nabla \mathbf{u})^h_{i,j}$ schematically in Figure 4.3.

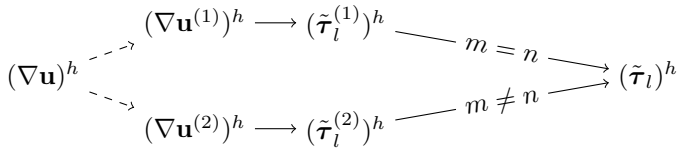


Figure 4.3: Schematic representation of Method 1.0. Dashed arrow implies some interpolation is required.

Method 1 orthogonalises the tensors at each location seperately. Provided that $\alpha_1 = 0$ this yields

$$(\boldsymbol{\tau}^{(p)})^h_{i,j} : (\mathbf{S}^{(p)})^h_{i,j} = 0, \quad p = 1, 2.$$

Unfortunately this does not imply that

$$(\boldsymbol{\tau})^h_{i,j} : (\mathbf{S})^h_{i,j} = 0. \tag{4.9}$$

However this is not a sensible requirement since (4.9) defines a summation over terms which are not located at the same position.

Rewriting (4.8) with the use of Lemma 4.3 yields (summation over $m, n$ is implied)

$$\begin{aligned} \epsilon_S^h &= -h^2 \sum_{i,j=1}^{N} \left[ (\tau_{m=n})^h_{i,j} (\mathbf{S}_{m=n})^h_{i,j} + (\tau_{m\neq n})^h_{i,j} (\mathbf{S}_{m\neq n})^h_{i,j} \right] \\ &= -h^2 \sum_{i,j=1}^{N} \left[ (\tau^{(1)}_{m=n})^h_{i,j} (\mathbf{S}^{(1)}_{m=n})^h_{i,j} + (\tau^{(2)}_{m\neq n})^h_{i,j} (\mathbf{S}^{(2)}_{m\neq n})^h_{i,j} \right] \\ &= -h^2 \sum_{i,j=1}^{N} \left[ (\tau^{(1)}_{m=n})^h_{i,j} (\mathbf{S}^{(1)}_{m=n})^h_{i,j} + \left\{ (\tau^{(2)}_{m\neq n})^h_{i,j} (\mathbf{S}^{(2)}_{m\neq n})^h_{i,j} \right\}^{(2)\to(1)} \right]. \end{aligned} \tag{4.10}$$

Demanding that the term between the square brackets to equal zero makes sense now since all terms are located (up to second order accuracy) at location 1. This term does not equal zero (in general) with method 1. However it does indicate that perhaps some alternative way of orthogonalisation may yield $\epsilon_S^h = 0$ for $\alpha_1 = 0$, which will be discussed next.

*Improving Method 1.0*

Let's consider now how we can orthogonalise an (arbitrary) staggered tensor $\boldsymbol{\eta}$ w.r.t. the staggered tensor $\mathbf{S}$ such that only the orthogonalisation coefficients are averaged and moreover

$$\sum_{i,j=1}^{N} (\boldsymbol{\eta})^h_{i,j} : (\mathbf{S})^h_{i,j} = 0.$$

Hence we assume

$$(\tau_{m=n})^h_{i,j} = (\eta^{(1)}_{m=n})^h_{i,j} - \gamma^{(1)}_{i,j}(S_{m=n})^h_{i,j},$$
$$(\tau_{m\neq n})^h_{i,j} = (\eta^{(2)}_{m\neq n})^h_{i,j} - \gamma^{(1)\to(2)}_{i,j}(S_{m\neq n})^h_{i,j}.$$

Using (4.10) it follows that the sub-grid dissipation is given by

$$-\frac{\epsilon^h_S}{h^2} = \sum_{i,j=1}^{N}\Bigg[(\eta^{(1)}_{m=n})^h_{i,j}(S^{(1)}_{m=n})^h_{i,j} + \left\{(\eta^{(2)}_{m\neq n})^h_{i,j}(S^{(2)}_{m\neq n})^h_{i,j}\right\}^{(2)\to(1)}$$
$$-\gamma^{(1)}_{i,j}(S^{(1)}_{m=n})^h_{i,j}(S^{(1)}_{m=n})^h_{i,j} - \left\{\gamma^{(1)\to(2)}_{i,j}(S^{(2)}_{m\neq n})^h_{i,j}(S^{(2)}_{m\neq n})^h_{i,j}\right\}^{(2)\to(1)}\Bigg].$$

Using Lemma 4.3 we get the following expression, where only coefficients $\gamma^{(p)}_{i,j}$ from location 1 occur

$$-\frac{\epsilon^h_S}{h^2} = \sum_{i,j=1}^{N}\Bigg[(\eta^{(1)}_{m=n})^h_{i,j}(S^{(1)}_{m=n})^h_{i,j} + \left\{(\eta^{(2)}_{m\neq n})^h_{i,j}(S^{(2)}_{m\neq n})^h_{i,j}\right\}^{(2)\to(1)}$$
$$-\gamma^{(1)}_{i,j}(S^{(1)}_{m=n})^h_{i,j}(S^{(1)}_{m=n})^h_{i,j} - \gamma^{(1)}_{i,j}\left\{(S^{(2)}_{m\neq n})^h_{i,j}(S^{(2)}_{m\neq n})^h_{i,j}\right\}^{(2)\to(1)}\Bigg].$$

Hence letting

$$\gamma^{(1)}_{i,j} = \frac{(\eta^{(1)}_{m=n})^h_{i,j}(S^{(1)}_{m=n})^h_{i,j} + \left\{(\eta^{(2)}_{m\neq n})^h_{i,j}(S^{(2)}_{m\neq n})^h_{i,j}\right\}^{(2)\to(1)}}{(S^{(1)}_{m=n})^h_{i,j}(S^{(1)}_{m=n})^h_{i,j} + \left\{(S^{(2)}_{m\neq n})^h_{i,j}(S^{(2)}_{m\neq n})^h_{i,j}\right\}^{(2)\to(1)}},$$

yields $\epsilon^h_S = 0$. This expression is merely an interpolated variant of the projection of $\mathbf{S}$ onto $\boldsymbol{\eta}$. We will refer to this improved method as "Method 1.1", whereas the "old" method 1 is referred to as "Method 1.0". Note that only the orthogonalisation with respect to $\mathbf{S}$ is replaced with the aforementioned method. In Figure 4.4 we summarise Method 1.1.

We also consider doing all of the orthogonalisation steps with this alternative method, we call this method "Method 1.2".

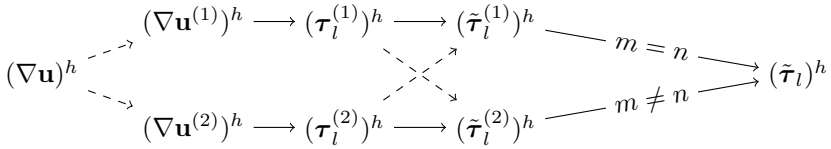


Figure 4.4: Schematic representation of Method 1.1. Dashed arrow implies some interpolation is required.

*Method 2.0*

With Method 2.0, we compute the velocity gradient only at location 1 (also if $d = 3$). Orthogonalisation is also done cell-centered at location 1, and finally the staggered tensor model is computed by interpolating *back* to the desired locations. It follows that the components of $(\boldsymbol{\tau})^h_{i,j}$ are defined as

$$(\tau_{m=n})^h_{i,j} = (\tau^{(1)}_{m=n})^h_{i,j}, \quad (\tau_{m\neq n})^h_{i,j} = \left\{(\tau^{(1)}_{m\neq n})^h_{i,j}\right\}^{(1)\to(2)}.$$

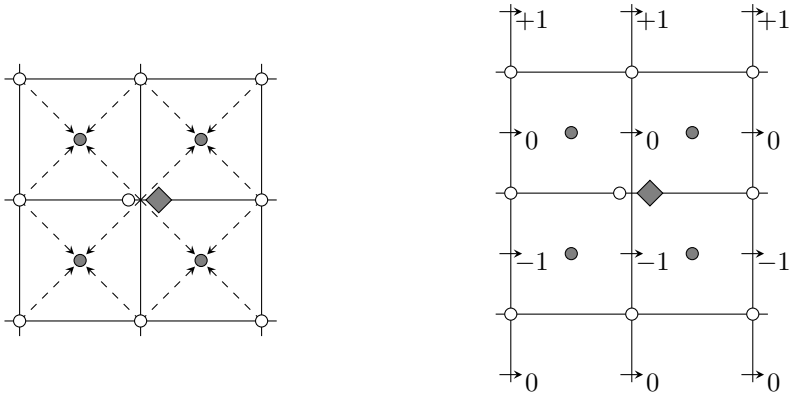


Figure 4.5: Left: illustration of the discretisation stencil resulting from method 2.0, the filled diamond $(\tau_{12})^h_{i,j}$ is averaged from the four closed circles which contain $(\tau^{(1)}_{12})^h$. The model tensor $(\boldsymbol{\tau}^{(1)})^h$ is derived from $(\nabla\mathbf{u}^{(1)})^h$ which in turn is interpolated from the staggered $(\nabla\mathbf{u})^h$ denoted by the open circles. Right: The vertical wave $u(x,y) = \sin(16y + \pi/4)$ represented on the grid.

This yields a second order accurate discretisation, as with Method 1.0, however interpolation is applied twice. In Figure 4.6 we summarise Method 2.0.

To get some indication as to how much the additional interpolation affects the accuracy we do an a priori test (numerical tests will be done later) in the following example.

**Example 4.1.** *We consider the velocity field to be given by* $u(x,y) = \sin(16y + \pi/4)$*, such that*

$$u(x_i, y_{j-\frac{1}{2}}) = \sin\left(16\left(\frac{2\pi}{64}(j-1/2)\right) + \pi/4\right) = \sin(j\pi/2).$$

*The wave is depicted in Figure 4.5 where the values of* $u$ *are shown. The left sub-figure shows how the value of* $(\tau_{12})^h$ *depends on* $(\nabla\mathbf{u})^h$*, the double averaging yields a nine point stencil. Where Method 1.0 would give* $((\boldsymbol{\tau}_1)_{12})^h_{i,j} = (S_{12})^h_{i,j}$*, Method 2.0 gives*

$$\begin{aligned}((\boldsymbol{\tau}_1)_{12})^h_{i,j} = \frac{1}{16}\big[&4(S_{12})^h_{i,j} + 2(S_{12})^h_{i-1,j} + 2(S_{12})^h_{i,j-1} + 2(S_{12})^h_{i,j+1} + 2(S_{12})^h_{i+1,j} \\ &+ (S_{12})^h_{i+1,j-1} + (S_{12})^h_{i-1,j-1} + (S_{12})^h_{i-1,j+1} + (S_{12})^h_{i+1,j+1}\big].\end{aligned}$$

*Hence for the example we consider here (where* $i,j$ *corresponds to the location of the diamond shape in Figure 4.5)*

$$((\boldsymbol{\tau}_1)_{12})^h_{i,j} = \frac{1}{16h}\left[4 + 2 - 2 + 2 + 2 - 1 - 1 + 1 + 1\right] = \frac{1}{2h},$$

*whereas Method 1.0 gives* $((\boldsymbol{\tau}_1)_{12})^h_{i,j} = 1/h$*. Hence for high frequencies the damping caused by the additional averaging may be quite severe.*

Method 2.0 does however naturally preserve the energy conservation properties of the MNSE, as we summarise in the following lemma.

**Lemma 4.4.** *Using Method 2.0, we obtain the following discrete energy equality, being the discrete analogue of* (3.8)*.*

$$\frac{d}{dt}\frac{1}{2}\left(\mathbf{u}^h, \boldsymbol{\Omega}\mathbf{u}^h\right) = -\frac{1}{\mathrm{Re}}\left(\mathbf{u}^h, \mathbf{D}\mathbf{u}^h\right) + h^2\sum_{i,j=1}^{N}(\alpha_1)_{i,j}|(\mathbf{S}^{(1)})^h_{i,j}|^2.$$

*Proof.* Let's consider computing the numerical sub-grid dissipation when using Method 2.0. Using (4.8), we get (summation over $m, n$ is implied)

$$\begin{aligned}
\epsilon_S^h &= -h^2 \sum_{i,j=1}^{N} (\boldsymbol{\tau})_{i,j}^h : (\mathbf{S})_{i,j}^h \\
&= -h^2 \sum_{i,j=1}^{N} \left[ (\tau_{m=n}^{(1)})_{i,j}^h (\mathbf{S}_{m=n}^{(1)})_{i,j}^h + (\tau_{m\neq n}^{(1)\to(2)})_{i,j}^h (\mathbf{S}_{m\neq n}^{(2)})_{i,j}^h \right] \\
&= -h^2 \sum_{i,j=1}^{N} \left[ (\tau_{m=n}^{(1)})_{i,j}^h (\mathbf{S}_{m=n}^{(1)})_{i,j}^h + (\tau_{m\neq n}^{(1)})_{i,j}^h (\mathbf{S}_{m\neq n}^{(2)\to(1)})_{i,j}^h \right] \\
&= -h^2 \sum_{i,j=1}^{N} (\boldsymbol{\tau}^{(1)})_{i,j}^h : (\mathbf{S}^{(1)})_{i,j}^h.
\end{aligned}$$

Hence letting

$$\boldsymbol{\tau} = \sum_{l=0}^{10} \alpha_l(\mathbf{x}, t) \tilde{\boldsymbol{\tau}}_l$$

we obtain

$$\epsilon_S^h = -h^2 \sum_{i,j=1}^{N} (\alpha_1)_{i,j} |(\mathbf{S}^{(1)})_{i,j}^h|^2.$$

□

$$(\nabla \mathbf{u})^h \dashrightarrow (\nabla \mathbf{u}^{(1)})^h \longrightarrow (\tilde{\boldsymbol{\tau}}_l^{(1)})^h \dashrightarrow (\tilde{\boldsymbol{\tau}}_l)^h$$

Figure 4.6: Schematic representation of Method 2.0. Dashed arrow implies some interpolation is required.

*Sub-grid dissipation after extrapolation*

What we want to discuss here is whether the vanishing sub-grid dissipation property is preserved when we extrapolate $\mathbf{T}(\mathbf{u}^h)$ to obtain fourth-order accuracy.

Up till now we have shown that both Method 1.1, 1.2 and 2.0 all preserve the energy conservation properties of the MNSE when considering a second-order approximation. This can be summarised as

$$\left( \mathbf{u}^h, \mathbf{T}^h(\mathbf{u}^h) \right) = 0,$$

for $\alpha_1 = 0$. We added an extra superscript $h$ to $\mathbf{T}$ to indicate that this is an approximation to $\mathbf{T}$ using the small control volumes of size $h$. Similarly we get an approximation on the three times larger control volumes, denoted by $\mathbf{T}^{3h}(\mathbf{u}^h)$. We let

$$\epsilon_S^{3h} = \left( \mathbf{u}^h, \mathbf{T}^{3h}(\mathbf{u}^h) \right),$$

where, equivalent to (4.8), we can show that

$$\epsilon_S^{3h} = -(3h)^2 \sum_{i,j=1}^{N} (\boldsymbol{\tau})_{i,j}^{3h} : (\mathbf{S})_{i,j}^{3h},$$

which also vanishes if $\alpha_1 = 0$. Hence for the extrapolated operator $\mathbf{T}^{\text{ext}}(\mathbf{u}^h)$ we have

$$\begin{aligned}\epsilon_S^{\text{ext}} &= \left(\mathbf{u}^h, \mathbf{T}^{\text{ext}}(\mathbf{u}^h)\right) \\ &= \frac{3^{2+d}}{3^{2+d}-1}\left(\mathbf{u}^h, \mathbf{T}^h(\mathbf{u}^h)\right) - \frac{1}{3^{2+d}-1}\left(\mathbf{u}^h, \mathbf{T}^{3h}(\mathbf{u}^h)\right) \\ &= \frac{3^{2+d}\epsilon_S^h - \epsilon_S^{3h}}{3^{2+d}-1},\end{aligned}$$

which also vanishes for $\alpha_1 = 0$.

## 4.3 Numerical validation

Now that we have established the theoretical properties of the previously mentioned discretisation methods, the next step is to validate these properties. We split the validation into two parts. First we confirm that the discretisation methods are indeed second- and fourth-order accurate. The second part concerns the sub-grid dissipation, which should vanish (or at least be relatively small as compared to a dissipative term), whenever $\alpha_1 = 0$.

### 4.3.1 Accuracy

We want to verify the second- and fourth-order accuracy of the discretisation methods from the previous section. In order to do so, we consider some periodic velocity field (not necessarily divergence free) $\mathbf{w}_0$. For this velocity field we compute both the exact[‡] contribution to the momentum equation, given by $\mathbf{T}(\mathbf{w}_0)$, as well as the approximation given by each of the four methods.

We define the relative $L^2$ error, using $N$ subintervals (yielding $N^3$ volumes, using a uniform grid) by

$$\varepsilon_{N,\text{Mi.j}} := \frac{\|\mathbf{T}(\mathbf{w}_0) - \mathbf{T}^h_{N,\text{Mi.j}}(\mathbf{w}_0)\|_{L^2(\Omega)}}{\|\mathbf{T}(\mathbf{w}_0)\|_{L^2(\Omega)}}, \tag{4.11}$$

where $\mathbf{T}^h_{N,\text{Mi.j}}(\mathbf{w}_0)$ denotes the Finite Volume approximation to $\mathbf{T}(\mathbf{w}_0)$ using method "Method i.j" on a uniform grid with $N^3$ volumes.

The initial velocity field is given by

$$\mathbf{w}_0(\mathbf{x}) = \begin{pmatrix} -\sin x + \cos y \\ \sin x + \cos z \\ \cos y + \sin z \end{pmatrix}, \quad \mathbf{x} \in \Omega = [0, 2\pi]^3.$$

The non-orthogonalised ($\boldsymbol{\tau}_l$, for $l = 1, \ldots, 10$), fourth-order results are shown in Figure 4.7 (for second-order results, see Appendix D.1). Note that we show only Methods 1.0 and 2.0, since without orthogonalisation Methods 1.0, 1.1 and 1.2 are equivalent.

As expected, due to the additional averaging, Method 2.0 is always less accurate than Method 1.0. However both methods are confirmed to be fourth-order accurate. This can easily be seen by the agreement of the slopes, which all tend to $4$ as $h$ becomes smaller.

Next we test the orthogonal terms. We only show $\tilde{\boldsymbol{\tau}}_l$, for $l = 2, \ldots, 5$, since $\tilde{\boldsymbol{\tau}}_1$ poses no challenge for the discretisation, whereas for $l > 5$ the terms vanish (for this particular velocity field) since the space of symmetric $3 \times 3$ tensors is spanned by 6 terms (including the identity tensor $\boldsymbol{\tau}_0$). The results are shown in Figure 4.8.

[‡]The analytical expressions are evaluated using `MATLAB`'s symbolic toolbox.

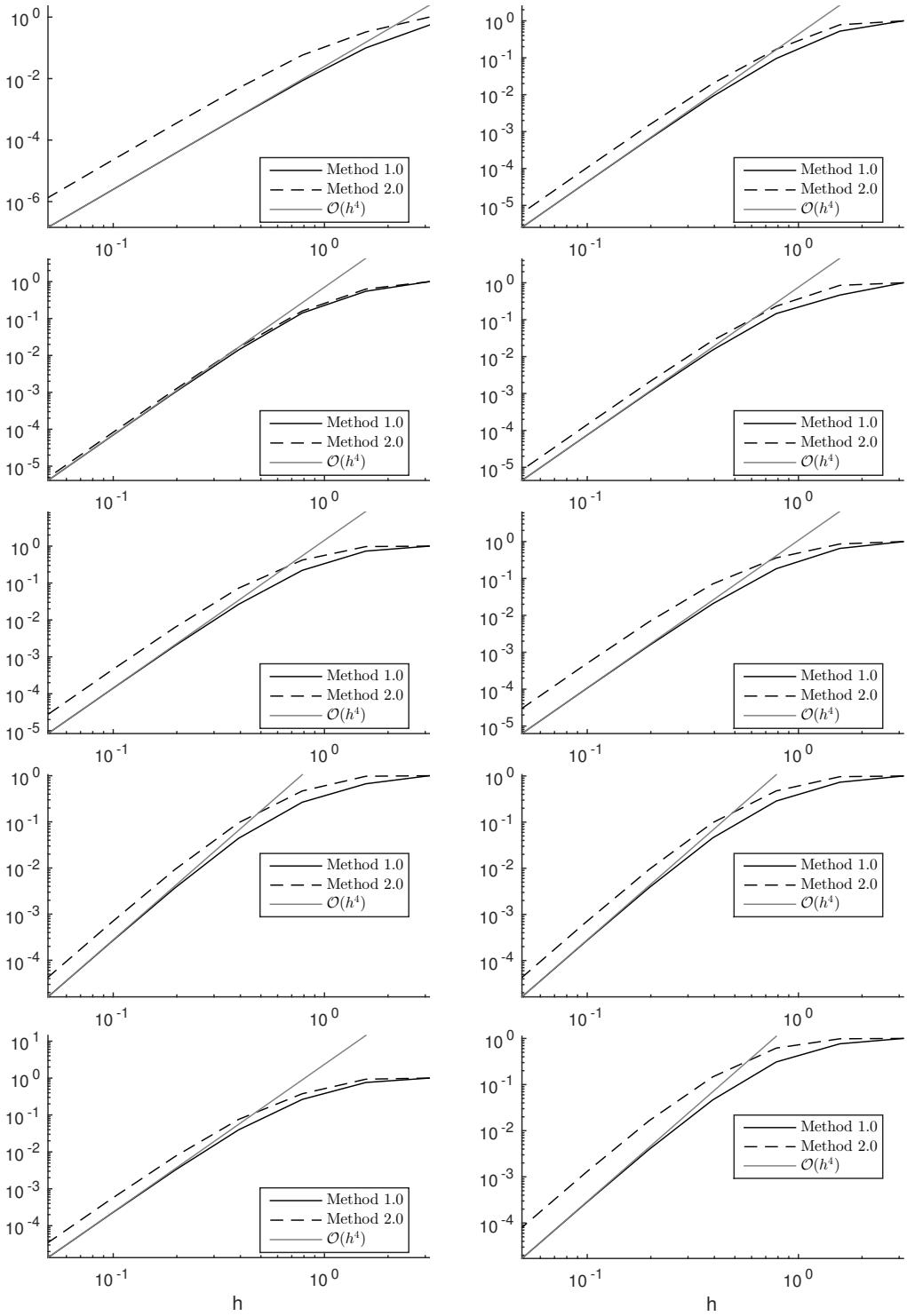


Figure 4.7: Relative $L^2$-error as given by (4.11) using fourth-order accurate approximation. From left to right, top to bottom: $\boldsymbol{\tau}_l$, for $l = 1, \ldots, 10$.

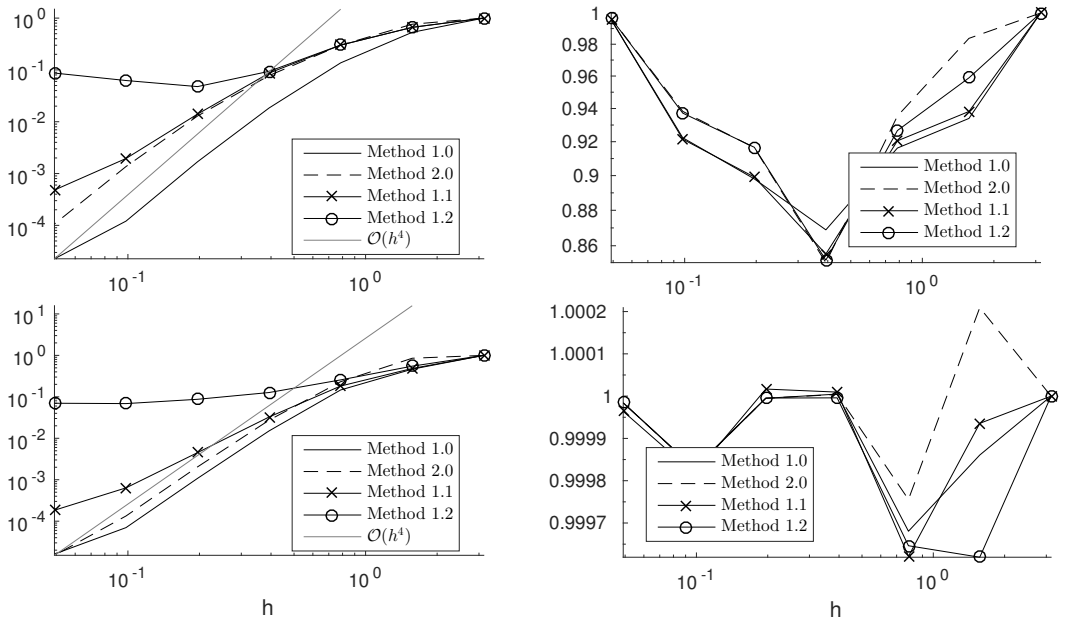


Figure 4.8: From left to right, top to bottom: $\tilde{\boldsymbol{\tau}}_l$, for $l = 2, \ldots, 5$.

The terms $\tilde{\boldsymbol{\tau}}_2$ and $\tilde{\boldsymbol{\tau}}_4$ clearly illustrate the differences in the four discretisation methods. Whereas the terms $\tilde{\boldsymbol{\tau}}_3$ and $\tilde{\boldsymbol{\tau}}_5$ seem to yield inaccurate results for *all* discretisation methods (note that similar results are obtained for second-order accuracy). We discuss (and solve) this problem in detail in Section 4.3.3, we first interpret the results corresponding to the other terms.

As expected, Method 1.0 yields the best results in terms of accuracy. Both Methods 1.0 and 2.0 are fourth-order accurate, albeit Method 2.0 needs more refinement before it is actually fourth-order accurate.

The term $\tilde{\boldsymbol{\tau}}_4$ requires some special attention. Recall from Section 3.3, where we showed the Gram matrix $\mathbf{G}$, that $\boldsymbol{\tau}_4$ is already orthogonal to $\boldsymbol{\tau}_0, \ldots, \boldsymbol{\tau}_3$. The local orthogonalisation used in both Methods 1.0 and 2.0 actually notices this, and hence attains the same accuracy as before, without orthogonalisation. However the averaging imposed in Method 1.1 and even worse in Method 1.2 results in a relatively large loss of accuracy, even though the orthogonalisation was not necessary (in terms of obtaining second- or fourth-order accuracy).

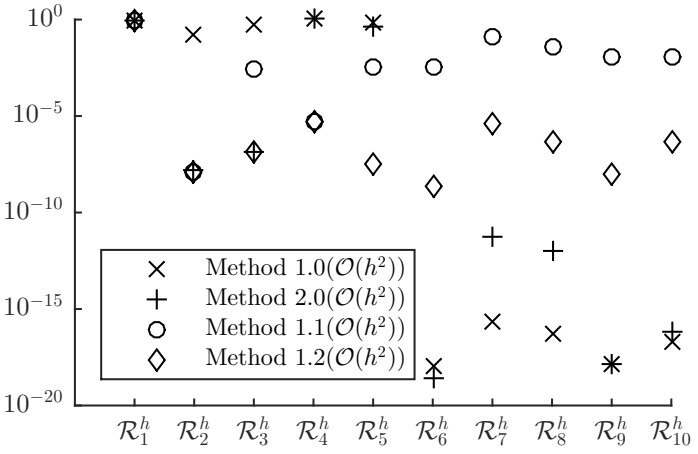


Figure 4.9: Ratio as given in (4.12) when using a HIT velocity field.

### 4.3.2 Numerical sub-grid dissipation

On the one hand, so far, we have demonstrated the accuracy properties of the four discretisation methods. However a second (and perhaps equally important) criterion for our discretisation is the preservation of the conservation law which states that the discrete sub-grid dissipation, $\epsilon_S^h$, vanishes whenever the coefficient $\alpha_1$ equals zero.

We test this using a homogeneous and isotropic initial velocity field. For this velocity field we then, for all four discretisation methods, calculate the sub-grid dissipation for all ten terms, both orthogonalised and not orthogonalised.

We quantify how small the sub-grid dissipation is by comparing $\epsilon_S^h(\boldsymbol{\tau}_l)$ to $\epsilon_S^h(\tilde{\boldsymbol{\tau}}_l)$, where for $l > 1$ we want the sub-grid dissipation to become significantly smaller after orthogonalisation. We define

$$\mathcal{R}_l^h := \left| \frac{\epsilon_S^h(\tilde{\boldsymbol{\tau}}_l)}{\epsilon_S^h(\boldsymbol{\tau}_l)} \right|, \quad \text{for } l = 2, \dots, 10 \tag{4.12}$$

as the ratio between the two. Let's consider a few special cases

- If $\tilde{\boldsymbol{\tau}}_l = 0$ (which is generally the case for $l = 6, \dots, 10$) the sub-grid dissipation should vanish. Hence in such a situation we want to have $\mathcal{R}_l^h = 0$.
- If a non-orthogonalised term $\boldsymbol{\tau}_l$ is already orthogonal to $\boldsymbol{\tau}_1$, the sub-grid dissipation should not change. More specifically
$$\mathcal{R}_l^h \approx 1, \quad \text{for } l = 4, 5.$$
- For the remaining terms ($l = 2, 3$) we would like to have
$$\mathcal{R}_l^h \ll 1.$$

In Figure 4.9 we show the results. Keeping in mind that, partially at least, we use orthogonalisation to be able to have control over the temporal evolution of the kinetic energy, we immediately see that Method 1.0 is not suitable.

Moreover due to the non-locality of the orthogonalisation used in Methods 1.1 and 1.2, we see that $\mathcal{R}_4^h \ll 1$, even though it should be of order one, as it is for Methods 1.0 and 2.0. For the same reasons

we also observe that Method 1.1 and especially Method 1.2 do not yield a proper sense of (local) orthogonality. Judging from Figure 4.9, $l > 5$, we would expect there to be 10 linearly independent tensors since $\mathcal{R}_l^h$ does not tend to zero for $l > 5$ when considering Methods 1.1 and 1.2.

### 4.3.3 Orthogonalisation

In our accuracy experiments we noticed a large relative error (of order one) for the terms $\tilde{\boldsymbol{\tau}}_3$ and $\tilde{\boldsymbol{\tau}}_5$ (see Figure 4.8). It's worth noting that these two terms cause a large relative error irrespective of which discretisation method was used.

To be able to study this analytically, we consider a simpler velocity field given by

$$\mathbf{w}_1(\mathbf{x}) = \begin{pmatrix} (y-\pi)^2 \\ (x-\pi)^2 \\ (z-\pi)^2 \end{pmatrix}, \quad \mathbf{x} \in \Omega = [0, 2\pi]^3.$$

From our experiments we note that the same issue arises when using this velocity field, as when using $\mathbf{w}_0$.

We consider the terms one by one. The velocity gradient is given by

$$\nabla \mathbf{w} = 2 \begin{bmatrix} 0 & y-\pi & 0 \\ x-\pi & 0 & 0 \\ 0 & 0 & z-\pi \end{bmatrix},$$

from which it follows that $\boldsymbol{\tau}_1, \boldsymbol{\tau}_2$ and $\boldsymbol{\tau}_3$ are given by

$$\boldsymbol{\tau}_1 = \begin{bmatrix} 0 & x+y-2\pi & 0 \\ x+y-2\pi & 0 & 0 \\ 0 & 0 & 2z-2\pi \end{bmatrix}, \quad \boldsymbol{\tau}_2 = \begin{bmatrix} (x+y-2\pi)^2 & 0 & 0 \\ 0 & (x+y-2\pi)^2 & 0 \\ 0 & 0 & (2z-2\pi)^2 \end{bmatrix},$$

$$\boldsymbol{\tau}_3 = \begin{bmatrix} (x-y)^2 & 0 & 0 \\ 0 & (x-y)^2 & 0 \\ 0 & 0 & 0 \end{bmatrix}.$$

It follows $\boldsymbol{\tau}_2$ and $\boldsymbol{\tau}_0$ are collinear on the plane described by $z = (x+y)/2$. Hence

$$\tilde{\boldsymbol{\tau}}_2 = \mathbf{0} \Leftrightarrow z = (x+y)/2.$$

Note that since the velocity gradient only has three linearly independent components, it follows that the set of symmetrised tensors can not have more than three linearly independent terms either. Hence

$$\boldsymbol{\tau}_3 = \mathbf{0} \Leftrightarrow z \neq (x+y)/2.$$

The orthogonalisation results in a discontinuous (w.r.t. the spatial coordinate $\mathbf{x}$) set of tensors. Note that since this discontinuity appears before the discrete divergence operator is applied, problems will arise after this differentiation operator is used. Example 4.2 illustrates this discontinuity more precisely.

**Example 4.2.** *Consider the orthogonalisation (without normalisation) of the columns of the following matrix* $\mathbf{V}(x)$

$$\mathbf{V}(x) = \begin{bmatrix} 1 & 1 & 0 \\ 0 & 1-x & 1 \\ 1 & 1 & 0 \end{bmatrix},$$

*here we do not allow the permutation of columns as we want to preserve the order globally. We want to preserve the order since in our model the numerical orthogonalisation is a local operation, whereas the ordering of the tensors (here the columns of* $\mathbf{V}(x)$*) should agree globally.*

*Denote by* $\tilde{\mathbf{V}}$ *the resulting orthogonalised columns. For* $x \neq 1$*, we get* $\tilde{\mathbf{V}}(x \neq 1)$*, given by*

$$\tilde{\mathbf{V}}(x \neq 1) = \begin{bmatrix} 1 & 0 & 0 \\ 0 & 1-x & 0 \\ 1 & 0 & 0 \end{bmatrix},$$

*whereas if* $x = 1$ *we get*

$$\tilde{\mathbf{V}}(x = 1) = \begin{bmatrix} 1 & 0 & 0 \\ 0 & 0 & 1 \\ 1 & 0 & 0 \end{bmatrix}.$$

*When computing the analytical expression* $\tilde{\mathbf{V}}(x)$ *using MATLAB's symbolic toolbox, we always end up with former expression, whereas the latter would be correct for* $x = 1$[§]*. The correct norm of* $\tilde{\mathbf{v}}_3(x)$ *is then given by*

$$|\tilde{\mathbf{v}}_3(x)| = \begin{cases} 0 & \text{if } x \neq 1 \\ 1 & \text{if } x = 1 \end{cases}.$$

*In this example,* $\mathbf{v}_1, \mathbf{v}_2$ *and* $\mathbf{v}_3$ *play the role of* $\boldsymbol{\tau}_0, \boldsymbol{\tau}_2$ *and* $\boldsymbol{\tau}_3$ *respectively.*

*If we replace the third column by*

$$\mathbf{v}_3 = \begin{bmatrix} 0 \\ 1-x \\ 0 \end{bmatrix},$$

*(hence scaling it with the norm of* $\tilde{\mathbf{v}}_2$*) we would get*

$$|\tilde{\mathbf{v}}_3(x)| = 0,$$

*for all* $x$*. This yields a set of columns which are continuous in* $x$*, but span a smaller space than the columns of the original* $\mathbf{V}$ *do.*

*Hence the relative scaling of the columns plays an important role in whether or not the orthogonalisation leads to discontinuities. However this replacement yields a rank one* $\tilde{\mathbf{V}}(x)$*, where the rank of* $\mathbf{V}(x)$ *is clearly two for all* $x$*.*

It follows that the large relative error is caused by the error in the simplification done in MATLAB rather than an error in our discretisation method. This does not mean however that we can now use this discretisation, since the discontinuous (let alone non-differentiable) behavior of $\tilde{\boldsymbol{\tau}}_3$ and $\tilde{\boldsymbol{\tau}}_5$ are undesirable and actually get worse upon mesh refinement. This is not caused by the discretisation but by the way the problem is posed.

Similar to the columns of $\mathbf{V}$, we note that the term $\boldsymbol{\tau}_3 = \boldsymbol{\Omega}^2$ is unrelated to $\boldsymbol{\tau}_1 = \mathbf{S}$ and $\boldsymbol{\tau}_2 = \mathbf{S}^2$ which is the cause of the problems we noted earlier. Hence we redefine our model terms in the following way

$$\begin{array}{lcllcl} \hat{\boldsymbol{\tau}}_0 & = & \boldsymbol{\tau}_0, & \hat{\boldsymbol{\tau}}_1 & = & \boldsymbol{\tau}_1 \perp \hat{\boldsymbol{\tau}}_0, \\ \hat{\boldsymbol{\tau}}_2 & = & \boldsymbol{\tau}_2 \perp \hat{\boldsymbol{\tau}}_0, \hat{\boldsymbol{\tau}}_1, & \hat{\boldsymbol{\tau}}_3 & = & |\hat{\boldsymbol{\tau}}_1| \boldsymbol{\tau}_3 \perp \hat{\boldsymbol{\tau}}_0, \hat{\boldsymbol{\tau}}_1, \\ \hat{\boldsymbol{\tau}}_4 & = & \boldsymbol{\tau}_4, & \hat{\boldsymbol{\tau}}_5 & = & |\boldsymbol{\tau}_4| \boldsymbol{\tau}_5 \perp \hat{\boldsymbol{\tau}}_4. \end{array} \tag{4.13}$$

With $\perp$ we denote the explicit orthogonalisation of the term on the left with the terms that follow on the right-hand side. Hence the Gram matrix corresponding to the new set of tensors is given by

$$\hat{\mathbf{G}} = \begin{bmatrix} \bullet & & & & \\ & \bullet & & & \\ & & \bullet & \bullet & \\ & & \bullet & \bullet & \\ & & & & \bullet \\ & & & & & \bullet \end{bmatrix}.$$

[§]This is because MATLAB's `simplify` does not check if a denominator equals zero and simplifies $(1-x)/(1-x)$ always to one.

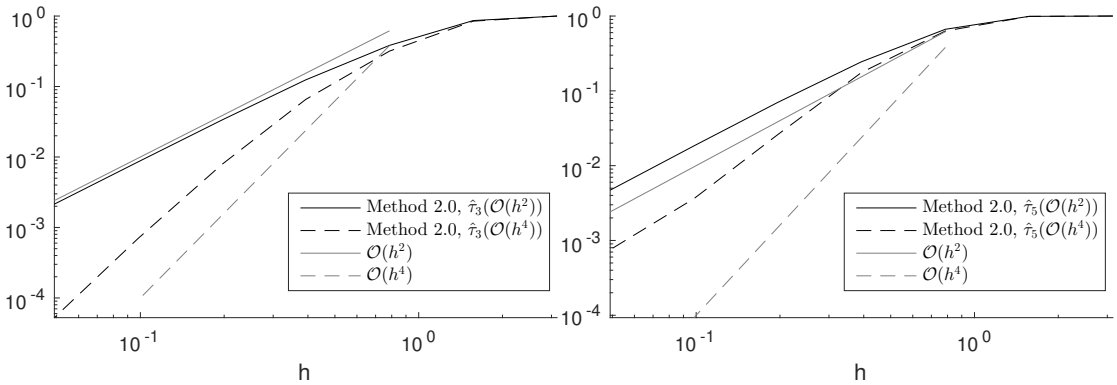


Figure 4.10: Relative error as given by (4.11) resulting from applying the new "basis" given by (4.13). Solid denotes the new basis, where dashed denotes the old.

whereas for the original set of orthogonalised tensors the Gram matrix was given by $\tilde{G}_{kl} = |\tilde{\boldsymbol{\tau}}_k|^2 \delta_{kl}$. Since $\boldsymbol{\tau}_4$ and $\boldsymbol{\tau}_5$ are already orthogonal w.r.t. $\boldsymbol{\tau}_0, \ldots, \boldsymbol{\tau}_3$, we do not modify $\boldsymbol{\tau}_4$ and only orthogonalise $\boldsymbol{\tau}_5$ w.r.t. $\boldsymbol{\tau}_4$. This yields a set of 6 tensors which are mutually orthogonal except for the pair $\hat{\boldsymbol{\tau}}_2, \hat{\boldsymbol{\tau}}_3$.

For the moment we leave out the terms $\boldsymbol{\tau}_6, \ldots, \boldsymbol{\tau}_{10}$, since in almost all cases the six terms given above are sufficient to span the space of symmetric $3 \times 3$ tensors. This choice of basis yields the following results when testing the accuracy, as shown in Figure 4.10. Note that from the results it follows that this alternative choice yields second- and fourth-order results, as expected.

### 4.3.4 Comparison and conclusion

Judging from the numerical validation, Method 2.0 appears to be the method of choice. It is second-order accurate, albeit with a slightly larger error constant than Method 1.0. The big advantage is that Method 2.0 has both a local sense of orthogonalisation as well as a vanishing numerical sub-grid dissipation whenever the model is non-dissipative.

The downside of Method 2.0, compared to Method 1.0, is that the tensors are interpolated twice. This yields a rather large stencil. For example, $((\boldsymbol{\tau}_1)_{12})^h_{i,j}$ depends on nine values of $(S_{12})^h$, *after* which we extrapolate to obtain fourth-order accuracy.

*Improving Method 2.0*

When solving the model problem, using only $\boldsymbol{\tau}_1$, the previously mentioned large stencil results in an energy spectrum (at the end of the simulation) as shown in Figure 4.11. The two peaks at the end of the spectrum correspond to the wavenumbers $k = 32$ and $k = 32\sqrt{2}$. These wavenumbers correspond exactly to the univariate and bivariate waves which are not noticed when averaging twice as we do in Method 2.0.

In particular a univariate wave given by

$$u = \sin(32y + \pi/4)$$

is not noticed, whereas

$$u = \sin(32x + \pi/4)$$

*is* noticed. This is due to the fact that the diagonal elements of $(\boldsymbol{\tau}_1)^h$ are not averaged at all. Similar situations arise when considering bivariate waves, e.g.

$$u = \sin(32(y + z))$$

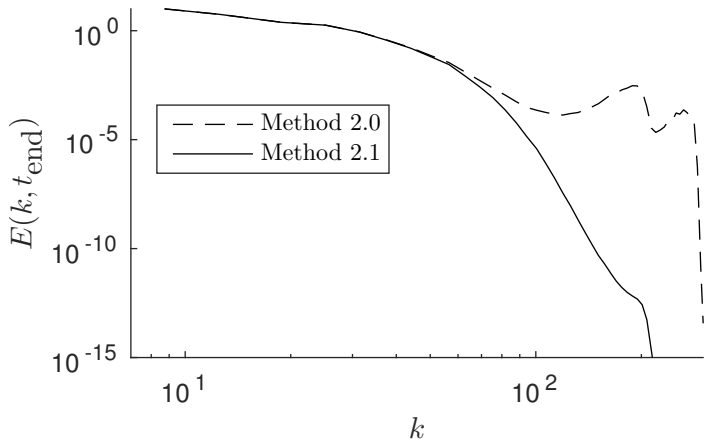


Figure 4.11: Resulting energy spectra at the end of a simulation using $\boldsymbol{\tau} = -C\boldsymbol{\tau}_1$.

is not noticed by $(\boldsymbol{\tau}_1)^h$, which corresponds to the wavenumber $k = |\mathbf{k}| = \sqrt{32^2 + 32^2}$. Therefore dissipation, as caused by $\boldsymbol{\tau}_1$, is not active on the wavenumbers $k = 32$ and $k = 32\sqrt{2}$ which correspond to the peeks observed in Figure 4.11.

Especially for this linear term, $\boldsymbol{\tau}_1$, this problem arises since there is no interaction between the wavenumbers (wave vectors). We can easily circumvent this problem though, since instead of using $(\boldsymbol{\tau}_1)^h$ (averaged twice) we can use the staggered $\mathbf{S}$ which we started with. Only the computation of any coefficient $\alpha_1(\mathbf{x}, t)$ needs to be adjusted for this term.

The resulting method will be denoted by "Method 2.1". We emphasise that all the other terms are not changed by this alteration; we still compute the averaged $(\boldsymbol{\tau}_1)^h$ for the construction of $(\hat{\boldsymbol{\tau}}_l)^h$, $l > 1$. Using Method 2.1 in the same model problem results in the energy spectrum as shown in Figure 4.11.

## 4.4 Temporal discretisation

The previously discussed spatial discretisation yields the following system of ODEs

$$\boldsymbol{\Omega}\frac{d\mathbf{u}^h}{dt} = -\mathbf{T}(\mathbf{u}^h), \tag{4.14}$$

where, provided $\alpha_1 = 0$, $\mathbf{T}$ satisfies

$$\left\langle \mathbf{u}^h, \mathbf{T}(\mathbf{u}^h) \right\rangle = 0. \tag{4.15}$$

When simulating (4.14) (hence not solving the complete MNSE), we want the temporal discretisation (in some approximate sense) to also conserve kinetic energy whenever $\alpha_1 = 0$. Moreover if we solve the full MNSE we need a time stepping procedure which has a linear absolute stability region which contains a sufficiently large part of the left-hand side of the complex plane since the eigenvalues of the Laplace operator are located there.

A candidate *explicit* time stepping procedure is given by the following parameter dependent, explicit one-leg scheme which was also used in Verstappen and Veldman (2003) (consider $\frac{du}{dt} = f(u)$)

$$(\beta + \frac{1}{2})u^{(n+1)} - 2\beta u^{(n)} + (\beta - \frac{1}{2})u^{(n-1)} = \delta t f((1+\beta)u^{(n)} - \beta u^{(n-1)}). \tag{4.16}$$

Depending on the value of $\beta$ we obtain different time stepping schemes (of possibly different order: two or three) which all have different linear absolute stability regions as well as conservation properties w.r.t. the kinetic energy.

*The case when* $\beta = 0$

If $\beta = 0$ we obtain the second-order Leap-Frog method

$$u^{(n+1)} = u^{(n-1)} + 2\delta t f(u^{(n)}).$$

This yields (when considering (4.14))

$$\left(\mathbf{u}^{(n)}, \mathbf{u}^{(n+1)}\right) = \left(\mathbf{u}^{(n)}, \mathbf{u}^{(n-1)} + 2\delta t \mathbf{T}(\mathbf{u}^{(n)}\right) = \left(\mathbf{u}^{(n)}, \mathbf{u}^{(n-1)}\right).$$

It follows that

$$\left(\mathbf{u}^{(n+1)}, \mathbf{u}^{(n)}\right) = C \tag{4.17}$$

for some constant $C$. Note that this is not as good as the desired conservation property

$$\|\mathbf{u}^{(n)}\|_2 = C.$$

The linear absolute stability region is given by (when considering $\frac{du}{dt} = \lambda u$)

$$\lambda = i\omega, \quad \omega \in \mathbb{R}, \quad \delta t \omega \leq 1.$$

It follows that the eigenvalues of the Jacobian of the operator are required to be purely imaginary for this method to be linearly absolutely stable.

Unfortunately, for our general tensor model the Jacobian is *not* skew-symmetric since from (4.15) it merely follows that

$$\mathbf{J}(\mathbf{u}^h)^T \mathbf{u}^h = -\mathbf{T}(\mathbf{u}^h),$$

which, if $\mathbf{T}$ is linear, implies that $\mathbf{J}(\mathbf{u}^h)$ is skew-symmetric. Since the linearisation is not energy conserving, linear stability analysis is simply not sufficient to be able to determine whether the temporal discretisation yields a stable simulation (in terms of a restriction on the step size $\delta t$).

*The case when* $\beta \neq 0$

Whenever $\beta \neq 0$ we find that (4.17) no longer holds. From studying the stability regions for different values of $\beta$, see Figure (4.12), we find that for larger values of $\beta$ the stability region moves away from the imaginary axis.

By choosing $\beta > 0$ we introduce some sense of stability in our simulation in the form of numerical damping (note that the amplification factor for $\beta = 0$ is equal to one in the stable region).

*Conclusion*

Unfortunately we can not make precise statements about the stability of the time-stepping procedure because this would require a nonlinear stability analysis. However, when simulating the full MNSE the introduction of the dissipative term means that we can not let $\beta = 0$. So whether or not $\beta = 0$ is numerically stable is irrelevant when considering realistic simulations.

We did however notice that the simulations using $\beta = 0$ were stable up to some point, and the kinetic energy was conserved quite well. We show this in Figure 4.13 where we performed a simulation using $\boldsymbol{\tau} = \boldsymbol{\tau}_4$. The observed oscillations are due to the time stepping procedure. When using Method 1.0 the kinetic energy increases over time until the simulation "blows up". This simple experiment shows the usefulness of preferring the preservation of energy conservation properties over minimising the truncation error.

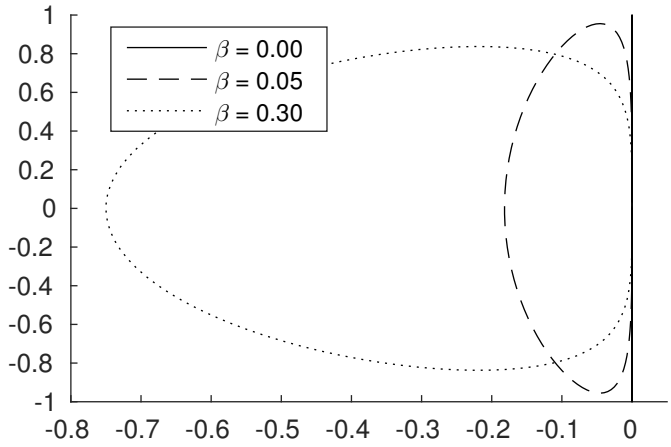


Figure 4.12: Regions of absolute stability for the time stepping procedure given by (4.16) for different values of $\beta$.

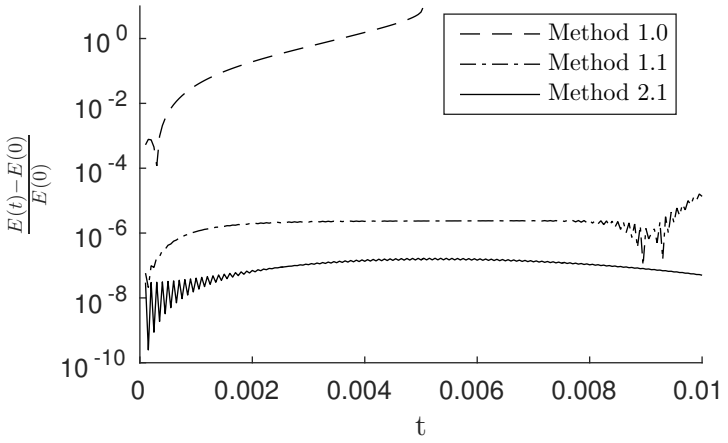


Figure 4.13: Simulation of $\partial_t \mathbf{u} = -\nabla \cdot \boldsymbol{\tau}_4$. Relative error in the conservation of the kinetic energy. Here we used $\beta = 0$, the step size is given by $\delta t = 10^{-5}$.

# Chapter 5

# Analysis of the general framework of LES models

The aim of this chapter is to characterise the members of the general framework of LES models as introduced in Section 3.3. As a starting point in this analysis we consider a single non-dissipative (transport) term. As introduced in Section 5.1 we consider the simulation of merely the LES model (hence also not imposing conservation of mass, see (5.1)), therefore separating the effect the LES model has from the other terms of the MNSE, e.g. convection and dissipation. We will call this the model problem.

In Section 5.2 we consider the influence of switching the time direction in the simulation of the aforementioned model problem. When considering the temporal evolution of the energy spectrum function we observe there to be no significant difference when going either forward or backward in time. We analyse this also analytically by considering the one-dimensional Burger's equation.

Section 5.3 covers the comparison of the transport term with the convective term. We choose this approach since we are interested in using a transport mechanism as being part of a LES model, therefore not only modelling the dissipative part of the exact sub-filter scale tensor. In this section we therefore quantify the transport mechanism in terms of the way it distributes the kinetic energy over the different scales of motion by comparing it to the convective term.

An a priori analysis of the transport term is done in Section 5.4. Here we consider whether the transport term is in some way an approximation to the exact sub-filter scale tensor.

Finally, in Section 5.5, we consider the application to LES. Using the results of the characterisation obtained in Section 5.3 we propose a two-parameter LES model where we model the transport part using the aforementioned transport term. Using the HIT test case we perform numerous simulations, where we perform the assessment of the LES model using experimental data from the CBC experiment (Comte-Bellot and Corrsin, 1971).

## 5.1 The model problem

In the general framework of LES models we have proposed the orthogonalisation of the terms to generalise the separation of dissipative and non-dissipative (transport) terms. We start off the characterisation of each of these terms by considering only one such transport term: $\hat{\boldsymbol{\tau}}_4$. We choose this term because it actually equals the non-orthogonalised term $\boldsymbol{\tau}_4$ therefore it does not require explicit orthogonalisation, hence making it an appealing term numerically.

To separate the influence of the already present convective and dissipative term in the MNSE, we

initially consider the simulation of the following model problem

$$\partial_t \mathbf{w} = -\nabla \cdot \boldsymbol{\tau}, \quad \mathbf{w}(0) = \mathbf{w}_0^{\text{HIT}}, \quad t \in [0, t_{\text{end}}]. \tag{5.1}$$

where we consider $\boldsymbol{\tau}$ to be a transport term, in particular we are interested in

$$\boldsymbol{\tau} = \alpha_4(\mathbf{x}, t)\boldsymbol{\tau}_4.$$

Such a model problem represents a conservation law. Momentum as well as kinetic energy are conserved (provided the boundary conditions are for example periodic). Since we consider a homogeneous (and isotropic) velocity field, but also for simplicity, we may consider $\alpha_4(\mathbf{x}, t)$ to be a constant

$$\alpha_4(\mathbf{x}, t) = C_4.$$

This simplification greatly simplifies the characterisation we want to perform. In the next section we consider the influence of changing the sign of $C_4$, which is actually equivalent to changing the temporal direction. Moreover, in Section 5.3 we study the influence of the magnitude of $C_4$, which is equivalent to changing the time scale.

## 5.2 Temporal direction

The starting point of our analysis is to determine what role the sign of the coefficient $C_4$ plays. As mentioned before, switching the sign of $C_4$ is equivalent to switching the temporal direction. Therefore we first consider two simulations of the model problem (5.1) where we consider both temporal directions. The second part of this section discusses what happens to the equations under a change of time direction.

### 5.2.1 Experimental observation

We perform two simulations of (5.1), where we keep the magnitude of $C_4$ equal but switch the sign. We choose $C_4$ initially such that at $t = t_{\text{end}}$ the end of the energy spectrum has somewhat converged. This yields $C_4 = 4 \cdot 10^{-2}$. The resulting temporal evolution of the energy spectra is shown in Figure 5.1.

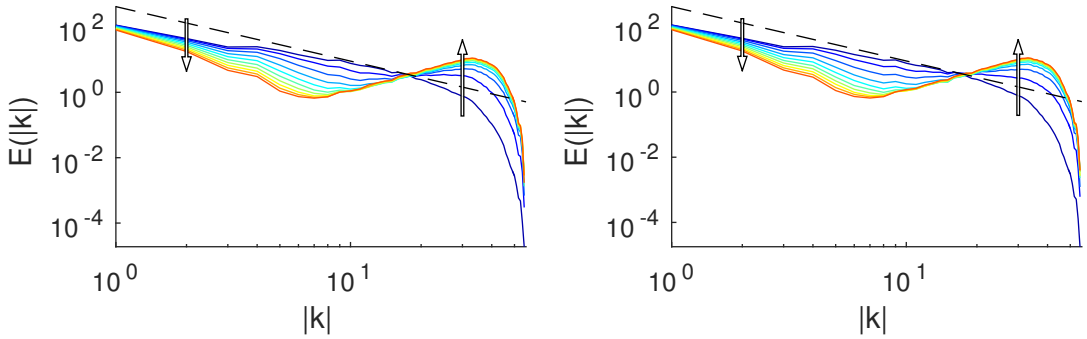


Figure 5.1: Temporal evolution of the energy spectrum when simulating the model problem (5.1) using $\boldsymbol{\tau}_4 = C_4\boldsymbol{\tau}_4$. Left: $C_4 = -4 \cdot 10^{-2}$. Right: $C_4 = 4 \cdot 10^{-2}$.

We observe that the sign of the coefficient (or equivalently the temporal direction) does not yield any noticeable difference when considering the energy spectrum.

It is to be noted that a similar result is found when simulating the convective term, where we also find that changing the temporal direction does not yield a different energy spectrum.

### 5.2.2 Analysis

*In the Fourier domain*

To simplify the analysis we consider a one-dimensional analogue to the model problem (5.1), where we consider using the convective term

$$\boldsymbol{\tau} = \mathbf{w} \otimes \mathbf{w}.$$

Such a one-dimensional analogue is given by the inviscid Burgers' equation

$$\begin{cases} \partial_t w &= -\partial_x(w^2), \quad x \in \Omega = [0, 2\pi], \quad t \in [-T, T] \\ w(x,t) &= w(x + 2\pi, t). \end{cases} \tag{5.2}$$

Similar to our model problem we consider periodic boundary conditions. Since the invariance of the time direction is observed in the Fourier spectrum, we consider the Burgers' equation in the Fourier domain.

Since the Fourier basis functions form an orthonormal basis for $L^2([0, 2\pi])$, we consider the Fourier series expansion of $w(x, t)$, given by

$$w(x,t) = \sum_{l=-N}^{N} \alpha_l(t) e^{ilx}.$$

After substituting this expression in (5.2) we impose a Galerkin condition. This results in the following system of ODEs

$$\frac{d\alpha_l}{dt} = -il(\boldsymbol{\alpha} * \boldsymbol{\alpha})_l, \tag{5.3}$$

where $(\boldsymbol{\alpha} * \boldsymbol{\alpha})_l$ denotes the discrete convolution given by

$$(\boldsymbol{\alpha} * \boldsymbol{\alpha})_l = \sum_{j+k=l} \alpha_j \alpha_k.$$

Since complex conjugation commutes with multiplication, it follows that the complex conjugate of the coefficients satisfies the same equation (5.3) *up to a sign.* We formalise and generalise this idea in the following Theorem.

**Theorem 5.1.** *Consider the system of ODEs given by*

$$\frac{d\boldsymbol{\alpha}}{dt} = i\mathbf{F}(\boldsymbol{\alpha}), \quad t \in \mathbb{R} \tag{5.4}$$

*with* $\mathbf{F} : \mathbb{C}^N \to \mathbb{C}^N$ *such that*

$$\mathbf{F}(\widetilde{\boldsymbol{\alpha}}) = \widetilde{\mathbf{F}(\boldsymbol{\alpha})}, \tag{5.5}$$

*where a tilde denotes reflection about either the real or imaginary axis (component-wise). If the initial condition at* $t = t_0$ *satisfies*

$$\boldsymbol{\alpha}_0 = \widetilde{\boldsymbol{\alpha}}_0 \tag{5.6}$$

*then*

$$\boldsymbol{\alpha}(t_0 + t) = \widetilde{\boldsymbol{\alpha}(t_0 - t)}.$$

*Proof.* Consider

$$\frac{d\boldsymbol{\alpha}}{dt} = is\mathbf{F}(\boldsymbol{\alpha}), \quad s \in \{-1, +1\}, \tag{5.7}$$

and let $\boldsymbol{\alpha}^{\pm}(t)$ be the solution to (5.7) with

$$\boldsymbol{\alpha}^{\pm}(t_0) = \boldsymbol{\alpha}_0, \quad s = \pm 1.$$

Note that if $\boldsymbol{\alpha}$ satisfies (5.7), then $\widetilde{\boldsymbol{\alpha}}$ satisfies

$$\frac{d\widetilde{\boldsymbol{\alpha}}}{dt} = -is\mathbf{F}(\widetilde{\boldsymbol{\alpha}}).$$

Hence $\widetilde{\boldsymbol{\alpha}^{+}}$ satisfies (5.7) with

$$\widetilde{\boldsymbol{\alpha}^{+}(t_0)} = \widetilde{\boldsymbol{\alpha}_0}, \quad s = -1.$$

So if $\boldsymbol{\alpha}_0 = \widetilde{\boldsymbol{\alpha}}_0$ then

$$\boldsymbol{\alpha}^{-}(t) = \widetilde{\boldsymbol{\alpha}^{+}(t)}.$$

Note that $s$ merely represents the time direction, hence yielding the desired result. □

This means that for a very general class of PDEs defined on a periodic spatial domain the magnitude of the Fourier coefficients of the solution do not depend on the temporal direction, given that the Fourier coefficients of the initial solution satisfy some reflection invariance condition. Stated differently: a spatial symmetry (Fourier coefficients are invariant under reflection) results in a temporal symmetry.

For the Burgers' equation this results in the following Corollary.

**Corollary 5.1.** *Let $w(x,t)$ be a solution to* (5.2)*. If the initial condition $w(x,t_0)$ is even about some point $x \in [0, 2\pi)$, then*

$$|\alpha_l(t_0 + t)| = |\alpha_l(t_0 - t)|, \quad t \in [0, T],$$

*where $\alpha_l$ denotes the $l$-th Fourier component of $w$.*

*Proof.* Let $\mathbf{F}(\boldsymbol{\alpha}) : \mathbb{C}^{2N+1} \to \mathbb{C}^{2N+1}$ be defined by

$$F(\boldsymbol{\alpha})_l = -l(\boldsymbol{\alpha} * \boldsymbol{\alpha})_l,$$

then the Fourier components $\alpha_l$ satisfy the system of ODEs given by (5.4). Note that indeed the condition (5.5) is satisfied by $\mathbf{F}$, when considering reflection about the real axis.

Let $w(x,t_0)$ be even (the initial condition may be even about any $x \in [0, 2\pi)$, but due to the periodicity of the solution we may impose a change of coordinates such that it is even about $x = 0$)

$$w(x,t_0) = w(-x,t_0),$$

it follows that the Fourier components are real and hence (5.6) is satisfied as well. From Theorem 5.1 it follows that

$$\boldsymbol{\alpha}(t_0 + t) = \overline{\boldsymbol{\alpha}(t_0 - t)}.$$

□

In the Fourier domain the model problem is given by

$$\frac{d\mathcal{F}\{w_n\}(\mathbf{k})}{dt} = -ik_m \mathcal{F}\{\tau_{mn}\}(\mathbf{k}),$$

where $\mathcal{F}\{\tau_{mn}\}(\mathbf{k})$ denotes the Fourier transform of the components of $\boldsymbol{\tau}$. It follows that whenever $\boldsymbol{\tau}$ is given by some function of $\mathbf{w}$, which involves even products of derivatives of components of $\mathbf{w}$ (so the Fourier transform does not introduce additional purely imaginary factors), then indeed using Fourier

basis functions the model problem can be transformed into a system of ODEs of the form (5.7) where $\mathbf{F}$ satisfies (5.5) for complex conjugation. Since $\boldsymbol{\tau}_4$ is given by

$$\boldsymbol{\tau}_4 = \mathbf{S\Omega} - \mathbf{\Omega S},$$

it follows that this term satisfies this property.

Note however that the conditions of Theorem 5.1 are sufficient, but not necessary for an energy spectrum function to be invariant under changing the temporal direction. The observations made in the energy spectrum are based on a quantity derived from $\boldsymbol{\alpha}$ (the energy spectrum function is obtained by integrating over a shell of wave vectors with constant magnitude) and hence there are many other cases for which the energy spectrum function is invariant under a change in temporal direction.

Without considering what those necessary conditions are, we can conclude that under some conditions on the initial condition, the temporal direction indeed does not influence the energy spectrum, which explains our observation.

*In the spatial domain*

It is worth mentioning that from the structure of the Burgers' equation similar observations could be made. A coordinate transformation

$$(t, x) \to (t, -x), \tag{5.8}$$

results in the same equation as the coordinate transformation

$$(t, x) \to (-t, x), \tag{5.9}$$

does. Even though this observation can be made, considering the equations in the Fourier domain yields more explicit results in the sense that we can actually give sufficient conditions under which the magnitude of the Fourier components is invariant under the temporal direction.

Such observations however are easier to make in the spatial domain. Hence also for the model problem, equipped with merely the convection operator

$$\partial_t \mathbf{w} = -\nabla \cdot (\mathbf{w} \otimes \mathbf{w}),$$

or the model problem where we consider $\boldsymbol{\tau} = \boldsymbol{\tau}_4$

$$\partial_t \mathbf{w} = -\nabla \cdot \boldsymbol{\tau}_4,$$

it follows that transformations (5.8) and (5.9) applied to (5.1) yield equivalent equations. Therefore indicating that the resulting solution is invariant under a change of time direction, provided that the initial condition is even about some point.

## 5.3 Comparison with convection

Since we now have some idea on how to interpret the sign of the coefficient, the next freedom to consider is the magnitude of $C$, or equivalently the time scale. We perform two simulations of the model problem, again using an initial HIT velocity field. In the first simulation we consider the convective term, that is we solve

$$\partial_t \mathbf{w} = -\nabla \cdot (\mathbf{w} \otimes \mathbf{w}), \quad \mathbf{w}(0) = \mathbf{w}_0^{\text{HIT}}, \quad t \in [0, t_{\text{end}}].$$

We take $t_{\text{end}} = 4.5$ since at this point in time the end of the energy spectrum has somewhat converged to a steady state, but also because the simulation soon becomes unstable (we use $\beta = 0$, see Section 4.4). The second simulation concerns the model term $\boldsymbol{\tau} = C_4 \boldsymbol{\tau}_4$, as we did before.

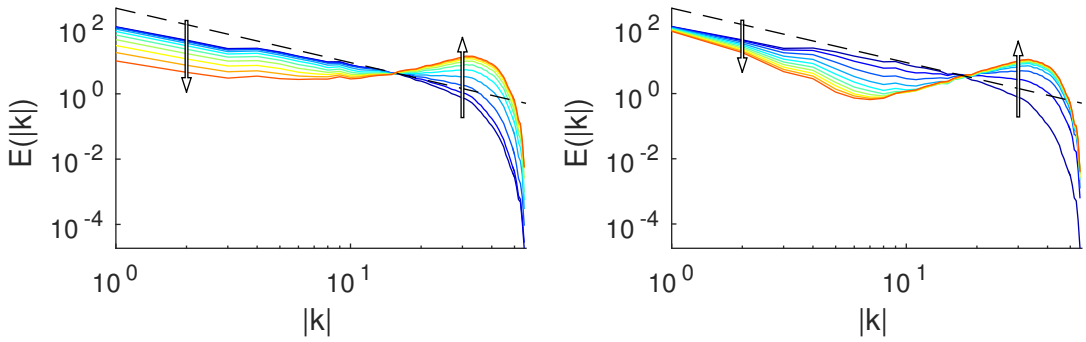


Figure 5.2: Temporal evolution of the energy spectrum. Left: convective term. Right: $\boldsymbol{\tau} = C_4\boldsymbol{\tau}_4$, where $C = 4 \cdot 10^{-2}$.

The two simulations result in the temporal evolution of the energy spectra as shown in Figure 5.2.

We observe a strong similarity (definitely as $t$ gets larger) at the end of the two spectra. At the large scales however, the convective term seems to have more effect. We now deal with quantifying the similarity at the end of the spectrum.

### 5.3.1 Correlation at the end of the energy spectrum

For studying the correlation at the end of the energy spectrum, we must define some correlation function $r(f(k), g(k))$, which yields a correlation value in the range $[0, 1]$ indicating whether the two functions $f(k)$ and $g(k)$ are correlated.

Given such a correlation function, we can then consider comparing the energy spectra of the two simulations at any two time-instances. That is we let

$$r_{mn} := r\left(E^{\text{Conv}}(k, t^{(m)}), E^{\boldsymbol{\tau}_4}(k, t^{(n)})\right)$$

be the correlation coefficient corresponding to the energy spectrum when simulating the convective term up to time $t = t^{(m)}$, compared to the energy spectrum when simulating $\boldsymbol{\tau}_4$ up to time $t = t^{(n)}$. Considering such a correlation surface, we will be able to determine a time scale for which the convective term and $\boldsymbol{\tau}_4$ are correlated the most at the end of the spectrum.

*Choosing a correlation function*

We must first choose a good correlation function. A good correlation function should differentiate between two qualitatively different energy spectra. A case in point being an energy spectrum resulting from a purely dissipative process compared to an energy spectrum resulting from the simulation of a transport term. Comparison of these two spectra should not yield a good correlation. Note that this is merely a test case and not a defining property of the correlation function.

The Pearson Correlation Coefficient (PCC) is given by

$$r^{\text{PCC}}(f(k), g(k)) := \frac{\langle f(k), g(k)\rangle}{\|f(k)\|\|g(k)\|}, \tag{5.10}$$

which is a measure for the linear correlation between the two functions $f(k)$ and $g(k)$. As mentioned previously, a method of validation of a correlation function is to consider how badly correlated the convective and dissipative term are. The correlation isolines resulting from using the PCC are shown

in Figure 5.3 (left). From our test it follows that, according to this correlation function, there is some time scale for which the correlation is larger than $90\%$ at the end of the spectrum. It follows that this correlation function is not suited for comparing energy spectra, hence we consider an alternative.

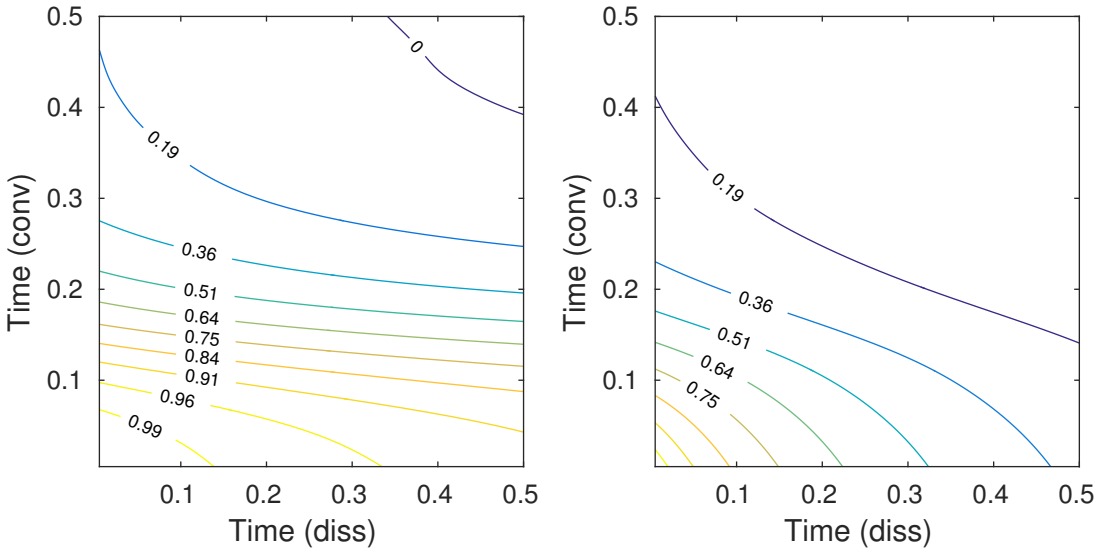


Figure 5.3: Resulting correlation isolines when comparing the end of the energy spectra from simulating the convective term, and the dissipative term. Left: PCC (5.10). Right: alternative (5.11).

The relative error between the two datasets could be used as a correlation function. However since we want to differentiate based on qualitative differences between two spectra, we may choose to ignore the energy content of a given spectrum (we consider the temporal evolution of the energy contents separately in a later section). This is done by considering the deviation of the energy spectrum from its mean value $\bar{f}(k)$.

We propose then, instead of using the PCC, to use the relative error between the two energy spectra, after subtracting the mean, as a correlation function.

Since a correlation function should yield a value of one whenever two datasets are correlated and zero when they are not, we consider one minus the previously mentioned relative error as our correlation function, this yields

$$0 \leq r(f(k), g(k)) := 1 - \frac{\|f(k) - g(k) - (\bar{f}(k) - \bar{g}(k))\|_2}{\|f(k) - \bar{f}(k)\|_2 + \|g(k) - \bar{g}(k)\|_2} \leq 1. \tag{5.11}$$

The range of $r$ equals the interval $[0, 1]$, as follows from application of the triangle inequality.

Applying this correlation function to our test case results in Figure 5.3 (right). As desired, this correlation function results in a decreasing correlation at any time scale (that is, along any straight line originating from the origin).

A final consideration would be to apply the correlation in loglog-space. That is, since we usually visually study a spectrum in a loglog-plot, we might consider the following correlation function as opposed to (5.11)

$$r^{\log}(f(k), g(k)) := r(f^{\log}(\tilde{k}), g^{\log}(\tilde{k})), \tag{5.12}$$

where $f^{\log}(\tilde{k})$ is defined as

$$f^{\log}(\tilde{k}) := \log_{10}(f(10^{\tilde{k}})).$$

For our test case (as well as for the upcoming results), this choice yields qualitatively similar results. See Figure 5.4. Our preference goes to the correlation function given by (5.11), mostly because this

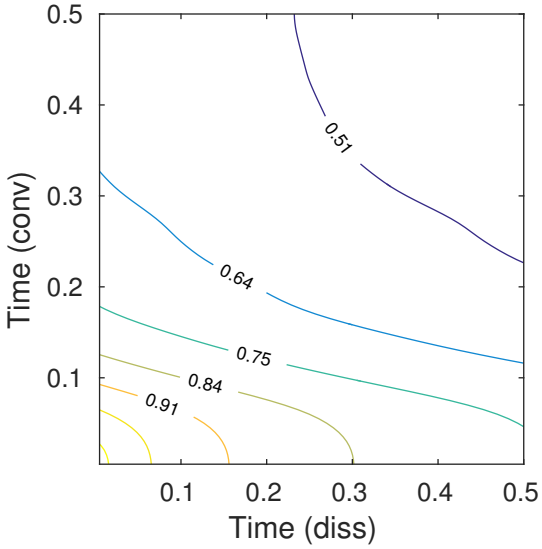


Figure 5.4: Resulting correlation isolines when comparing the end of the energy spectra from simulating the convective term, and the dissipative term. The correlation function is defined by (5.12)

yielded good results in the convection/dissipation test. But also because in loglog space the $L^2$-norm of a spectrum function $E(k,t)$ does not represent a physical quantity like kinetic energy.

*Results*

Using this correlation function we can now quantify the comparison between the two energy spectra shown in Figure 5.2. The observed similarity is at the end of the wavenumber range. Hence we fix some wavenumber $k^*$, and consider the correlation of the two energy spectra only for $k > k^*$. Since the energy spectra from both the simulation of the convective term as well as the simulation using $\boldsymbol{\tau}_4$ remains constant around $k = 18$, we choose this to be our value of $k^*$.

In Figure 5.5 we show the resulting correlation coefficient isolines. Moreover we plot the straight line (hence choosing a time scale or equivalently a coefficient $C$) originating from the origin for which the minimum correlation along this line is maximised. The figure on the right shows the correlation along this line.

Moreover, in Figure 5.6 we show the correlation at the beginning of the spectrum (for $k < k^*$). Note that also in this comparison we could choose a time scale for which the correlation is high.

We conclude that both at the beginning and end of the spectrum the two terms show similarity, albeit not simultaneously at a single time scale.

### 5.3.2 Presence of an inertial subrange

We have now made a qualitative comparison between the simulation of the convective term and that of the model term $\boldsymbol{\tau}_4$. We could also consider a quantitative comparison in terms how the model terms divides the energy among different scales of motion.

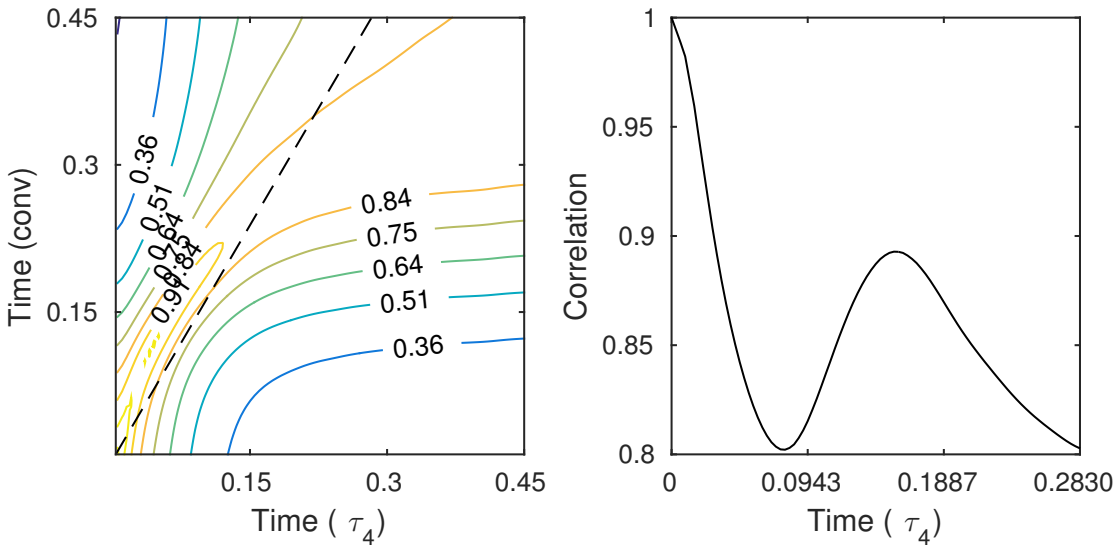


Figure 5.5: Left: Correlation coefficient isolines. Comparing the end ($k > k^*$) of the energy spectra resulting from simulating the convective term, and the model term $\boldsymbol{\tau}_4$. The dashed line equals $t^{\text{Conv}} = 1.59t^{\boldsymbol{\tau}_4}$. Right: The correlation coefficient along the dashed line.

When studying the temporal evolution of the energy spectrum of a full NS simulation, we often consider the full wavenumber range to consist of three qualitatively different subintervals. This was mentioned before in Section 2.3 where we briefly discussed Kolmogorov's theory of turbulence.

Similarly, when simulating merely a transport term, we can define a wavenumber range where the energy content remains constant, the inertial range. We define the energy content as

$$E_I(t) := \fint_I E(k,t)dk, \quad I \subset [0, k_{\text{max}}],$$

where

$$\fint_\Omega f(x)dx := \frac{1}{|\Omega|}\int_\Omega f(x)dx,$$

denotes the average of $f$ over the set $\Omega$. Defining such an inertial range, being a subinterval of the total wavenumber range, yields three different wavenumber subintervals.

The largest wavenumber $k_{\text{max}}$ noticed by our model in a 3D simulation using a uniform mesh with 64 subintervals in each direction (rounded to the nearest integer) is given by

$$\lfloor k_{\text{max}} \rceil = \left\lfloor \sqrt{32^2 + 32^2 + 32^2} \right\rceil = \left\lfloor 32\sqrt{3} \right\rceil = 55.$$

The corresponding wave vector, $[32, 32, 32]^T$, represents a fully diagonal wave spanning 8 volumes. It follows that the interval $I$ is a subinterval of the total wavenumber range given by $I_k := [0, 55]$.

Both for the convective term and the model term $\boldsymbol{\tau}_4$ we experimentally determine the wavenumber subinterval for which the energy content remains constant. We find the following inertial subranges

$$I_{\text{I}}^{\text{Conv}} = [4, 31], \quad I_{\text{I}}^{\boldsymbol{\tau}_4} = [7, 33].$$

The definition of the inertial subrange also yields two other wavenumber subintervals: the large scales of motion denoted by $I_{\text{L}}$ containing all wavenumbers smaller than those in the inertial range, and the

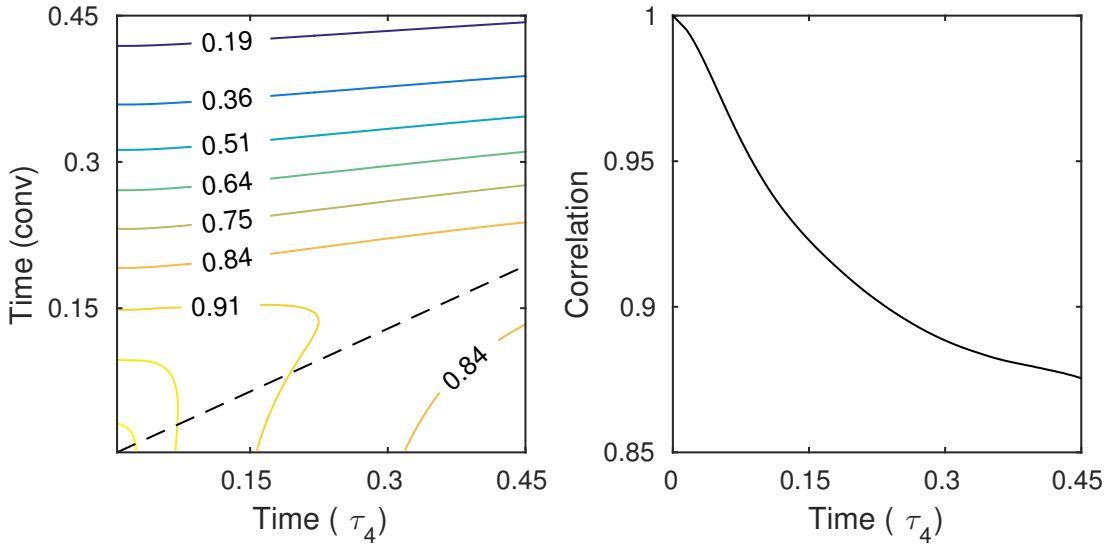


Figure 5.6: Left: Correlation coefficient isolines. Comparing the beginning ($k < k^*$) of the energy spectra resulting from simulating the convective term, and the model term $\boldsymbol{\tau}_4$. The dashed line equals $t^{\text{Conv}} = 0.43 t^{\boldsymbol{\tau}_4}$. Right: The correlation coefficient along the dashed line.

small scales of motion denoted by $I_S$ containing the wavenumbers larger than those in the inertial range. This results in Figure 5.7 where we compare the energy contents. We use

$$C_4 = C_4^{\text{opt}} := \frac{4 \cdot 10^{-2}}{1.59} \approx 2.52 \cdot 10^{-2},$$

as follows from desiring the largest correlation at the end of the spectrum (the value $1.59$ was the "best" time scale, $t^{\text{Conv}} = 1.59 t^{\boldsymbol{\tau}_4}$, in Figure 5.5). This figure clearly shows that both the convective term and $\boldsymbol{\tau}_4$ transport energy to the small scales in a similar way. Whereas at the smaller scales they do not, given this coefficient.

### 5.3.3 Triad interactions

Since the similarity of the temporal evolution of the energy spectra is a phenomenon observed in Fourier space, we consider both model terms in Fourier space.

The Fourier transform of the convective term is given by

$$\mathcal{F}\left\{\partial_m (w_m w_l)\right\}(\mathbf{k}) = i k_m \int_{\mathbb{R}^d} \hat{w}_m(\mathbf{p}) \hat{w}_l(\mathbf{k} - \mathbf{p}) d\mathbf{p},$$

where $\hat{w}_m(\mathbf{k}) := \mathcal{F}\{w_m\}(\mathbf{k})$. If for some $m, l$ it holds that $\hat{w}_m(\mathbf{p})$ and $\hat{w}_l(\mathbf{q})$ are nonzero, then this results in a contribution to the Fourier transform of the convective term at wave vector $\mathbf{k}$ for which

$$\mathbf{k} = \mathbf{p} + \mathbf{q}.$$

Such interactions of two wave vectors, resulting in a contribution to a third wave vector, is called a triad interaction. When considering LES there are several relevant and different types of triad interactions (Pope, 2001). The fully resolved triad interactions are those for which $\mathbf{k}, \mathbf{p}$ and $\mathbf{q}$ are contained in the wavenumber range $I_k$.

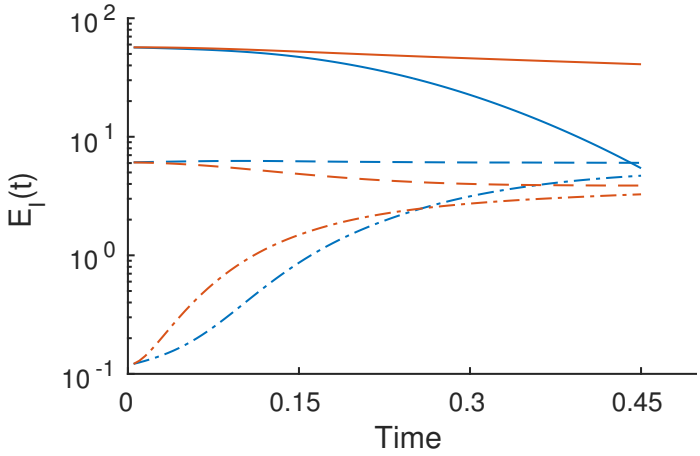


Figure 5.7: Energy content $E_I(t)$. Solid: $I = I_{\mathrm{L}}$. Dashed: $I = I_{\mathrm{I}}$. Dash-dotted: $I = I_{\mathrm{S}}$. Blue corresponds to convective term, red to $\boldsymbol{\tau}_4$ with $C_4 = C_4^{\mathrm{opt}}$.

Similarly we can consider the Fourier transform of the model term

$$-\nabla \cdot (\mathbf{S\Omega} - \mathbf{\Omega S}).$$

We first write

$$\mathbf{S\Omega} - \mathbf{\Omega S} = \frac{1}{2}(\mathbf{A}^T\mathbf{A} - \mathbf{A}\mathbf{A}^T), \quad \mathbf{A} = \nabla \mathbf{w},$$

the Fourier transform of $\mathbf{A}^T\mathbf{A}$ is given by

$$\begin{aligned}\mathcal{F}\left\{\mathbf{A}^T\mathbf{A}\right\}(\mathbf{k})_{ml} &= \int_{\mathbb{R}^d} \hat{A}_{nm}(\mathbf{p})\hat{A}_{nl}(\mathbf{k}-\mathbf{p})d\mathbf{p} \\ &= -\int_{\mathbb{R}^d} \hat{w}_n(\mathbf{p})\hat{w}_n(\mathbf{k}-\mathbf{p})p_m(k_l - p_l)d\mathbf{p}.\end{aligned}$$

Similarly the Fourier transform of $\mathbf{A}\mathbf{A}^T$ is given by

$$\mathcal{F}\left\{\mathbf{A}\mathbf{A}^T\right\}(\mathbf{k})_{ml} = -\int_{\mathbb{R}^d} \hat{w}_m(\mathbf{p})\hat{w}_l(\mathbf{k}-\mathbf{p})p_n(k_n - p_n)d\mathbf{p}.$$

The divergence operator in Fourier space is given by

$$\mathcal{F}\{\nabla \cdot \boldsymbol{\tau}\}(\mathbf{k})_l = ik_m \mathcal{F}\{\boldsymbol{\tau}_{ml}\}(\mathbf{k}),$$

which, applied to $\boldsymbol{\tau} = \boldsymbol{\tau}_4$, yields

$$\begin{aligned}&\mathcal{F}\{-\nabla \cdot (\mathbf{S\Omega} - \mathbf{\Omega S})\}(\mathbf{k})_l = \\ &\quad -ik_m \int_{\mathbb{R}^d} \left[\hat{w}_n(\mathbf{p})\hat{w}_n(\mathbf{k}-\mathbf{p})p_m(k_l - p_l) - \hat{w}_m(\mathbf{p})\hat{w}_l(\mathbf{k}-\mathbf{p})p_n(k_n - p_n)\right] d\mathbf{p}.\end{aligned}$$

From this expression we recognise triad interactions similar to those resulting from the convective term.

## 5.4 Application to LES - a priori

Here we consider whether the transport term $\boldsymbol{\tau}_4$ is in any way an approximation to the exact sub-filter scale stress tensor. Following the approach as presented in Berselli et al. (2005, Section 7.3.3), we consider the single-mode analysis of several model terms. This means that for some model tensor we consider a simple velocity field $\mathbf{u}$, compute the exact sub-filter scale tensor $\boldsymbol{\tau}^{\text{Exact}}(\mathbf{u})$ and compare this result with $\boldsymbol{\tau}^{\text{Model}}(\bar{\mathbf{u}})$. We at least must consider the two-dimensional case $d = 2$, since for $d = 1$ we have $\boldsymbol{\Omega} \equiv 0$.

Let's consider a velocity field containing a single mode, given by

$$u = e^{iKy}, \quad v = 0.$$

We consider a filter kernel (which will be specified later) $g_\delta(\mathbf{x})$ with its Fourier transform given by $\hat{g}_\delta(\mathbf{k})$. It follows that the filtered velocity field, $\bar{u}$, is given by

$$\bar{u}(y) = (g_\delta * u)(y) = \mathcal{F}^{-1}\left\{\hat{g}_\delta(k)\delta(k-K)\right\}(y) = \hat{g}_\delta(K)e^{iKy}.$$

Hence the exact sub-filter scale tensor is given by (only the $(1,1)$-component is nonzero)

$$\boldsymbol{\tau}_{11}^{\text{Exact}} = \overline{uu} - \bar{u}\bar{u} = (\hat{g}_\delta(2K) - \hat{g}_\delta(K)^2)e^{i2Ky}.$$

*Smagorinsky's model*

The application of Smagorinsky's model on the filtered velocity field yields the following model tensor

$$\begin{aligned}
\boldsymbol{\tau}^{\text{Smag}}(\bar{\mathbf{u}}) &= -(C_s\delta)^2|\mathbf{S}(\bar{\mathbf{u}})|\mathbf{S}(\bar{\mathbf{u}}) \\
&= -\frac{(C_s\delta)^2}{2\sqrt{2}}|\partial_y\bar{u}|\begin{bmatrix}0 & \partial_y\bar{u}\\ \partial_y\bar{u} & 0\end{bmatrix} \\
&= -i\frac{(C_s\delta)^2}{2\sqrt{2}}\hat{g}_\delta(K)^2e^{iKy}\begin{bmatrix}0 & 1\\ 1 & 0\end{bmatrix}.
\end{aligned}$$

*Gradient model*

Similarly, the Gradient model yields the following (for $\gamma = 6$)

$$\begin{aligned}
\boldsymbol{\tau}^{\text{Grad}}(\bar{\mathbf{u}}) &= \frac{\delta^2}{12}\nabla\bar{\mathbf{u}}\nabla\bar{\mathbf{u}}^T \\
&= \frac{\delta^2}{12}\begin{bmatrix}0 & \partial_y\bar{u}\\ 0 & 0\end{bmatrix}\begin{bmatrix}0 & 0\\ \partial_y\bar{u} & 0\end{bmatrix} \\
&= \frac{\delta^2}{12}\begin{bmatrix}(\partial_y\bar{u})^2 & 0\\ 0 & 0\end{bmatrix},
\end{aligned}$$

hence the only nonzero component is given by

$$\boldsymbol{\tau}_{11}^{\text{Grad}}(\bar{\mathbf{u}}) = -\frac{\delta^2K^2}{12}\hat{g}_\delta(K)^2e^{i2Ky}.$$

*General tensor model*

Since $d = 2$, there are only three linearly independent symmetric $2 \times 2$ tensors. For this particular velocity field it follows that only $\hat{\boldsymbol{\tau}}_0, \hat{\boldsymbol{\tau}}_1$ and $\hat{\boldsymbol{\tau}}_4$ are nonzero. Hence we consider $\hat{\boldsymbol{\tau}}_4 = \boldsymbol{\tau}_4$ since $\hat{\boldsymbol{\tau}}_1$ was considered already with the Smagorinsky model (up to scaling by some constant and $|\mathbf{S}(\bar{\mathbf{u}})|$).

$$\begin{aligned}\boldsymbol{\tau}_4(\bar{\mathbf{u}}) &= \mathbf{S}(\bar{\mathbf{u}})\boldsymbol{\Omega}(\bar{\mathbf{u}}) - \boldsymbol{\Omega}(\bar{\mathbf{u}})\mathbf{S}(\bar{\mathbf{u}}) \\ &= \frac{(\partial_y \bar{u})^2}{2}\begin{bmatrix}-1 & 0\\ 0 & 1\end{bmatrix} \\ &= \frac{K^2}{2}\hat{g}_\delta(K)^2 e^{i2Ky}\begin{bmatrix}1 & 0\\ 0 & -1\end{bmatrix}.\end{aligned}$$

It follows that up to a constant the $(1,1)$-component agrees with that of the Gradient model. However also the $(2,2)$-component is non-zero.

*Comparison*

Regardless of which filter kernel we choose, it is obvious that Smagorinsky's model does not seem to approximate the exact sub-filter scale tensor at all. Moreover, the $(1,1)$-component of $\boldsymbol{\tau}_4(\bar{\mathbf{u}})$ agrees up to a constant with that of the Gradient model. However, where the Gradient model correctly has $\tau_{22} = 0$ we have $(\boldsymbol{\tau}_4)_{22}(\bar{\mathbf{u}}) = -(\boldsymbol{\tau}_4)_{11}(\bar{\mathbf{u}}) \neq 0$, which yields an incorrect nonzero contribution to the $y$-momentum equation after taking the divergence (the exact sub-filter scale tensor yields no contribution at all to the momentum equations).

To be able to plot the amplification factor (in front of the $e^{i2Ky}$ term), we need to choose a filter. Let's consider the box filter, given by

$$\hat{g}_\delta(k) = \operatorname{sinc}(\delta k/2), \quad \operatorname{sinc}(x) = \frac{\sin x}{x}.$$

Hence the exact sub-filter scale tensor is given by

$$\tau_{11}^{\text{Exact}} = (\operatorname{sinc}(\delta K) - \operatorname{sinc}(\delta K/2)^2)e^{i2Ky},$$

and similarly the (nonzero component of the) Gradient model is then given by

$$\tau_{11}^{\text{Grad}}(\bar{\mathbf{u}}) = -\frac{\delta^2 K^2}{12}\operatorname{sinc}(\delta K/2)^2 e^{i2Ky}.$$

In Figure 5.8 we show the amplification factor as a function of $\delta K$ for both the exact sub-filter scale tensor and the Gradient model. Note that we do not show $\boldsymbol{\tau}_4$ since, up to scaling, the $(1,1)$-component is equal to that of the Gradient model. We also show the comparison when using the Gaussian filter. Indeed the Gradient model yields an approximation to the exact sub-filter scale tensor. This is according to our expectation since the Gradient model is constructed having modeling consistency in mind.

The idea of using $\boldsymbol{\tau}_4$ as being part of an LES model does not come from modeling consistency. However we do note that some components of $\boldsymbol{\tau}_4$ contain an approximation to the exact sub-filter scale tensor, this becomes apparent already from observing that

$$\boldsymbol{\tau}_4 = \mathbf{S}\boldsymbol{\Omega} - \boldsymbol{\Omega}\mathbf{S} = \frac{1}{2}(\mathbf{A}^T\mathbf{A} - \mathbf{A}\mathbf{A}^T).$$

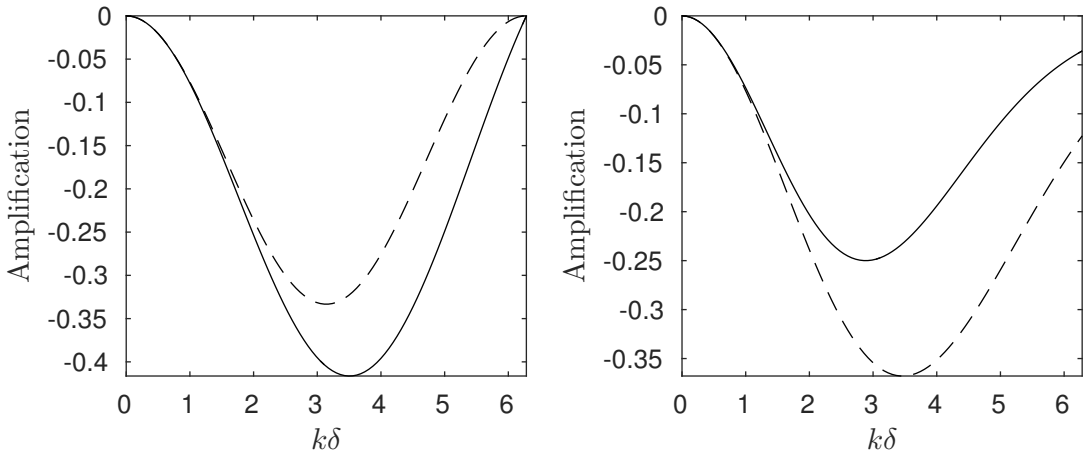


Figure 5.8: Left: the amplification factor when using the box filter, where the solid line denotes the exact value, and the dashed line denotes the value given by the Gradient model. Right: same for the Gaussian filter.

## 5.5 Application to LES - a posteriori

In this section, we discuss results of using $\boldsymbol{\tau}_4$ as the transport part of a LES model for the simulation of HIT. Mainly we try to make use of the observed properties of $\boldsymbol{\tau}_4$: it transports energy to higher wavenumbers, but is less active on lower wavenumbers when compared to the convective term. The expectation is that adding this term to the MNSE can indirectly increase or decrease the amount of total dissipation, since this process is more active on high wavenumbers. Moreover, if this term were to be used in combination with an eddy viscosity model, we expect we can use a smaller eddy viscosity while obtaining a similar decay in kinetic energy.

Hence we introduce a two-parameter model, given by

$$\boldsymbol{\tau} = C_1 \boldsymbol{\tau}^{\text{Smag}} + C_4 \boldsymbol{\tau}_4. \tag{5.13}$$

Using this model we simulate the MNSE, which were given by

$$\begin{aligned} \nabla \cdot \mathbf{w} &= 0, \\ \partial_t \mathbf{w} + \nabla \cdot (\mathbf{w} \otimes \mathbf{w}) + \nabla p - \frac{1}{\text{Re}} \Delta \mathbf{w} + \nabla \cdot \boldsymbol{\tau} &= 0, \\ \mathbf{w}(0) &= \mathbf{w}_0^{\text{HIT}}. \end{aligned}$$

### 5.5.1 The CBC experiment

To be able to assess the quality of the model (the next subsection discusses how we will do this) we need some reference data. A famous physical experiment, where the authors considered grid-generated decaying HIT, is given by the Comte-Bellot and Corrsin (CBC) experiment (Comte-Bellot and Corrsin, 1971).

In the physical experiment the authors considered a turbulent flow generated by a grid at the beginning of a wind tunnel. The turbulence is convected along the mean flow in the (by definition) streamwise direction. If we denote the mean flow velocity by $\mathcal{U}$, we can impose Taylor's hypothesis (Taylor, 1935),

and identify the streamwise direction in the physical experiment with the temporal direction in the numerical simulation of decaying HIT in a periodic box.

Measurements were done at three measurement stations, located at a distance $d_1, d_2$ and $d_3$ away from the grid. This yields, for our numerical simulation, three corresponding time instances given by

$$t_i = \frac{d_i}{\mathcal{U}},$$

where we will measure certain quantities.

For the numerical simulation we use an initial field, generated according to the procedure described in Rozema and Bae (2016), whose spectrum function at $t = t_1$ has been matched to that of the measured spectrum function in the experiment, at $d = d_1$. After the spectrum has been matched, we simulate sufficiently many time steps to ensure that the skewness structure function (5.14) has sufficiently converged (as was done in Kang et al. (2003)). The velocity field is then rescaled such that its spectrum function again matches that of the physical experiment at $d = d_1$.

### 5.5.2 Quality assessment of LES

The assessment of the resulting simulations of decaying HIT will be done by comparing several quantities measured in the CBC experiment. We are interested in quantities that are measured at all three time instances. This yields the following quantities which we will base our assessment on

- The total kinetic energy $E(t)$
- The energy spectrum function $E(k, t)$
- Both longitudinal as well as transversal two-point correlation functions, which we will denote by $f(r, t)$ and $g(r, t)$ respectively (as was done in Section 2.3)
- The non-dimensionalised third-order structure function $\tilde{D}_3^L(r, t)$. For small $r$, this structure function corresponds to the skewness of the longitudinal velocity derivative (Pope, 2001, Section 6.2), hence we will denote this structure function by

$$\mathcal{S}(r, t) := \tilde{D}_3^L(r, t). \tag{5.14}$$

### 5.5.3 Experimental results

Our approach is as follows. We first select some range of $(C_1, C_4)$-values for which we perform a LES. For each simulation we quantify how well the decay of kinetic energy matches that of the measured values from the CBC experiment. We then select only a few experiments based on this quantification, and study the resulting energy spectra.

Furthermore, for the same experiments, we compare the two-point correlation functions $f, g$ as well as the skewness structure function $\mathcal{S}$. Finally, as was discussed in Section 2.3, we quantify the two-point correlation functions, for small $r$, using the Taylor microscale.

*Energy*

We perform numerous numerical experiments solving the MNSE where the LES model is given by (5.13). We consider

$$(C_1, C_4) \in [0, 1.25] \times [-1 \cdot 10^{-3}, 4 \cdot 10^{-3}].$$

The $C_4$-range is chosen based on earlier simulations which showed that a further increase of $C_4$ does not have much effect on the energy decay. We also noticed this earlier in our model tests, where the end of the spectrum takes on the shape shown in Figure 5.2 (right) faster as the coefficient is increased.

In each parameter direction we take 31 values (such that the parameter values $C_1 = C_4 = 0$ and $C_1 = 1$ are among the parameter values), yielding a total of 961 simulations. Then for each simulation we compute the relative error $\tilde{r}(C_1, C_4)$ in terms of kinetic energy, as compared to the original data. Since the kinetic energy always matches the first data point at $t = t_1$ we omit this data in measuring the error. This yields the correlation isolines as shown in Figure 5.9. Note again that, especially for small

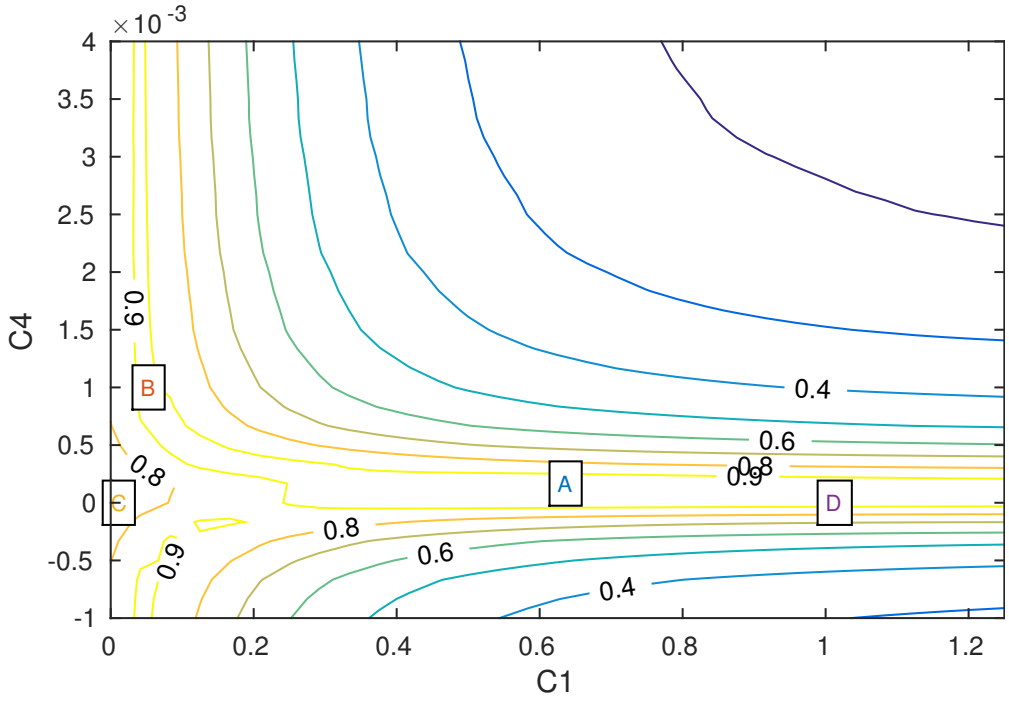


Figure 5.9: Correlation $\tilde{r}(C_1, C_4)$ (in terms of kinetic energy decay) isolines. Note: the colored letters do not indicate the correlation value, but instead match the colors in later figures when plotting other measured quantities.

values of $C_1$, the correlation value $\tilde{r}$ tends to some constant value as $C_4$ reaches its maximum value, hence justifying our choice for the maximum value of $C_4$.

Among the experiments we picked a few interesting parameter values, which are labeled by the capitalised letters 'A', 'B', etc.. The corresponding parameter values are shown in Table 5.1, for completeness we also included a simulation with the QR model. 'A' corresponds to the simulation which yielded the highest correlation value $\tilde{r}$. 'B' is picked for its smallness of the Smagorinsky coefficient while still yielding an OK correlation value $\tilde{r}$. 'C' and 'D' correspond to no model and the usual Smagorinsky model respectively.

The temporal evolution of kinetic energy for each of the simulations is shown in Figure 5.10. As expected, the additional transport of energy to the end of the spectrum indeed increases the total dissipation. Moreover, for each of the simulations we show the corresponding energy spectra at times $t = t_2, t_3$ in Figure 5.11. The cause of this additional dissipation can again be observed by studying the energy spectrum functions. The additional transport to higher wavenumbers, caused by a nonzero coefficient $C_4$, results in additional dissipation, but also in a small pile-up of energy at the end of the spectrum since the additionally transported energy is too much for the dissipative term to "absorb".

| Label | $C_1$ | $C_4$ | $\tilde{r}$ |
|---|---|---|---|
| A | 0.62 | $1.667 \cdot 10^{-4}$ | 0.986722 |
| B | 0.04 | $10^{-3}$ | 0.915354 |
| C | 0.00 | 0 | 0.698345 |
| D | 1.00 | 0 | 0.950277 |
| QR | NA | NA | 0.967415 |

Table 5.1: Parameter values, and their corresponding labels and correlation values.

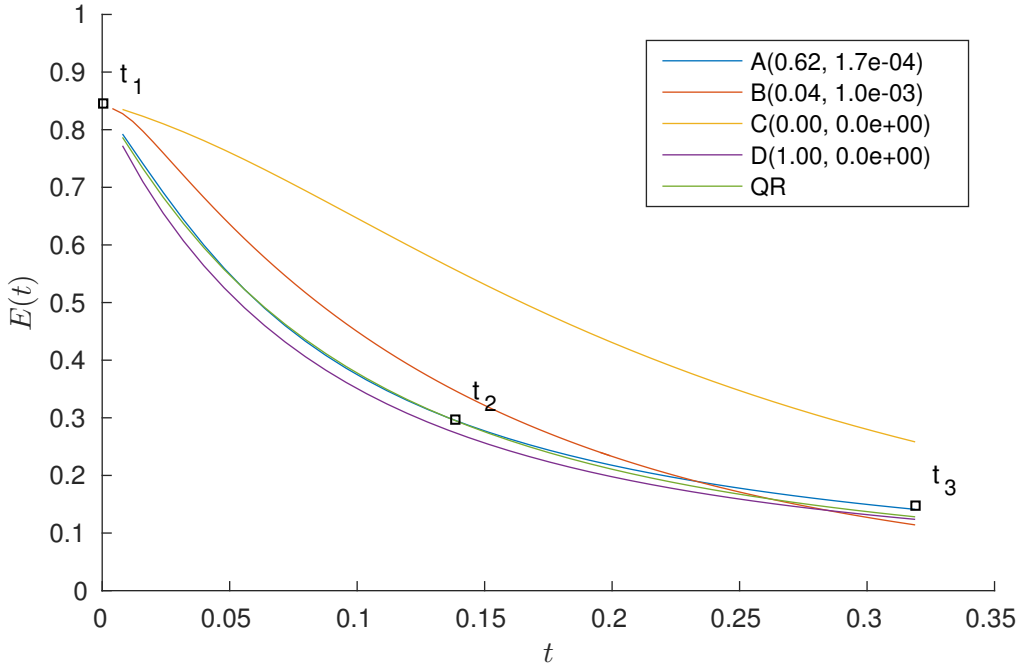


Figure 5.10: Temporal evolution of the kinetic energy for several values of $(C_1, C_4)$. Where (A) blue = best correlation $\tilde{r}$, (B) red = $(0.04, 10^{-3})$, (C) yellow = no model, (D) purple = Smagorinsky, green = QR.

*Two-point correlation functions*

In the CBC experiment both the longitudinal structure function $R_{11}(r\mathbf{e}_1, t)$ (will be denoted by $f(r,t)$) as well as the transversal structure function $R_{11}(r\mathbf{e}_2, t)$ (will be denoted by $g(r,t)$) were measured. For the selected simulations we show both the longitudinal as well as the transversal correlation function in Figure 5.12. Note that we do not show the structure functions at $t = t_1$ since all simulations used the same initial field.

We observe that for the eddy viscosity models, as well as simulation 'A' corresponding to the combination $(C_1, C_4)$ yielding the highest correlation $\tilde{r}$, the correlation functions $f$ and $g$ increases in time. Moreover for these simulations the two-point correlations match the experimental data quite well. For the simulation using no model and the simulation using a relatively large value of $C_4$, the correlation is much lower. Note that these two simulations also suffer from a pile-up of energy at the end of the spectrum. This correspondence makes sense since such an excess of energy at the end of the spectrum results in a strong presence of small-scale structures, hence resulting in a lower correlation for small increments $r$.

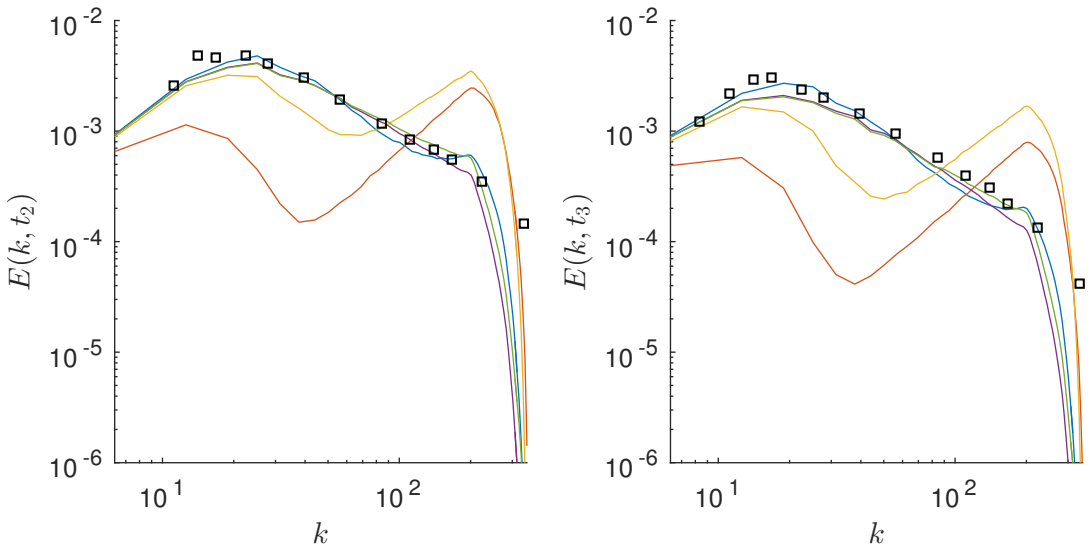


Figure 5.11: Energy spectra at the measurement times $t = t_2$ (left) and $t = t_3$ (right). Where (A) blue = best correlation $\tilde{r}$, (B) red = $(0.04, 10^{-3})$, (C) yellow = no model, (D) purple = Smagorinsky, green = QR.

It follows that using a transport term like $\boldsymbol{\tau}_4$ as a part of a LES model does not worsen the agreement to two-point correlation functions.

As a measure of isotropy we consider verifying the relation (2.7), which was given by

$$g(r,t) = f(r,t) + \frac{r}{2}\frac{\partial f(r,t)}{\partial r}. \tag{5.15}$$

We define the correlation between $g(r,t)$ and the approximation defined by the right-hand side of (5.15) as one minus the relative error between both functions (as in (5.11)). The resulting correlation values are shown in Figure 5.13.

For the simulation with the QR and Smagorinsky model, as well as simulation 'A' (best correlation), the isotropy is maintained about equally well in time for all three simulations. The simulations using either no model or having a relatively large coefficient $C_4$ yield significantly worse correlation values, indicating a decrease in isotropy during these simulations.

*Estimation of Taylor microscale*

In Section 2.3 we discussed that for small increments $r$ the longitudinal and transversal two-point correlation functions are fully characterised by the Taylor microscale (or equivalently, by the second derivative at $r = 0$). Hence for small increments $r$ the Taylor microscale yields a characterisation of the two-point correlation functions.

For the computation of the Taylor microscale we must approximate the second derivative of a correlation function at $r = 0$. Suppose we have a correlation value located at $r = h$ (where $h$ is the mesh width). Together with the fact that the correlation function equals one at $r = 0$ and that it is even about $r = 0$ this yields the following approximation to, for example, the transversal Taylor microscale $\lambda_g(t)$

$$\lambda_g(t) \approx \sqrt{-2\frac{h^2}{g(h,t) - 2g(0,t) + g(-h,t)}} = h\sqrt{\frac{1}{1 - g(h,t)}}.$$

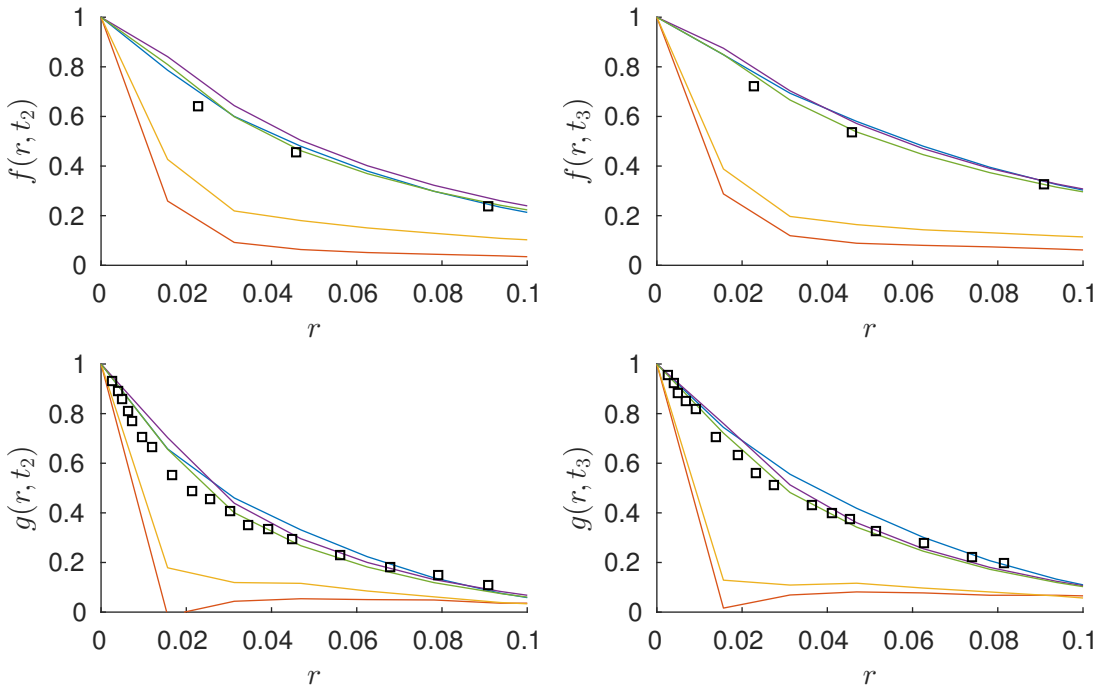


Figure 5.12: Longitudinal (top) and transversal (bottom) correlation functions at two time instances $t = t_2$ (left) and $t = t_3$ (right). Where (A) blue = best correlation $\tilde{r}$, (B) red = $(0.04, 10^{-3})$, (C) yellow = no model, (D) purple = Smagorinsky, green = QR.

Unfortunately, the longitudinal two-point correlation function, as shown in Figure 5.12, is not measured for small increments $r$ in the CBC experiment. Fortunately however, we can argue that, due to (5.15), the transversal two-point correlation function $g$ is sufficient. More precisely, for homogeneous and isotropic velocity fields, the longitudinal and transversal Taylor microscales differ up to a constant factor $\sqrt{2}$. This follows directly from (5.15).

When computing the Taylor microscale in the simulation, we encounter similar problems as we did when using the measured CBC data. For $64^3$ grid points, the resolution simply isn't high enough to be able to compute a good approximation to the Taylor microscale. Hence we also performed simulations on a higher resolution, using $128^3$ grid points. For these simulations we scaled the coefficient $C_4$ using the fact that its dimensions are given by $m^2$ (as given by (3.9)). Hence we reduce the coefficient $C_4$ by a factor four.

The resulting temporal evolution of the transversal Taylor microscale is shown in Figure 5.14. Note that, again, the simulations using either no model or having a relatively large coefficient $C_4$ yield different results than the other three simulations. However, since the isotropy of the velocity field is significantly reduced for these simulations, as follows from Figure 5.13, we no longer consider the Taylor microscale as a characterisation of the normalised two-point correlation tensor $\tilde{\mathbf{R}}(\mathbf{r}, t)$.

The simulations 'A', 'D' and QR yield a qualitatively similar temporal evolution of the Taylor microscale when compared to the CBC data, that is, it increases in time. We expect that further mesh refinement may yield quantitatively better results since the refinement from $N = 64$ to $N = 128$ already improved the agreement of the correlation functions significantly, see for example Figure 5.15. However, further mesh refinement would result in almost performing a DNS, which is of course not the purpose of our research.

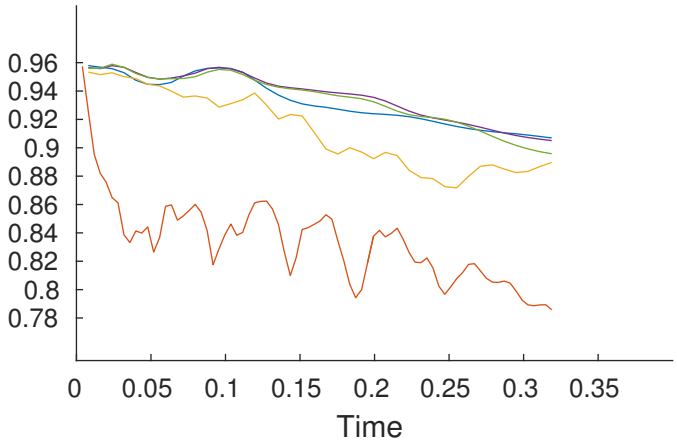


Figure 5.13: Measure of isotropy, which follows from (5.15). Here we plot the correlation between the actual transversal two-point correlation function $g(r,t)$ and its approximation based on the longitudinal two-point correlation function $f(r,t)$. Where (A) blue = best correlation $\tilde{r}$, (B) red = $(0.04,\ 10^{-3})$, (C) yellow = no model, (D) purple = Smagorinsky, green = QR.

*Skewness structure function*

We finally consider the longitudinal skewness structure function $\mathcal{S}$. In Figure 5.16 we show the longitudinal skewness structure function at the two time-instances $t = t_2, t_3$.

Note that when using no model and even more for the simulation with a relatively large coefficient $C_4$, the skewness tends to zero for all values of $r$. This indicates that the probability density function of the longitudinal velocity gradient is symmetric in these simulations, where it should not be.

For both the QR model as simulations 'A' and 'D', the skewness coefficient agrees somewhat to the hypothesised universal range of values (Cerutti et al., 2000) of

$$-\mathcal{S} \in [0.3, 0.4].$$

Except for the QR model, which yields a constant value of $\mathcal{S}$ for two grid points (i.e. values of $r$), all other simulations did not show a constant value in the inertial range. Such a constant value, however, is to be expected from Kolmogorov's theory.

Similar to the observations done when considering the two-point correlation functions, we find that also the skewness is not affected much when using a transport term as part of a LES model.

## 5.6 Conclusion

In this chapter we considered the use of a nonlinear transport term as part of a LES model. Contrary to eddy-viscosity models, such a model also models the non-dissipative part of the exact sub-filter scale stress tensor.

By comparing the temporal evolution of the energy spectrum functions using such a transport term in the model problem (5.1) we found that this particular term results in a net transport of kinetic energy from large (medium) scales of motion to small scales. The hypothesis was then that we could use such a mechanism to indirectly increase the total dissipation due to the LES model. Using the test case of decaying HIT in a periodic box we confirmed that this is indeed possible by considering a two-parameter LES model containing a purely dissipative and purely non-dissipative part. Introducing this transport

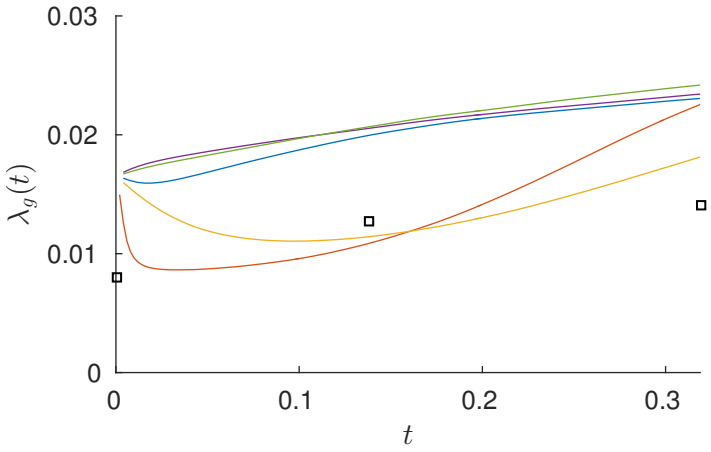


Figure 5.14: Estimation of the transversal Taylor microscale, based on a simulation using $128^3$ grid points. (A) blue = best correlation $\tilde{r}$, (B) red = $(0.04, 10^{-3})$, (C) yellow = no model, (D) purple = Smagorinsky, green = QR.

term, allowed the reduction of the amount of eddy-viscosity, while obtaining a similar decay in kinetic energy.

When only considering the decay in kinetic energy we merely analyse the dissipative behaviour of the model. To obtain good dissipative behaviour however, a purely dissipative model is sufficient. Therefore we also consider other quantities like the energy spectrum function, which, when considered as a function of time, provides insight on how the energy is distributed among the different scales of motion. We found that the introduction of a transport term resulted in a small pile-up of energy at the smallest scales. This was to be expected since the use of such a transport term increases the transport of energy to small scales, while simultaneously reducing the amount of dissipation.

Besides kinetic energy (per wavenumber) we also considered several statistical measures. For instance we considered the two-point correlation function. Here we found that the use of a transport term does not worsen the agreement to experimental data of such statistical measures.

These are promising results in the sense that this shows that the general framework of LES models proposed earlier contains a lot of freedoms (more transport terms, but also dependence of the coefficients on the invariants) which can be explored without affecting the dissipative properties of the LES model. Hence allowing the modelling of non-dissipative mechanisms in a LES model, while maintaining good agreement to the decay of kinetic energy.

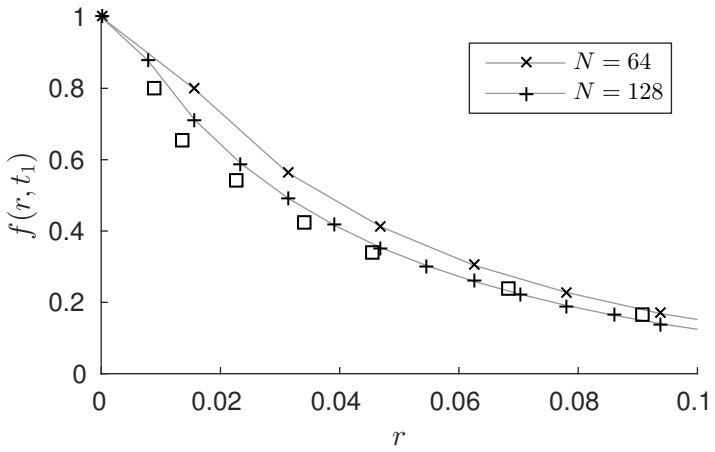


Figure 5.15: Longitudinal two-point correlation function. Comparison between $64^3$ and $128^3$ gridpoints.

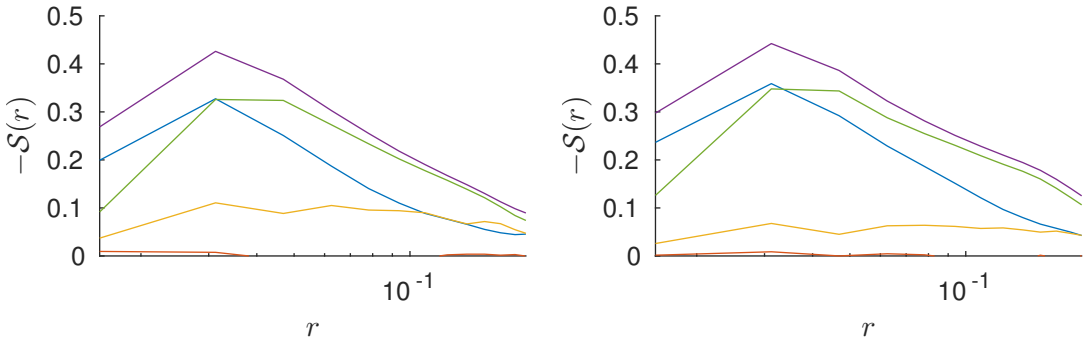


Figure 5.16: Longitudinal skewness structure function at the two time instances $t_2$ (left) and $t_3$ (right). Where (A) blue = best correlation $\tilde{r}$, (B) red = $(0.04, 10^{-3})$, (C) yellow = no model, (D) purple = Smagorinsky, green = QR.

# Chapter 6

# Discussion

## 6.1 Summary

The Navier-Stokes equations (NSE) are a model for fluid flow. When simulating a turbulent flow at high Reynolds number the required resolution to capture all scales of motion is too high. Therefore we want to find equations that govern the temporal evolution of the local spatial average of the velocity field instead. Due to the nonlinearity of the NSE, expressing the equations merely in terms of the local spatial average of the velocity field requires a model which describes the interaction of the small scales of motion (not represented in the simulation) with the large scales of motion. Such a model is called a Large Eddy Simulation (LES) model. There is a large variety of such LES models, perhaps the most common ones are given by eddy-viscosity models. In an eddy-viscosity model the aim is to model the dissipative behaviour of the interaction between the small and large scales of motion. Eddy-viscosity models are generally functions of the velocity gradient.

An example of a non-eddy-viscosity model is the Gradient model, which depends nonlinearly on the velocity gradient. This model is a mathematically consistent approximation to the exact interactions between the small and large scales of motion. The Gradient model is not purely dissipative (like an eddy-viscosity model) and therefore also models some transport mechanism. The Gradient model, however, turns out to be inherently unstable. One way of stabilising this model is by using only it's dissipative part. Thereby decomposing the Gradient model in it's dissipative and transport part.

We then propose a generalisation of the previously mentioned LES models: we assume the LES model to be a function of the velocity gradient. Moreover, we generalise the separation of dissipation and transport mechanisms by means of orthogonalisation. This yields a framework of LES models expressed in terms of a linear combination of eleven model tems. Only one of these terms is dissipative and is included in the previously mentioned eddy-viscosity models. The Gradient model can also be represented in this framework. The research done in this report is aimed at finding out how to use the transport terms as a part of a LES model, and therefore also modelling the non-dissipative interactions between the small and large scales of motion. This research will be done by means of numerical experiments which are verified by comparison to other LES models as well as experimental data.

Before such simulations can be done, we need a suitable discretisation method. We choose to use a symmetry-preserving Finite Volume (FV) discretisation method. Here, symmetry-preserving indicates the preservation of symmetry properties of certain differential operators present in the NSE in the discretisation. This results in a discrete equivalent to the analytical energy equality. Such preservation of symmetry properties is desirable since it results in stability properties in the simulation.

We extend this symmetry-preserving discretisation by discretising the contribution of the LES model to the momentum equation. We consider several methods for discretising the LES model. Such methods

are second-order accurate and may be extrapolated. Moreover we emphasise the importance of preserving the energy equality in the discretisation and therefore desire local orthogonality properties as well as zero contribution to the discrete energy equality whenever the model is non-dissipative. This results in choosing a single discretisation method which we use in the research that follows. Simulations using a non-dissipative term confirm the importance of preserving the energy equality in the discretisation: a discretisation method which does not preserve this results in an unstable simulation.

Provided with this discretisation method we can now start characterising the terms present in the general framework of LES models. We choose a single transport term. By comparing the simulation of merely this term to a known transport term, given by the convection operator, we are able to characterise this transport term in terms of how it distributes kinetic energy over the scales of motion. We find that the net result is transport from large (medium) to small scales of motion. Therefore we expect that in combination with a dissipative term we can obtain a similar decay in kinetic energy as a purely dissipative model (eddy-viscosity model), while using less eddy-viscosity.

To test this hypothesis we use the test case of decaying Homogeneous and Isotropic Turbulence (HIT) in a periodic box. We propose a two-parameter LES model which is a linear combination of a dissipative term and a non-dissipative term given by the previously characterised transport term. We perform numerous simulations and quantify the agreement to the kinetic energy decay from the experimental data. This results in a single set of parameters for which this agreement is optimised. Such a comparison only assesses the dissipative behaviour of the LES model. To obtain good dissipative behaviour however, a purely dissipative model is sufficient. Therefore we also consider other quantities like the energy spectrum function, which, when considered as a function of time, provides insight on how the energy is distributed among the different scales of motion.

We find that the introduction of a transport term results in a small pile-up of energy at the smallest scales. This is to be expected, since we simultaneously increase the transport of energy to small scales of motion, as well as decrease the amount of dissipation (which is most active at small scales of motion).

Besides kinetic energy (per wavenumber) we also consider several statistical quantities. For instance, we compute the two-point correlation functions which are also available from the experimental data. Here we find that using a transport term as part of a LES model does not worsen the agreement to the experimental data in terms of the statistical measures. This may not sound optimistic at first, however such results are promising in the sense that we have shown that using a transport term to model the non-dissipative part of the interaction between the small and large scales of motion results in good dissipative properties while maintaining similarly good agreement in terms of statistical measures. Hence allowing the modelling of non-dissipative mechanisms in a LES while maintaining the previously mentioned good agreement. Such modelling is of course far from fully explored in this work.

## 6.2 Future work

Having this general framework of tensor models, together with a suitable discretisation method, a lot of research and experimentation can be done since a lot of freedoms (e.g. the use of the invariants) are still to be explored. Such freedoms can (and should) be restricted by imposing mathematical and physical consistency conditions. This approach reduces the amount of possible LES models we can consider, but also allows us to study which of these conditions are actually important.

Also, more test cases should be considered. The simulation of HIT in a periodic box is perhaps the simplest test case involving the simulation of a turbulent flow since it merely addresses the interior closure problem. Therefore wall bounded flows should also be considered, where for instance, near-wall scaling laws may be imposed.

# Appendix A

# Preliminaries

## A.1 Function spaces

Important results regarding existence and uniqueness of solutions to the Navier-Stokes equation depend heavily on Lebesgue spaces and the theory surrounding such spaces. We briefly recall some definitions and notation regarding Lebesgue spaces, weak derivatives and Sobolev spaces. This brief summary is in no way intended to be an introduction to the theory of Sobolev spaces, it is merely intended to establish consistent notation.

To indicate an arbitrary (possibly mixed and/or higher order) derivative we use multi-index notation. Given a multi-index $\alpha = (\alpha_1, \ldots, \alpha_d) \in \mathbb{N}^d$, the derivative with respect to $\alpha$ is defined as

$$\partial_\alpha f := \frac{\partial^{|\alpha|} f}{\partial^{\alpha_1} x_1 \ldots \partial^{\alpha_d} x_d},$$

where the sum of the components of the multi-index is given by

$$|\alpha| := \sum_{j=1}^{d} \alpha_j.$$

**Definition A.1** ($L^p$ norm & $L^p$ spaces)**.** *Given a real valued function $f$*

$$f : \mathbb{R}^d \supset \Omega \to \mathbb{R},$$

*we define the $L^p$ norm, for $1 \leq p \leq \infty$, as*

$$\|f\|_{L^p(\Omega)} := \left( \int_\Omega |f|^p \, d\mathbf{x} \right)^{1/p},$$

*in the case of $1 \leq p < \infty$. And for $p = \infty$ we have*

$$\|f\|_{L^\infty(\Omega)} := \operatorname*{ess\,sup}_{x \in \Omega} |f(x)|.$$

*If no subscript is added the $L^2$ norm is implied, that is*

$$\|f\| := \|f\|_{L^2(\Omega)}.$$

*Moreover, we define the Lebesgue space $L_p$ as*

$$L^p(\Omega) := \left\{ f \,;\, \|f\|_{L^p(\Omega)} < \infty \right\}.$$

**Definition A.2** (Locally integrable function)**.** *A function $f$ is said to be locally integrable on $\Omega$ if $f \in L^1(K)$ for any compact subset $K \subset \mathring{\Omega}$. The space of locally integrable functions with respect to domain $\Omega$ is denoted by $L^1_{\text{loc}}(\Omega)$.*

It turns out that requiring solutions to the MNSE to be differentiable in the usual sense is too strict, hence we weaken this notion by introducing the notion of a weak derivative.

**Definition A.3** (Weak derivative)**.** *The function $f \in L^1_{\text{loc}}(\Omega)$ is said to have a weak derivative (of order $\alpha$) if there is some function $g \in L^1_{\text{loc}}(\Omega)$ such that*

$$\int_\Omega f \partial_\alpha \phi \, d\mathbf{x} = (-1)^{|\alpha|} \int_\Omega g\phi \, d\mathbf{x}, \quad \forall \phi \in C_0^\infty.$$

*The function $g$ is said to be the weak derivative of $f$ and is denoted by*

$$D_w^\alpha f = g.$$

**Definition A.4** (Sobolev norm & Sobolev spaces)**.** *Given a non-negative integer $k$ and $0 \leq p \leq \infty$. Let $f$ be a locally integrable function on $\Omega$. Suppose that weak derivatives $D_w^\alpha f$ exist for $|\alpha| \leq k$. The Sobolev norm is defined by*

$$\|f\|_{W_p^k(\Omega)} := \left( \sum_{|\alpha| \leq k} \|D_w^\alpha f\|^p_{L^p(\Omega)} \right)^{1/p}.$$

*Consequently, the Sobolev space $W_p^k(\Omega)$ is defined by*

$$W_p^k(\Omega) := \left\{ f \in L^1_{\text{loc}}(\Omega) \, ; \, \|f\|_{W_p^k(\Omega)} < \infty \right\}.$$

Often we will consider $p = 2$ since, as it turns out, in this special case the space is a Hilbert space. Hence we introduce the notation

$$H^k(\Omega) := W_2^k(\Omega).$$

Moreover we define the $L^2(\Omega)$ inner product $\langle \cdot, \cdot \rangle_{L^2(\Omega)}$ by

$$\langle f, g \rangle \equiv \langle f, g \rangle_{L^2(\Omega)} := \int_\Omega fg \, d\mathbf{x}.$$

When considering solutions to the Navier-Stokes equations, we consider vector valued functions, for example $\mathbf{u} \in [L^2(\Omega)]^d$. For convenience we define the solenoidal subspace of $[L^2(\Omega)]^d$, given by

$$L^2_\sigma(\Omega) := \left\{ \mathbf{u} \in [L^2(\Omega)]^d \, ; \, \nabla \cdot \mathbf{u} = 0, \mathbf{u} \cdot \mathbf{n} = 0 \right\}.$$

Using this definition we may omit the continuity equation if we search for solutions in $L^2_\sigma(\Omega)$. The divergence free restriction is considered in a weak sense. Norms and inner products on vector valued functions (or tensors) follow from those defined on scalar valued functions. For example

$$\langle \mathbf{f}, \mathbf{g} \rangle_{L^2(\Omega)} = \int_\Omega \mathbf{f} \cdot \mathbf{g} \, d\mathbf{x},$$

and

$$\|\mathbf{f}\|_{L^2(\Omega)} = \left( \int_\Omega |\mathbf{f}|^2 \, d\mathbf{x} \right)^{1/2},$$

where $|\mathbf{f}|$ denotes the Euclidean norm on $\mathbb{R}^d$.

Finally we must also consider function spaces in which time-dependent solutions are considered. To this purpose we define the following notation

$$L^p(0,T;\mathcal{B}) := \left\{ f : (0,T) \to \mathcal{B} \,;\, \left( \int_0^T \|f(t)\|_{\mathcal{B}}^p \, dt \right)^{1/p} < \infty \right\},$$

for $1 \leq p < \infty$, and analogous to Definition A.1 for $p = \infty$.

# Appendix B

# Derivations

## B.1 Symmetries of the NSE

Suppose $\mathbf{u}(\mathbf{x},t), p(\mathbf{x},t)$ is a solution to the NSE, then such a solution is invariant under translation, Galilean boosts and rotations.

*Translation invariance*

Let $\mathbf{u}'(\mathbf{x},t), p'(\mathbf{x},t)$ be given by

$$\mathbf{u}'(\mathbf{x},t) = \mathbf{u}(\mathbf{x}+\mathbf{L},t), p'(\mathbf{x}+\mathbf{L},t),$$

for some fixed vector $\mathbf{L}$. It follows that

$$\partial_m \mathbf{u}'(\mathbf{x},t) = \partial_m \mathbf{u}|_{\mathbf{x}+\mathbf{L},t}\,,$$

and similarly for the pressure. Hence the primed velocity field and pressure indeed also satisfy the NSE.

*Rotation invariance*

Let $\mathbf{u}'(\mathbf{x},t), p'(\mathbf{x},t)$ be given by

$$\mathbf{u}'(\mathbf{x},t) = \mathbf{R}\mathbf{u}(\mathbf{R}^{-1}\mathbf{x},t), p'(\mathbf{R}^{-1}\mathbf{x},t),$$

for some constant rotation matrix $\mathbf{R} = \mathbf{R}^{-T}$. We consider the terms of the NSE one by one, starting off with the time derivative term

$$\partial_t \mathbf{u}'(\mathbf{x},t) = \mathbf{R}(\partial_t \mathbf{u}(\mathbf{R}^{-1}\mathbf{x},t)).$$

The velocity gradient transforms like

$$(\nabla \mathbf{u}')_{mn} = \partial_m u'_n = R_{np}\partial_m u_p(\mathbf{R}^{-1}\mathbf{x},t) = R_{np}(R^{-1})_{lm}\ \partial_l u_p|_{\mathbf{R}^{-1}\mathbf{x},t} = (\mathbf{R}(\nabla \mathbf{u})\mathbf{R}^{-1})_{mn}, \quad \text{(B.1)}$$

hence for the convective term we get

$$\begin{aligned}(\mathbf{u}'\cdot\nabla\mathbf{u}')_n &= u'_m\partial_m u'_n \\ &= R_{mr}u_r(\mathbf{R}^{-1}\mathbf{x},t)R_{np}(R^{-1})_{lm}\ \partial_l u_p|_{\mathbf{R}^{-1}\mathbf{x},t} \\ &= R_{np}u_l(\mathbf{R}^{-1}\mathbf{x},t)\ \partial_l u_p|_{\mathbf{R}^{-1}\mathbf{x},t} \\ &= (\mathbf{R}(\mathbf{u}\cdot\nabla\mathbf{u}))_n.\end{aligned}$$

And for the pressure we get

$$(\nabla p')_n = \partial_n p' = \partial_m p|_{\mathbf{R}^{-1}\mathbf{x},t}\,(R^{-1})_{mn} = R_{nm}\,\partial_m p|_{\mathbf{R}^{-1}\mathbf{x},t} = (\mathbf{R}\nabla p)_n.$$

Finally, the Laplace term yields

$$\Delta u'_n = \partial_m \partial_m u'_n = R_{np}(R^{-1})_{lm}\,\partial_l \partial_r u_p|_{\mathbf{R}^{-1}\mathbf{x},t}\,(R^{-1})_{rm} = (\mathbf{R}\Delta\mathbf{u})_n.$$

The transformed velocity field is also divergence free, since taking the trace of the transformation rule for the velocity gradient (B.1) yields

$$\begin{aligned}\nabla \cdot \mathbf{u}' &= \partial_m u'_m \\ &= R_{mp}(R^{-1})_{lm}\,\partial_l u_p|_{\mathbf{R}^{-1}\mathbf{x},t} \\ &= \partial_l u_l|_{\mathbf{R}^{-1}\mathbf{x},t} \\ &= \nabla \cdot \mathbf{u}.\end{aligned}$$

We conclude that indeed $\mathbf{u}', p'$ yields a solution to the NSE.

*Galilean invariance*

For Galilean invariance it suffices to consider the time derivative term and the convective term, since the other terms remain (trivially) unchanged. We consider the following velocity field and pressure

$$\mathbf{u}'(\mathbf{x},t) = \mathbf{u}(\mathbf{x} - \mathbf{U}t, t) + \mathbf{U}, p'(\mathbf{x} - \mathbf{U}t, t),$$

for some constant velocity vector $\mathbf{U}$. The time derivative term transforms like

$$\partial_t u'_n = \partial_t|_{\mathbf{x}-\mathbf{U}t,t} - \partial_m u_n|_{\mathbf{x}-\mathbf{U}t,t}\,\mathbf{U}_m.$$

Whereas for the convective term we get

$$u'_m(\partial_m u'_n) = (\,u_m|_{\mathbf{x}-\mathbf{U}t,t} + \mathbf{U}) \cdot (\,\partial_m u_n|_{\mathbf{x}-\mathbf{U}t,t}).$$

Since the two additional terms are the same up to the sign, it follows that the NSE are invariant under Galilean transformations.

# Appendix C

# Implementation details (FORTRAN)

## C.1 Finite Volume discretisation

Here we briefly describe the implementation of the FV discretisation of the tensor model, that is, the computation of $\mathbf{T}(\mathbf{u}^h)$, when using Method 2.1. The structure of the FORTRAN-code is as follows: (we start our description inside INTGRT_OL, which is called inside the main loop)

1. Appropriate boundary conditions on the velocity unknowns are imposed. That is, the values of the velocity field in the "ghost cells" are computed. This is done using the already provided subroutines BNDCDU, BNDCDV and BNDCDW. These subroutines are called inside INTGRT_OL (inside integrates_OL_method2s, explicit one-leg method).

2. Inside INTGRT_OL the subroutine EVAL_RHS is called. This evaluates the right-hand side of the momentum equation of the full MNSE *except* for the pressure contribution, hence it evaluates

$$-\mathbf{C}(\mathbf{u}^h)\mathbf{u}^h - \frac{1}{\mathrm{Re}}\mathbf{D}\mathbf{u}^h - \mathbf{T}(\mathbf{u}^h). \tag{C.1}$$

   Note that each of the separate contributions can be switched off using the modelPar parameter file: cterm, dterm and tterm respectively. Conservation of mass (and hence the pressure term) can be switched off using pterm.

3. Inside EVAL_RHS the convective and diffusive terms are calculated (as they are defined in Verstappen and Veldman (2003)). Then the tensor model contribution is calculated:

   (a) First the staggered velocity gradient is computed $(\nabla \mathbf{w})^h_{i,j,k}$ using the subroutine STAGGRADUVW (inside gradtensor_method2.f).

   (b) Then the staggered velocity gradient is interpolated to location 1, that is, the center of the control volumes. This yields $(\nabla \mathbf{w}^{(1)})^h_{i,j,k}$. This is done using the subroutine COLGRADUVW (inside gradtensor_method2.f).

   (c) Now the tensor model is computed at location 1, using the subroutine MODEL (inside modeltensor_method2s.f, method2s was the old name used for Method 2.1):

      i. The symmetric and skew symmetric parts of the velocity gradient are computed.

      ii. Using these tensors, the required number (this is the parameter numbrtens inside modelPar) of symmetrised tensors (3.4) are computed.

| $l$ | $k$ |
|---|---|
| 1 | 2 |
| 2 | 3 |
| 3 | 2 |
| 4 | 6 |
| 5 | 9 |
| 6 | 10 |

Table C.1: Read as: "$\alpha_l$ is computed during the computation of $\boldsymbol{\tau}_k$". An overview showing at which step inside the subroutine `MODEL` the invariants are computed.

iii. During the computation of these symmetrised terms, the invariants (3.5) are computed as well.

iv. Then, optionally (the parameter `orth` inside `modelPar`), the tensors are orthogonalised according to (4.13).

v. The next step is the computation of the coefficients $\alpha_l(\mathbf{x}^{(1)}_{i,j,k}, t)$. This is done in the subroutine `COMPUTECOEFF` (inside `compute_coeff.f`). This subroutine computes the coefficients from functional relationships on the invariants. The type of functional relationship of $\alpha_l$ is determined by the parameter `al` inside `modelPar`. The actual functional relationship must be "hard coded" inside `COMPUTECOEFF`.

vi. Since $\boldsymbol{\tau}_1$ is directly used, without the double interpolation, it follows that we must therefore interpolate the coefficients $\alpha_1(\mathbf{x}^{(1)}_{i,j,k}, t)$ to the staggered locations. Before we do so, boundary conditions must be imposed, this is done using `BNDCTM_loc1` (inside `bndctm.f`).

vii. We then compute the tensor model at location 1 (except for the contribution by $\boldsymbol{\tau}_1$). Each tensor term is premultiplied by its coefficient $\alpha_l$, as well as an additional scaling parameter which can be set inside `modelPar` using `cl` (there called, "model coefficients").

viii. The next step is to impose boundary conditions on the collocated tensor using `BNDCTM_loc1_coll` (inside `bndctm.f`), and then construct the staggered model tensor $(\boldsymbol{\tau})^h_{i,j,k}$ by combining the contribution from the staggered $(\boldsymbol{\tau}_1)^h_{i,j,k}$ as well as the contribution from the interpolated tensor terms located at location 1 (calculated in the previous step).

This yields $(\boldsymbol{\tau}^{(1)})^h_{i,j,k}$. Also inside this subroutine, the tensor model is interpolated back to the staggered location, yielding $(\boldsymbol{\tau})^h_{i,j,k}$. Note that only the elements $n \geq m$ (upper triangular part of $\tau_{mn}$) are evaluated.

(d) Next the boundary conditions are imposed on the model tensor.

(e) Note that all these steps are repeated for the three times larger control volumes if the desired spatial order equals four.

(f) Finally the surface integrals are computed inside the subroutines `DIVTU`, `DIVTV` and `DIVTW` (located inside `divtensu.f`, etc.).

4. The three contributions are added, yielding (C.1).

As mentioned above, the invariants $\alpha_l$ are computed during the computation of the symmetrised tensors. Hence in Table C.1 we show an overview which indicates at which step in the computation of the symmetrised tensors each invariant is computed.

*Method 1.x*

The implementation of Methods 1.0, 1.1 and 1.2 is very similar to the one described above. The subroutines `EVAL_RHS`, `COLGRADUVW` (computes the velocity gradient at four collocated locations when using Method 1.x), `MODEL` are replaced by the ones located in `evalrhs_method1.f`, `gradtensor_method1.f` and `modeltensor_method1x.f` respectively.

## C.2 Particle tracking

For the study of the temporal evolution of certain geometrical shapes (e.g. a plane or a line) we consider a method for tracking particles (a list of positions). Hence together with the (M)NSE we solve the additional equations given by

$$\frac{d\mathbf{x}^{(q)}(t)}{dt} = \mathbf{u}^h(\mathbf{x}^{(q)}(t), t), \;\; \mathbf{x}^{(q)}(0) = \mathbf{x}_0^{(q)},$$

for $q = 1, \ldots, N_q$. Where $N_q$ is the number of particles which are to be tracked. By $\mathbf{u}^h(\mathbf{x}^{(q)}(t), t)$ we denote the interpolation (where the order of accuracy is equal to that of the spatial discretisation) of the velocity approximation $\mathbf{u}^h$ at the location $\mathbf{x}^{(q)}(t)$.

Let's consider this in more detail for $d = 2$. Suppose that particle $q$ is located inside the following shifted control volumes

$$\mathbf{x}^{(q)}(t) \in \Omega_{i_x+\frac{1}{2},j_x} \cap \Omega_{i_y,j_y+\frac{1}{2}},$$

for some $i_x, j_x, i_y, j_y$. Then bilinear interpolation using

$$u^h_{i_y-1,j_y}, u^h_{i_y,j_y}, u^h_{i_y-1,j_y+1}, u^h_{i_y,j_y+1}$$

yields a second-order accurate approximation to $u(\mathbf{x}^{(q)}(t), t)$. Similarly, bilinear interpolation using

$$v^h_{i_x,j_x-1}, v^h_{i_x+1,j_x-1}, v^h_{i_x,j_x}, v^h_{i_x+1,j_x}$$

yields an $\mathcal{O}(h^2)$ accurate approximation to $v(\mathbf{x}^{(q)}(t), t)$.

Applying the same bilinear interpolation to the three times larger shifted control volumes yields $\mathcal{O}((3h)^2)$ accurate approximations. Extrapolation then gives a fourth-order approximation to $\mathbf{u}(\mathbf{x}^{(q)}(t), t)$. Given such an approximation, we can apply the parameter dependent one-leg method to compute an approximation to $\mathbf{x}^{(q)}(t)$.

This is implemented in `ptracking.f`.

## C.3 Energy spectrum

### C.3.1 Computation of the one-dimensional energy spectrum

Here we describe how we compute the one-dimensional energy spectrum function $E(k, t)$ (defined in 2.2.2) inside `FORTRAN`. We start off by assuming that we already have the Fourier components of some velocity field $\mathbf{u}$ (in Section C.3.2 we describe how the Fourier components are computed).

We denote by $\hat{\mathbf{u}}_\mathbf{k}$ the Fourier component corresponding to the wave vector $\mathbf{k}$. Recall the definition of $E(k, t)$

$$E(k, t) = \pi k^2 \phi(k, t),$$

where $\phi(k,t)$ is the average energy corresponding to wave vectors of magnitude $|\mathbf{k}| = k$. One way of approximating $E(k_i,t)$ is then given by

$$E(k_i,t) = \sum_{\mathbf{k}\in S(k)} \|\hat{\mathbf{u}}_\mathbf{k}\|^2,$$

where $S(k)$ is the set of wave vectors which have a *rounded* magnitude of $k$, that is

$$S(k) = \{\mathbf{k}\,;\ \lfloor\|\mathbf{k}\|\rceil = k\}\,.$$

The problem with this approximation is that

$$|S(k)| - 4\pi k^2$$

is relatively large for small values of $k$ Hence the error made in approximating $4\pi k^2$ by $|S(k)|$ results in a "bumpy" energy spectrum. This can be remedied by considering instead

$$E(k_i,t) = \sum_{\mathbf{k}\in S(k_i)} \frac{k^2}{|S(k_i)|}\|\hat{\mathbf{u}}_\mathbf{k}\|^2,$$

however this approach has the disadvantage that the sum over all wavenumbers no longer equals the total kinetic energy

$$\sum_{i=1}^{i_{\max}} E(k_i,t) \neq E(t).$$

Instead we opt for a "smoothing" strategy which is achieved by redefining $S(k)$. We consider

$$S^r(k) := \{\mathbf{k}\,;\ \lfloor\|\mathbf{k}+\mathbf{d}\|\rceil = k, \mathbf{d}\in D^r\}\,,$$

where the set of wave vector shifts $D^r$ is given by

$$D^r := \left\{\mathbf{d} = (d_1,d_2,d_3)\,;\ d_m = -\frac{1}{2} + \frac{i-\frac{1}{2}}{r}, \quad m = 1,2,3, \quad i = 1,\ldots,r\right\}.$$

Note that $r = 1$ yields $S^1(k) = S(k)$. The parameter $r$ can be interpreted as a resolution. The resulting energy spectrum is then approximated by

$$E^r(k_i,t) = \sum_{\mathbf{k}\in S^r(k_i)} \frac{\|\hat{\mathbf{u}}_\mathbf{k}\|^2}{r^3}.$$

This preserves the total kinetic energy, that is, summation over $E^r(k_i,t)$ still equals $E(t)$. In Figure C.1 we show the resulting energy spectrum functions for several values of $r$.

### C.3.2 Fast Fourier transform

Here we describe how the three dimensional Fourier transform was constructed from the three consecutive one-dimensional Fast Fourier Transforms. The built-in FFT routines `FFTX`, `FFTY` and `FFTZ` can be used to compute the 3D FFT. However, each of the routines assumes the input array $\mathbf{u}$ is real valued. This makes sense since the velocity field indeed satisfies this property.

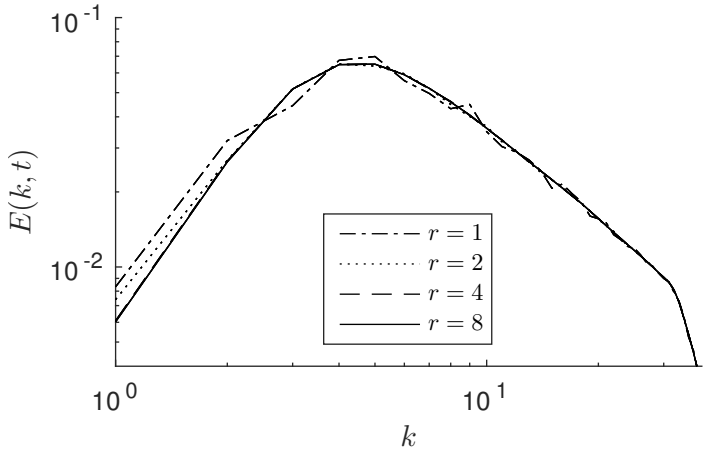


Figure C.1: Comparison between different resolution values $r$.

Consider for the moment the one-dimensional case, $u_i$ is now one-dimensional and real valued, for $i = 1, \ldots, N$. The output of, for example, `FFTX` is not given by the complex valued $N \times 1$ array $\hat{\mathbf{u}}$ containing the Fourier coefficients of $\mathbf{u}$. Instead the following array is given as output

$$\begin{aligned} \tilde{u}_k &= \Re(\hat{u}_k), \quad k = 1, \ldots, N/2+1, \\ \tilde{u}_{N/2+k} &= \Im(\hat{u}_k), \quad k = 2, \ldots, N/2. \end{aligned}$$

Together with the conjugate symmetry property

$$\hat{u}_{N/2+k} = \overline{\hat{u}_{N/2-k+2}}, \quad k = 2, \ldots, N/2,$$

and the fact that $\hat{u}_k \in \mathbb{R}$ for $k = 1$ and $k = N/2+1$, this array also completely describes the discrete Fourier transform of $\mathbf{u}$ in the sense that one can reconstruct $\hat{\mathbf{u}}$ from $\tilde{\mathbf{u}}$. Since the (discrete) Fourier transform is a linear operation, this conjugate symmetry property can be extended to $d$ dimensional FFT's as well.

Consider now the three dimensional case, where $\mathbf{u}$ is an array (or variable) of three indices, each running from 1 to $N$. We define the following arrays, derived from $\mathbf{u}$

$$\mathbf{u}^{(1)} = \Re(\mathcal{F}_x\{\mathbf{u}\}), \mathbf{u}^{(2)} = \Im(\mathcal{F}_x\{\mathbf{u}\}), \mathbf{u}^{(11)} = \Re(\mathcal{F}_y\{\mathbf{u}^{(1)}\}), \ldots, \mathbf{u}^{(222)} = \Im(\mathcal{F}_z\{\mathbf{u}^{(22)}\}), \tag{C.2}$$

hence yielding 8 arrays, denoted by $\mathbf{u}^{(pqr)}$. Here $\mathcal{F}_{x_i}$ denotes applying the FFT in the $i$-th direction. It immediately follows that

$$\hat{\mathbf{u}} = \mathcal{F}_z\{\mathcal{F}_y\{\mathcal{F}_x\{\mathbf{u}\}\}\} = \mathbf{u}^{(111)} - \mathbf{u}^{(122)} - \mathbf{u}^{(212)} - \mathbf{u}^{(221)} + i(-\mathbf{u}^{(222)} + \mathbf{u}^{(211)} + \mathbf{u}^{(121)} + \mathbf{u}^{(112)}).$$

Note that the 8 arrays given by (C.2) are explicitly given when using `FFTX`, `FFTY` and `FFTZ` on the array $\mathbf{u}$, but only for the wave vectors $\mathbf{k} = (k_1, k_2, k_3) \in \{0, \ldots, N/2\}^3 =: \mathbf{K}^{(111)}$. Hence we already have $\hat{\mathbf{u}}$ for $\mathbf{k} \in \mathbf{K}^{(111)}$. We define the following subsets of $\{-N/2+1, \ldots, N/2\}$

$$\mathbf{K}^{(1)} = \{0, \ldots, N/2\}, \mathbf{K}^{(2)} = \{-N/2+1, \ldots, -1\}.$$

These sets induce the following Cartesian products

$$\mathbf{K}^{(lmn)} := \mathbf{K}^{(l)} \times \mathbf{K}^{(m)} \times \mathbf{K}^{(n)}, \quad \text{for } l, m, n = 1, 2.$$

Let $\mathbf{k}^{(lmn)}$ denote the restriction of $\mathbf{k}$ to $\mathbf{K}^{(lmn)}$. The goal is now to express $\mathbf{u}(\mathbf{k}^{(lmn)})$ in terms of $\mathbf{u}(\mathbf{k}^{(111)})$. From repeatedly using the conjugate symmetry property it follows that

$$\mathbf{u}^{(pqr)}(\mathbf{k}^{(lmn)}) = (-1)^{\delta_{p2}\delta_{l2}+\delta_{q2}\delta_{m2}+\delta_{r2}\delta_{n2}}\mathbf{u}^{(pqr)}(\mathbf{k}^{(111)}).$$

Using this identity then completely describes how to recover $\hat{\mathbf{u}}$ from $\mathbf{u}^{(pqr)}(\mathbf{k}^{(111)})$, this is implemented in the subroutine `RECONSTRUCT` which is called inside `ENERGYSPECTRUM`, both subroutines are contained in `energyspectrum.f`.

# Appendix D

# Additional figures

## D.1 Numerical validation: accuracy, second-order results

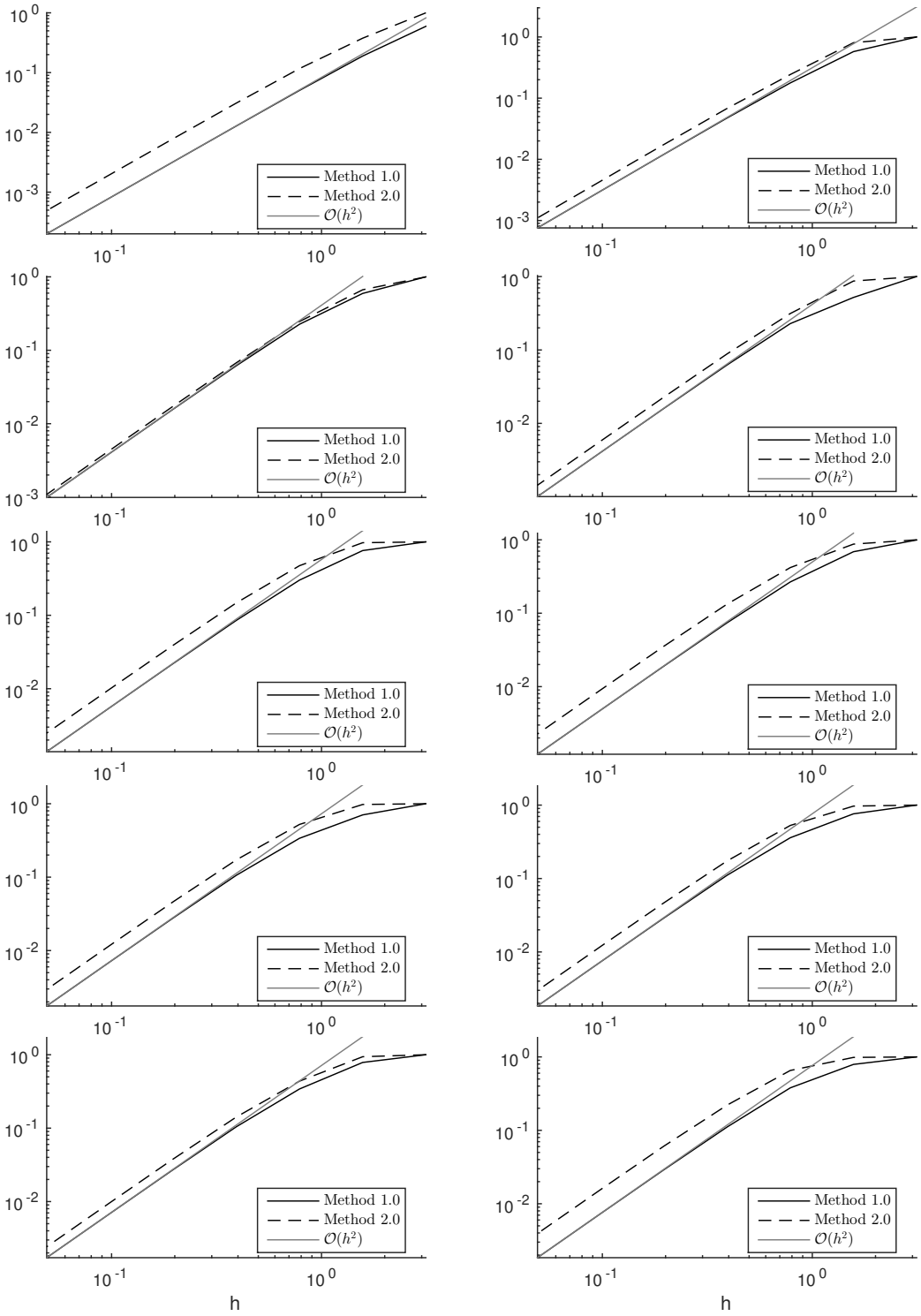


Figure D.1: Relative $L^2$-error as given by (4.11) using second-order accurate approximation. From left to right, top to bottom: $\boldsymbol{\tau}_l$, for $l = 1, \ldots, 10$.

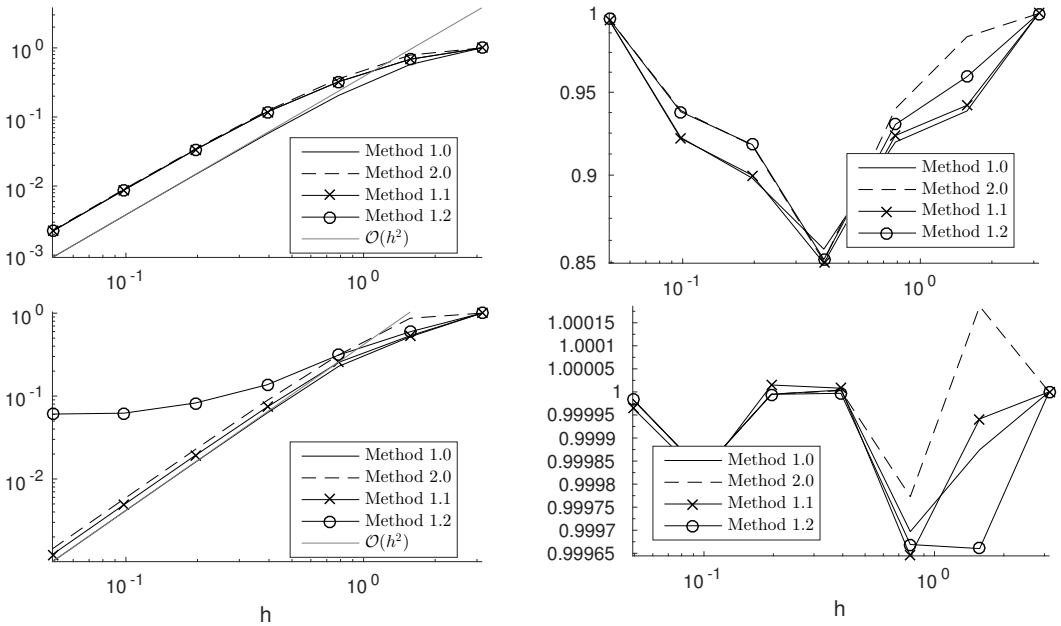


Figure D.2: From left to right, top to bottom: $\tilde{\boldsymbol{\tau}}_l$, for $l = 2, \ldots, 5$.

# Bibliography


Berselli, L. C., Iliescu, T., and Layton, W. J. (2005). *Mathematics of large eddy simulation of turbulent flows*. Springer.

Cerutti, S. and Meneveau, C. (2000). Statistics of filtered velocity in grid and wake turbulence. *Physics of Fluids (1994-present)*, 12(5):1143–1165.

Cerutti, S., Meneveau, C., and Knio, O. M. (2000). Spectral and hyper eddy viscosity in high-Reynolds-number turbulence. *Journal of Fluid Mechanics*, 421:307–338.

Comte-Bellot, G. and Corrsin, S. (1971). Simple Eulerian time correlation of full-and narrow-band velocity signals in grid-generated,'isotropic' turbulence. *Journal of Fluid Mechanics*, 48(02):273–337.

Frisch, U. (1995). *Turbulence: the legacy of AN Kolmogorov*. Cambridge University Press.

Kang, H. S., Chester, S., and Meneveau, C. (2003). Decaying turbulence in an active-grid-generated flow and comparisons with large-eddy simulation. *Journal of Fluid Mechanics*, 480:129–160.

Kolmogorov, A. N. (1941). The local structure of turbulence in incompressible viscous fluid for very large Reynolds numbers. In *Dokl. Akad. Nauk SSSR*, volume 30, pages 301–305. JSTOR.

Kosovic, B. (1997). Subgrid-scale modelling for the large-eddy simulation of high-Reynolds-number boundary layers. *Journal of Fluid Mechanics*, 336:151–182.

Lund, T. S. and Novikov, E. (1993). Parameterization of subgrid-scale stress by the velocity gradient tensor.

Manteuffel, T. A. and White, A. B. (1986). The numerical solution of second-order boundary value problems on nonuniform meshes. *Mathematics of Computation*, 47(176):511–535.

McDonough, J. (2004). Introductory lectures on turbulence Physics, Mathematics and Modeling.

Pope, S. B. (2001). *Turbulent flows*. Cambridge Univ Press.

Rozema, W. and Bae, H. J. (2016). Initial conditions for large-eddy simulation of decaying homogeneous isotropic turbulence. `http://web.stanford.edu/~hjbae/CBC`. Accessed: 2016-03-13.

Sagaut, P. (2002). *Large eddy simulation for incompressible flows*. Springer.

Serrin, J. (1963). The initial value problem for the Navier-Stokes equations. *Nonlinear problems*, 9:69ff.

Silvis, M. H. and Verstappen, R. (2015). Physically-consistent subgrid-scale models for large-eddy simulation of incompressible turbulent flows. *arXiv preprint arXiv:1510.07881*.

Speziale, C. G. (1991). Analytical Methods for the Development of Reynolds-Stress Closures in Turbulence. *Annual Review of Fluid Mechanics*, 23(1):107–157.

Taylor, G. I. (1935). Statistical theory of turbulence. In *Proceedings of the Royal Society of London A: Mathematical, Physical and Engineering Sciences*, volume 151, pages 421–444. The Royal Society.

Verstappen, R. (2011). When does eddy viscosity damp subfilter scales sufficiently? *Journal of Scientific Computing*, 49(1):94–110.

Verstappen, R. and Veldman, A. (2003). Symmetry-preserving discretization of turbulent flow. *Journal of Computational Physics*, 187(1):343–368.

Vreman, A. (2004). An eddy-viscosity subgrid-scale model for turbulent shear flow: Algebraic theory and applications. *Physics of Fluids (1994-present)*, 16(10):3670–3681.

Vreman, B., Geurts, B., and Kuerten, H. (1996). Large-eddy simulation of the temporal mixing layer using the Clark model. *Theoretical and computational fluid dynamics*, 8(4):309–324.